

Final report dated 14.07.2023

PSIGE

Passive Seismic Imaging for GEothermal

Source: flickr/ Falk Lademann, creative commons



UNIVERSITÉ
DE GENÈVE

Date: 14.07.2023

Location: Bern

Publisher:
Swiss Federal Office of Energy SFOE
Energy Research and Cleantech
CH-3003 Bern
www.bfe.admin.ch

Subsidy recipients:
Department of Earth Sciences, University of Geneva
Rue des Maraichers 13, CH-1205 Geneva
https://www.unige.ch/sciences/terre/en/earth-sciences-department/

Authors:
Genevieve Savard, University of Geneva, genevieve.savard@unige.ch
Matteo Lupi, University of Geneva, matteo.lupi@unige.ch

SFOE project coordinator:
Valentin Gischig, valentin.gischig@bfe.admin.ch
Stefano Benato, stefano.benato@bfe.admin.ch

SFOE contract number: SI/501911-01

The authors bear the entire responsibility for the content of this report and for the conclusions drawn therefrom.

Résumé

Ce projet a pour objectif de tester la méthode de tomographie de bruit ambiant avec réseaux denses de capteurs (NANT) en tant que méthode économique et fiable pour l'exploration de ressources géothermiques. Cette méthode a démontré avec succès qu'il est possible d'imager la structure du sous-sol (plus particulièrement une propriété géophysique appelée la vitesse des ondes S) sur une grande superficie et à une profondeur qui pénètre le socle crystallin. La méthode NANT a été testée dans deux régions de la Suisse à haut potentiel géothermique: le canton de Argovie et la région multinationale qui entoure Riehen, à Bâle-Ville. Les campagnes de mesure sur le terrain se sont déroulées sans aucune incidence pour les populations locales, même dans la zone urbaine de Bâle. Cela souligne que cette méthode est non-invasive et logistiquement simple à planifier en comparaison avec les méthodes d'exploration conventionelles, telle la sismique réflexion, qui requiert des camions vibrateurs. Les données de bruit sismique ambiant que nous avons recueillies avec nos capteurs nous ont permis de faire des observations d'ondes de surface aux fréquences requises pour imager le sous-sol jusqu'à 5 kilomètres de profondeur. Les modèles du sous-sol que nous avons obtenus à partir de ces données se comparent favorablement aux données géologiques et géophysiques connues à ces deux localités, y compris des contrastes majeures entre unités géologiques (fossé rhénan) et des contrastes plus subtiles qui peuvent être associés à des failles connues et des anomalies causées par la présence de fluides en profondeur. La méthode NANT se révèle prometteuse pour l'exploration des ressources géothermiques en Suisse.

Summary

This project aimed to test ambient noise tomography (ANT) with dense nodal networks as an economically and scientifically valuable geothermal exploration tool. The method succeeds at imaging the shear wave velocity structure of the subsurface, over a large area and can image the crystalline basement structure. Nodal ANT was successfully tested in two areas of high geothermal potential in Switzerland: the canton of Aargau and the area surrounding Riehen, Basel-Stadt. The field campaigns and the deployments went almost unnoticed by the local communities even in densely urbanized areas, highlighting how non-invasive and logistically simple this method is. The data retrieved from the temporary sensor deployments recorded ambient noise characteristics that allowed confident observations of surface wave characteristics at the low frequencies required for deep imaging, despite the very varied site conditions and shallow depth of burial. The subsurface models developed from these data reach a depth of 5 km and compare favourably with the known geology in these two areas, including the expected large-scale tectonic unit contrasts caused by major graben structures but also finer scale velocity contrasts suggesting the presence of several faults and fluid anomalies. From our models, we have also developed interpretations to explain the geometry of measured heat flux anomalies and low shear wave velocities in terms of fluid flow. The NANT method is found to be promising for geothermal exploration in Switzerland.

Main findings

Ambient noise tomography applied to dense temporary nodal arrays of geophones is an effective, low-cost method to acquire a model of the subsurface for a large area and down to arbitrary depths. It has several unique advantages compared to traditional exploration methods:

- The method can image the subsurface at the depths relevant to geothermal exploration including the crystalline basement;
- Low shear-wave velocity anomalies may be linked to the presence of underground fluids, which are the target for geothermal exploration;
- The required fieldwork campaigns cause little to no disturbance for local communities as they do not require artificial seismic sources. This facilitates public acceptance of exploration campaigns and facilitates greatly campaign planning and logistics.

This method can help pinpoint promising sites for drilling and more importantly, provide information at depths where the potential for geothermal electricity generation is high but where other geophysical imaging methods have little to no resolution.

Contents

1 Introduction **6**
- 1.1 Background information and current situation . . . 6
- 1.2 Purpose of the project . . . 6
- 1.3 Objectives . . . 7

2 Procedures and data acquisition **8**
- 2.1 Equipment acquisition . . . 8
- 2.2 Site selection and geological context . . . 8
  - 2.2.1 Aargau . . . 8
  - 2.2.2 Riehen . . . 12
- 2.3 NANT deployment in Aargau . . . 12
- 2.4 NANT deployment in Riehen . . . 15
- 2.5 Quality control and data preparation . . . 17

3 Methodologies **20**
- 3.1 Seismic ambient noise conditions . . . 20
- 3.2 Wavefields retrieved from ambient noise and directivity analysis . . . 22
  - 3.2.1 Cross-correlation and stacking methods . . . 22
  - 3.2.2 Surface wave observations . . . 25
- 3.3 Noise directivity analysis . . . 25
- 3.4 Local seismicity during the deployments . . . 26
- 3.5 Frequency-Time ANalysis (FTAN) and group dispersion picking . . . 27
  - 3.5.1 Picking approaches . . . 28
  - 3.5.2 Bi-modal distribution of group velocities . . . 28
  - 3.5.3 Outlier rejection . . . 34
- 3.6 Group velocity maps . . . 34
- 3.7 Depth inversion . . . 35
- 3.8 Rayleigh wave ellipticity (H/V ratio) . . . 35

4 Results: Aargau subsurface model **38**
- 4.1 Group velocity maps . . . 38
  - 4.1.1 Rayleigh waves . . . 38
  - 4.1.2 Love waves . . . 38
- 4.2 3D shear wave velocity model . . . 40
- 4.3 Comparison to seismic reflection . . . 44
- 4.4 H/V ratios . . . 44

5 Results: Riehen area subsurface model **49**
- 5.1 Group velocity maps . . . 49
  - 5.1.1 Rayleigh waves . . . 49
  - 5.1.2 Love waves . . . 49
- 5.2 3D shear wave velocity model . . . 51
- 5.3 Comparison to seismic reflection . . . 55
- 5.4 H/V ratios . . . 55

6 Discussion of results **58**
- 6.1 Comparison to other methods . . . 58
- 6.2 NANT as a geothermal exploration tool: finding a drilling target . . . 59

7 Conclusions and outlook **60**

8 Publications **61**

A Data quality control **66**
A.1 Node metadata . . . 66
A.2 Comparison to broadband seismometer . . . 66

B FK decomposition of the recovered wavefield **68**

C Predicted dispersion and sensitivity kernels **70**
C.1 Riehen . . . 70
C.2 Aargau . . . 70

D Uncertainty and resolution estimation **74**
D.1 Checkerboard tests . . . 74
D.2 Bootstrap resampling . . . 74
D.3 Comparison of different picking datasets . . . 74

E Polarization analysis to enhance body wave energy **79**

F Local seismicity recorded by the Riehen nodal network **81**

G Comparison to regional earthquake tomography **83**

H Possible methodological improvements **86**

1. Introduction

1.1 Background information and current situation

The success of geothermal resource exploitation largely relies on the prior knowledge of the subsurface. Indeed, one of the key challenges for the industry is the high-risk cost of drilling to confirm the existence of a viable geothermal resource [Harvey et al., 2014]. Methods from different disciplines such as geology, geochemistry, and geophysics are commonly employed during the exploration phase to reduce the subsurface uncertainty and better characterize the geothermal resource. The use of such techniques is key to lowering subsurface uncertainty and de-risk the drilling phase, i.e., to increase the probability of success of a project and maximize its estimated monetary value.

The main geophysical methods used for geothermal exploration can be divided into three categories: gravimetric, electromagnetic, and seismic. Gravity surveys can provide information about density anomalies related to lateral variations in lithologies. Electromagnetics methods such as magnetotellurics or controlled source electromagnetic (CSEM) can map the electrical resistivity of the subsurface, helping to constrain the depth of certain types of reservoirs. Gravity and electromagnetics methods are affordable potential methods, but they provide limited information about the subsurface structures, and they can be affected by anthropogenic noise typical of urban environments.

To obtain a clear and detailed image of the subsurface, including faults and geometry of the stratigraphic layers, active seismic reflection is to date the only tool available. Unfortunately, seismic reflection is also the costliest method, at around 18'000 CHF per km^2 [Jenne et al., 2013], and sometimes much more. For instance, the 3D seismic reflection campaign of St Gallen covered an area of 270 km2 and led to a net cost of about 10 million CHF [Huwiler, 2012]. The development of geothermal energy is still hindered by a lack of cost-effective exploration methods.

Recently, noise-based passive seismic methods started to be applied to geothermal reservoir imaging and monitoring. Obermann et al. [2015] monitored the geothermal site of St. Gallen, revealing an aseismic perturbation likely related to gas infiltration into the well after fluid injection. With a similar study, Hillers et al. [2015] detected and located an aseismic transient deformation in response to the 2006 Basel reservoir stimulation experiment. Taira et al. [2018] characterized reservoir responses to earthquakes and fluid extraction at the Salton Sea geothermal field, California. Sánchez-Pastor et al. [2019] monitored responses of a geothermal reservoir to production and stimulation operations in Reykjanes, Iceland. Around the geothermal sites of Soultz-sous-foret and Rittershoffen in France, noise-directivity analyses and Ambient-Noise Tomographies (ANTs) were carried out to retrieve shear-wave velocity models of the upper crust around the reservoirs [Lehujeur et al., 2015, 2017, 2018]. The authors identified seismic velocity anomalies that they attributed to hydrothermal fluid circulation at the base of the sedimentary cover. However, their project did not include a comparison of their results with a 3D active seismic model, an important step for the benchmarking of the method.

To date, ANTs are almost exclusively performed with surface waves. Surface waves are retrieved from ambient noise as they propagate coherently across large distances. Surface waves are mainly sensitive to the shear-wave velocity profile of the subsurface. They are thus an interesting proxy to detect fractured or fluid-filled lithostratigraphic units. Unfortunately, the large wavelengths of surface waves needed to probe deep structures imply a low resolution of the corresponding tomographic images. In contrast, the resolution of body-wave tomography is much higher, in particular with increasing depth. However, retrieving individual crustal body waves from ambient noise is challenging because their amplitude is much smaller than surface waves. Outside of a geothermal exploration context, a single case study demonstrated the possibility to extract individual P-waves from ambient noise. This study from Nakata et al. [2015] took place in Long Beach, California, and delivered a high-resolution 3D P-wave velocity model of the first 1000 m of the subsurface.

1.2 Purpose of the project

ANT has gained interest in the last few years due to the development of affordable, portable, and wireless seismic sensors [Hand, 2014]. The ANT method consists in constructing a 3D seismic-velocity model of the

subsurface based on the travel-times of individual waveforms extracted from the ambient-noise wavefield. The ANT technique does not rely on the manipulation of expensive active sources (e.g., vibroseis trucks), and does not rely on the occurrence of natural seismicity either. The data acquisition is purely passive and non-invasive, consisting of independent (i.e. cableless) passive seismic sensors to be installed in the ground shallow subsurface for a period of about 1 month. We note that this type of data acquisition could greatly improve the public acceptance of subsurface exploration. The ANT technique applied to dense nodal arrays (NANT) could also significantly reduce the cost of geothermal exploration. However, ANT has been seldom applied to dense nodal arrays and there is a need for more studies demonstrating how the method, historically applied in regional to continental scale studies, performs at a local scale close to urban centres where geothermal energy is most needed.

The purpose of this project is to demonstrate the performance of ANT with temporary dense nodal arrays (NANT) in providing useful images of the subsurface for geothermal exploration. To achieve this goal, we apply this method in two areas of Switzerland where:

1. There is a known high heat flow anomaly that makes the area interesting for geothermal exploration.
2. There are multiple previous geological and geophysical investigations in the area that allow comparisons with the NANT models to assess geological consistency and reliability.

The two areas selected for this project are the canton of Aargau and the international area around Riehen, Basel-Stadt. More details are provided in section 2.2.

1.3 Objectives

The objective of PSIGE is to develop and characterize NANT as an affordable and logistically simple geothermal (and upper crust in general) exploration technique. We intend to quantify the extent to which NANT could complement active seismic reflection surveys, in a way to drastically reduce exploration-related costs. Note that our project is in line with the objectives of Task 1.1 (Work Package 1) of the Swiss Competence Center for Energy Research – Supply of Electricity.

To increase the technology readiness level (TRL) of the NANT method, there are several technical challenges that we address in this project:

1. Demonstrate that nodal geophone deployments on the scale of two hundred or more are logistically simple, efficient, and fast while causing minimal disruption for residents and communities.
2. Develop and adapt existing ambient noise processing methodology to the processing of thousands of station pairs.
3. Demonstrate that surface waves arrivals can reliably be retrieved from temporary geophone recordings of up to a month and perform surface-wave ANT to extract a subsurface shear-wave velocity model. Compare this model with existing geological and geophysical datasets to assess its credibility.
4. Attempt to retrieve body wave arrivals from ambient noise recordings and demonstrate the value of three-component data to achieve this objective.

2. Procedures and data acquisition

2.1 Equipment acquisition

The PSIGE project initially planned the acquisition of 500 3-component seismic nodes. Following the allocation of a dedicated budget of CHF 148k from the SFOE, as well as a budget of CHF 52k by the University of Geneva, a purchase order of CHF 200k was placed in May 2020 with the company DTCC-Smart Solo. This first purchase allowed us to acquire 210 3-component seismic nodes, as well as the peripherals required to operate them. These instruments were deployed for the first ANT experiment in Aargau, from December 2020 to January 2021.

The model of geophone purchased (IGU-16HR 3C[1]) has a battery autonomy of up to 30 days (in Cycle On GPS mode) and a natural frequency of 5 Hz. While the amplitude of the instrument response decreases below 5 Hz, the sensitivity is sufficient to detect the low frequencies required for ambient noise tomography on a local scale, i.e. frequencies down to about 0.2 Hz (see section 3.1), below which the self-noise level of the geophone is expected to start dominating the signal.

In 2021, the Swiss company Geo2x expressed their interest in participating to the funding for an additional number of sensors and help with the time-consuming logistics of field deployments. However, the expected counterpart (granting Geo2x access to the sensor pool for private projects) could not be considered due to the public nature of the initial funds.

In Table 2.1, some of the key configuration parameters used for the SmartSolo geophones for the two experiments are listed.

	Aargau	Riehen
Start date and time	2020/12/05 00:00:00	2022/09/03 00:00:00
Sampling rate	4 ms	4 ms
GPS mode	Cycle On (8 min)	Always On
Number of channels	3	3
Preamplifier gain	36 dB	36 dB
Anti-alias filter	Linear Phase	Linear Phase
Lowcut filter	Disabled	Disabled
Max number of days recorded	30	21

Table 2.1: Key configuration parameters applied to the SmartSolo IGU-16HR 3C nodes for the two deployments

2.2 Site selection and geological context

Regions in Switzerland with high heat flow anomalies have higher geothermal potential for electricity generation, as the required drilling depths are shallower. The two sites selected for our ANT campaigns both coincide with regions of high heat flow, as shown in Figure 2.1.

2.2.1 Aargau

The first site selected for the application of nodal ANT is the canton of Aargau. It was proposed after discussions with representatives from Swisstopo, Nagra and SFOE. The canton of Aargau benefits from the highest heat flow anomaly in the country ($> 140\,\mathrm{mW/m^2}$), which is suspected to be related to hydrothermal circulation along faults bounding the Permo-Carboniferous trough crossing the area. There is also a strong political will in this canton to take advantage of these favourable geothermal conditions, but it is recognized that the lack of subsurface information hinders the development of new geothermal projects there[2].

[1] https://smartsolo.com/cp-3.html

[2] https://www.thinkgeoenergy.com/calls-for-mapping-of-geothermal-potential-in-aargau-switzerland/

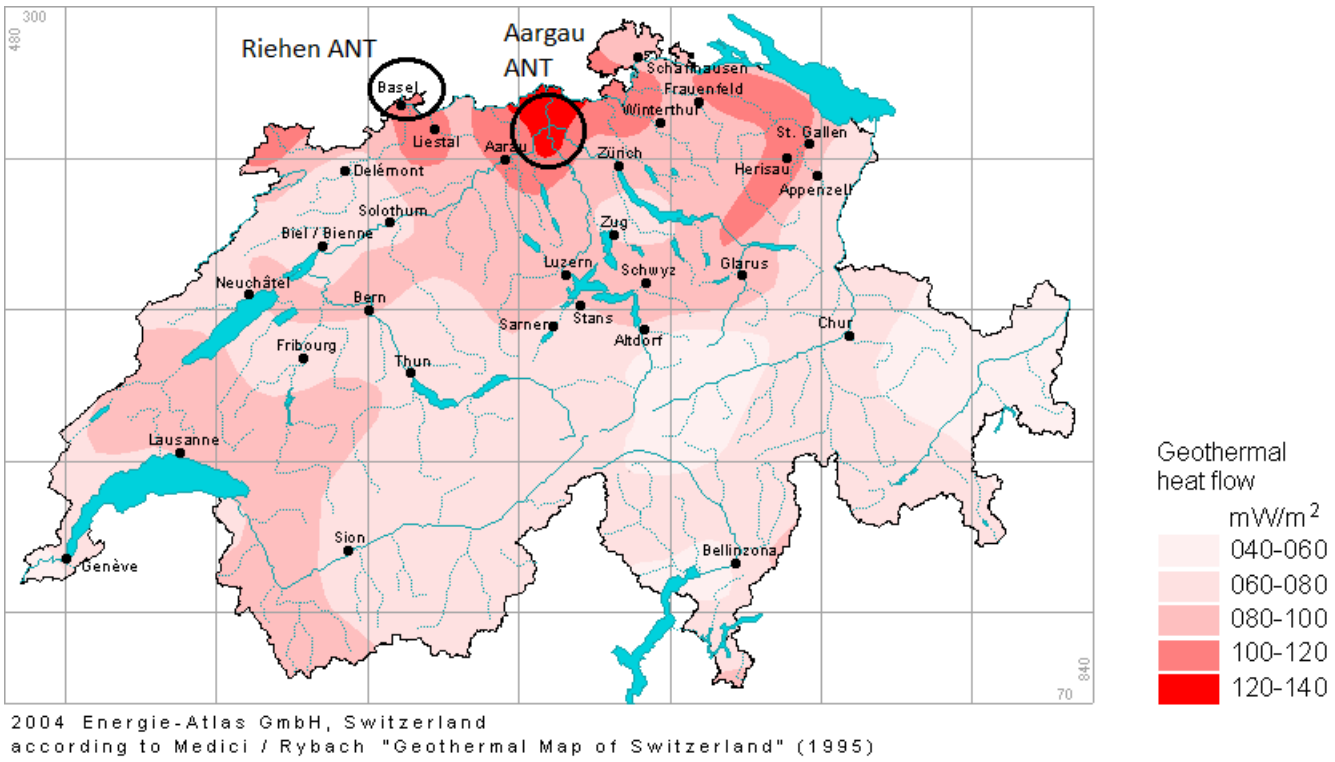


Figure 2.1: Map of geothermal heat flow in Switzerland. The two areas where we conducted ANT surveys are shown by black ellipses.

Figure 2.2 and 2.3 show the known geology in this area, according to the Swisstopo data repositories[3] and an interpreted depth cross-section by Eberhard [2016]. We note that this depth profile interpretation based on seismic reflection 2D lines has some small differences with a more recent study by Madritsch et al. [2018]. The study area is centred on the peak heat flux anomaly and is traversed by the north Permo-Carboniferous trough, which is a graben-like structure cutting through the crystalline basement which was filled with sedimentary rocks from the Permian and Carboniferous eras. The Permo-Carboniferous trough in northern Switzerland, also called the Constance-Frick trough, strikes in the east-west direction and is bounded by the Jura Main Thrust and the Mandach Thrust.

Existing subsurface information for this area includes several deep wells and an extensive database of 2-D seismic reflection profiles conducted by Nagra over the last 45 years with the aim of finding a suitable storage site for nuclear waste. Figure 2.4 shows an overview of existing datasets and major faults[4]. These existing datasets provide a good basis for observations to compare with our shear-wave velocity model. Nagra also conducted 3-D reflection seismic surveys between 2015 and 2017. The "Jura Ost" survey area overlaps with our study area. The depth-migrated model from these data is however not yet available to us for comparison [5]. There are also a few deep wells in the area by Nagra, most notably the deepest well, Riniken, located near the middle of our study area[6]. These well logs provide another useful data set for comparison to NANT.

The study of Madritsch et al. [2018] provides a great summary of the known geology in this area from the numerous Nagra reports over the last few decades along with a new interpretation of the many older and newer 2D seismic reflection profiles in this area. They suggest the Constance-Frick Trough is segmented in two at a location east of the Aare River that corresponds to the expected SE continuation of the Vorwald Fault, that acts as a transfer structure.

It is worth noting that the Constance-Frick trough is recognized as a structure that can provide a multitude of underground resources, as illustrated in Figure 2.5. In this context, the identification of fluid anomalies is key to harnessing the geothermal potential in this unique geological setting.

The field campaign in Aargau was conducted under the leadership of the previous PSIGE PI, Dr. Thomas Planès, from December 2020 to January 2021.

[3] https://www.swisstopo.admin.ch/en/maps-data-online/metadata-catalogue-geocat.html
[4] Nagra data made available on ArcGIS Online by Michael Ruff: https://arcg.is/1LiDX01
[5] According to Nagra report NAB 18-34 (2019) https://nagra.ch/en/downloads/arbeitsbericht-nab-18-34-2/
[6] Nagra report NTB-86: https://nagra.ch/en/downloads/technischer-bericht-ntb-86-02-2/

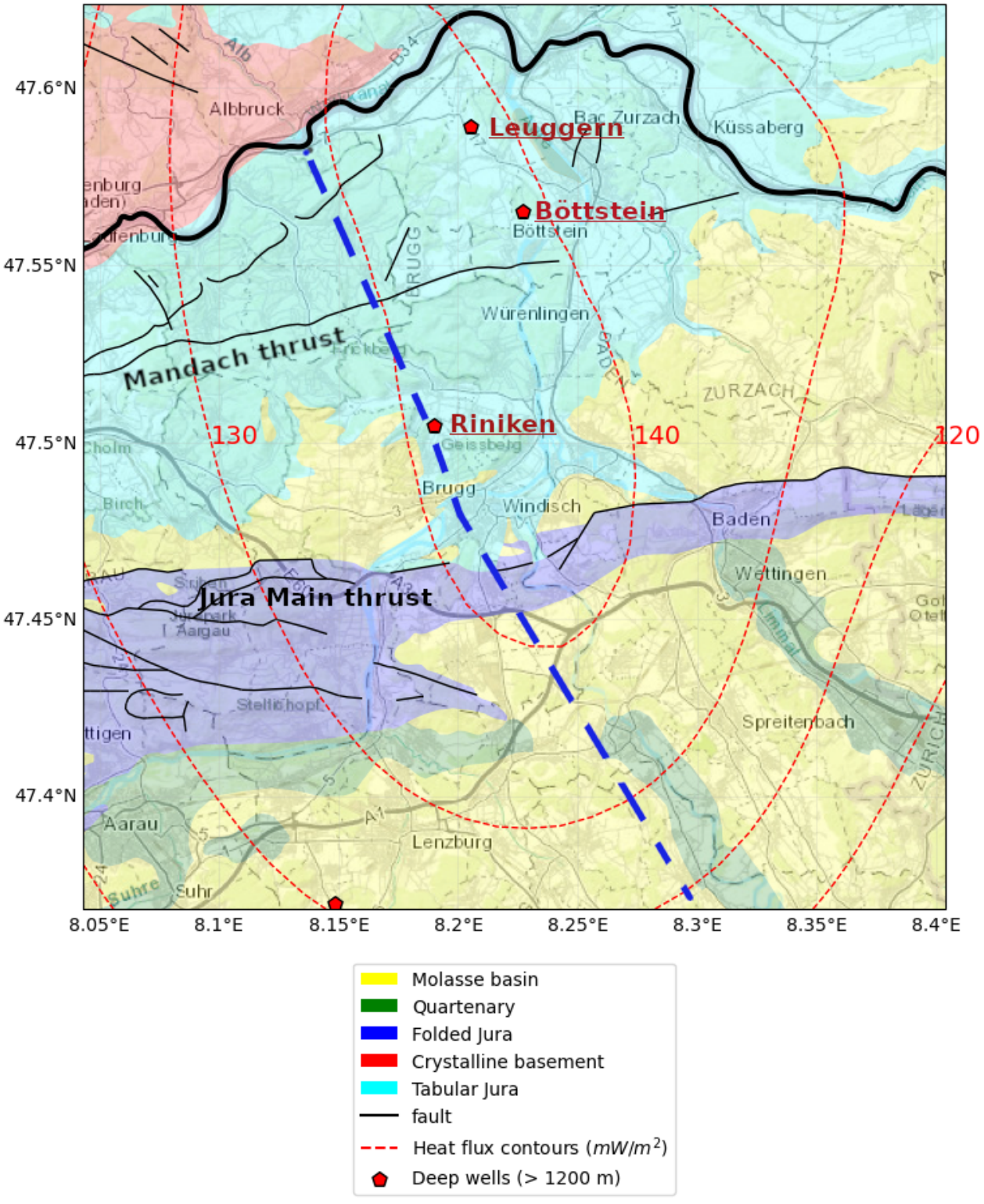


Figure 2.2: Surficial geology in the canton of Aargau, with data from Swisstopo. Colored polygons indicate different geological units, while thin black lines show the surface expression of several faults, with the Mandach thrust and the Jura Main thrust being two major fault zones. Red pentagons show the location of deep wells from nagra exceeding $1200\,\mathrm{m}$ in total depth. Dashed red lines show the isocontours of the heat flux, labelled in $\mathrm{mW/m^2}$. The blue dashed line indicates the trace of the depth cross-section in the following figures.

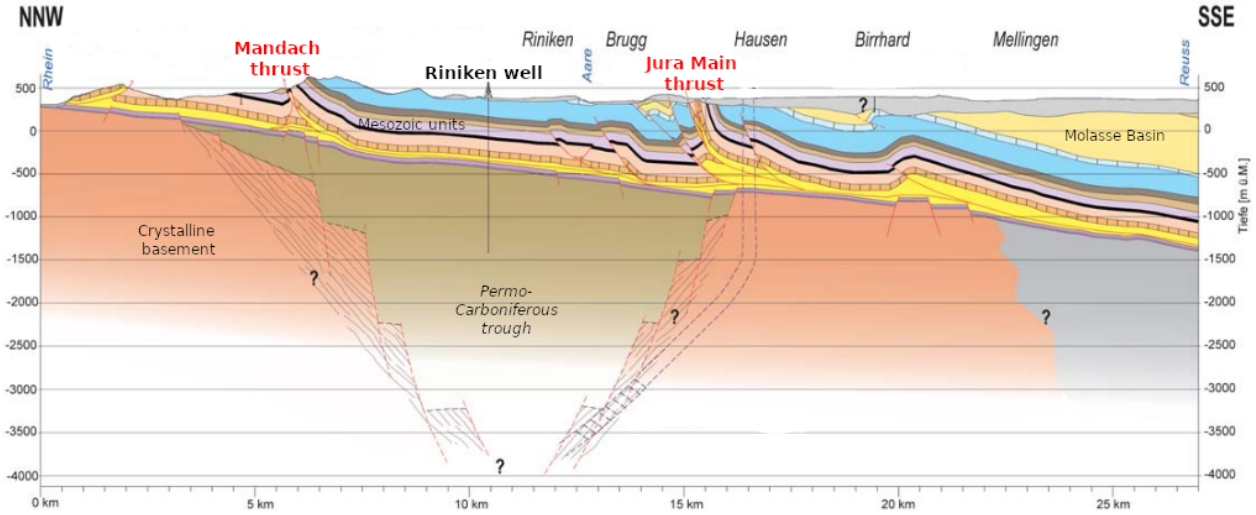


Figure 2.3: Interpreted depth cross-section along the blue trace in Figure 2.2 on the basis on 2D seismic reflection profiles and deep wells by Nagra. Modified from Eberhard [2016]

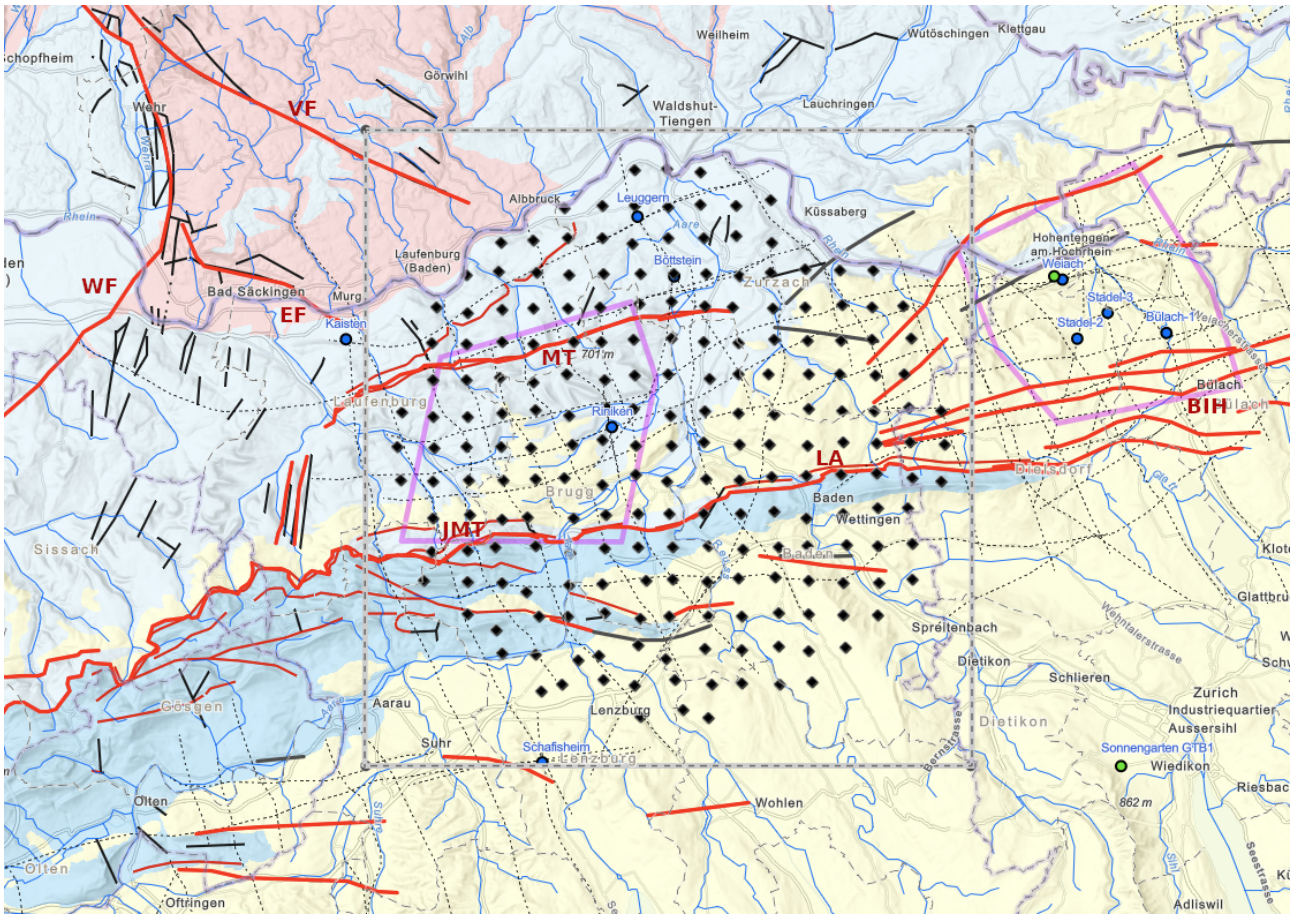


Figure 2.4: Regional overview of the Aargau study area (gray box outline) and NANT stations (black diamonds) along with existing 2D seismic reflection data (black dotted lines), 3D seismic reflection data (pink polygon show survey outline), deep boreholes (labelled blue circles) and major faults (thick red lines) from the Nagra database. Other faults from the Swisstopo database are shown as thinner solid red lines (thrust) and black lines (other faults). Major fault names: VF: Vorwald Fault, EF: Eggberg Fault, MT: Mandach Thrust, JMT: Jura Main Thrust, LA: Lägeren Anticline, BIH: Baden-Irchel-Herdern Fault zone, WF: Weiach Flexure

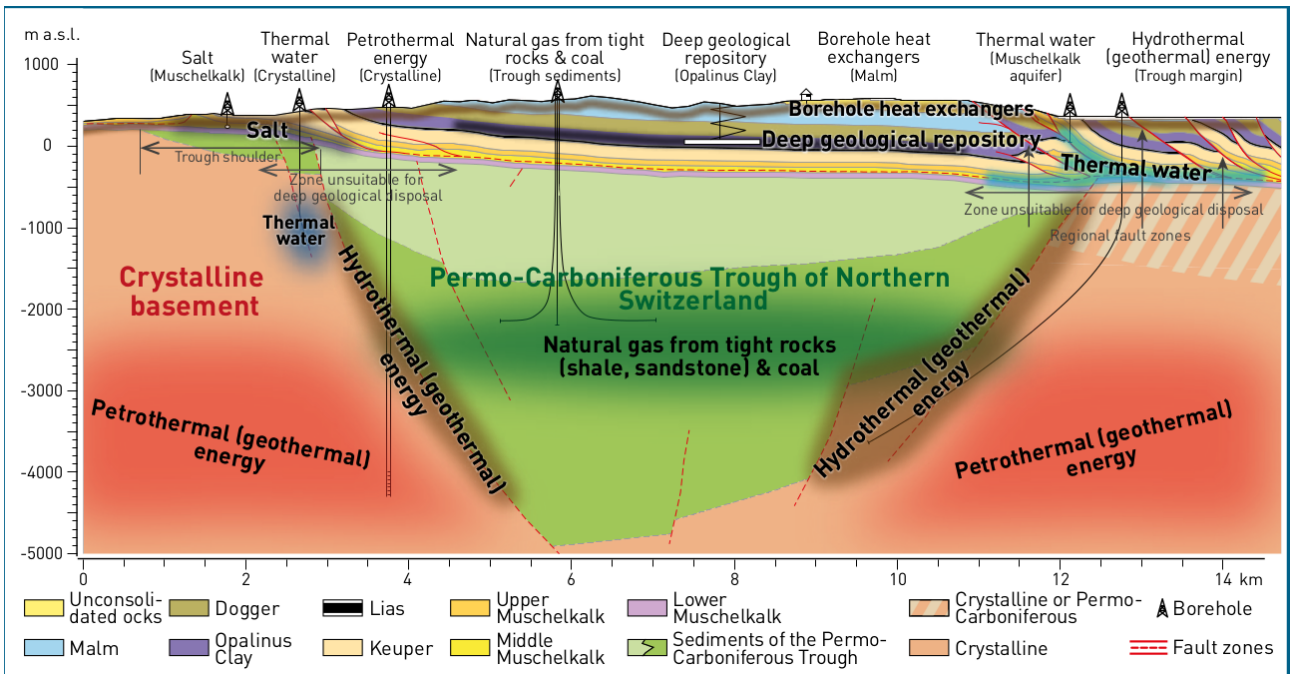


Figure 2.5: Potential underground resources in the canton of Aargau. This interpreted depth section follows the same cross-section as Figure 2.3. Figure taken from "Underground resources and deep geological repositories – a conflict?", by Nagra (`https://nagra.ch/en/downloads/resources-leaflet/`).

2.2.2 Riehen

In the context of the Geo2Riehen district heating project, Wärmeverbund Riehen AG showed interest in contributing CHF 68k in funding to study the subsurface to up to 2 km in depth using our NANT approach. In addition to the 3-D seismic reflection survey conducted by Wärmeverbund Riehen AG, there are multiple other geophysical observations in this area that may help benchmark the NANT method and/or interpret the velocity model. Indeed, Basel was infamously the site of the Deep Heat Mining Project, a ground-breaking hot dry rock EGS geothermal project from 2006 to 2009. Another reason why this area is particularly interesting for developing the NANT method is the denser urban environment that provides a potentially more challenging dataset for ambient noise processing. The high level of anthropogenic noise may also potentially help generate stronger body waves in the ambient noise waveforms, as in the Nakata et al. [2015] study.

The Riehen campaign was originally planned for 2020 but was postponed multiple times due to delays out of our control. In February 2022, the 3-D reflection seismic campaign was finally conducted in Riehen and neighbouring Basel-Stadt[7]. A contract was concluded with UniGe in May 2022 to allow us to conduct the NANT campaign. The deployment occurred in September 2022 and the data was collected in early October 2022.

Figure 2.6 below shows the geological context of the study area while Figure 2.7 shows an interpreted depth cross-section along the cyan dashed line, modified from Michel et al. [2017]. The area of Basel is one the most seismically active of Switzerland, due to the complex tectonic regime comprising the southern end of the extending Upper Rhine Graben and the northward propagation of the deformation front of the Jura fold and thrust belt to the south. The opening of the Rhine Graben occurred approximately 25 Ma ago and was progressively filled with thick marine and freshwater sediments. Different fault families of different orientations correspond to different phases of tectonic evolution: Hercynian NW-SE faults due to the Variscan-Hecynian orogen, Permo-Carboniferous E-W faults linked to the formation of the Permo-Carboniferous troughs and Rhenish NNE-SSW faults due to the opening of the Rhine Graben [Delacou et al., 2009]. Most notably, a major tectonic boundary in the study area is defined by the contact between the Rhine Graben to the west and the Mesozoic bedrock of the Tabular Jura to the east, which is named the Rhine Valley Flexure fault. This master fault splits the area of Riehen in two and is the target of the hydrothermal (geothermal) energy plant of the Geo2Riehen project.

2.3 NANT deployment in Aargau

The installation of the SmartSolo nodal geophones is straightforward, which allowed us to easily recruit field helpers for the deployment and retrieval of the stations. The deployment took place over 3.5 days from November, 30th 2020 to December 3rd 2020 and was performed by 7 independent teams of 2 to 3 persons. Each

[7] `https://www.erdwaermeriehen.ch/erdwaerme-riehen/geo2riehen.html`

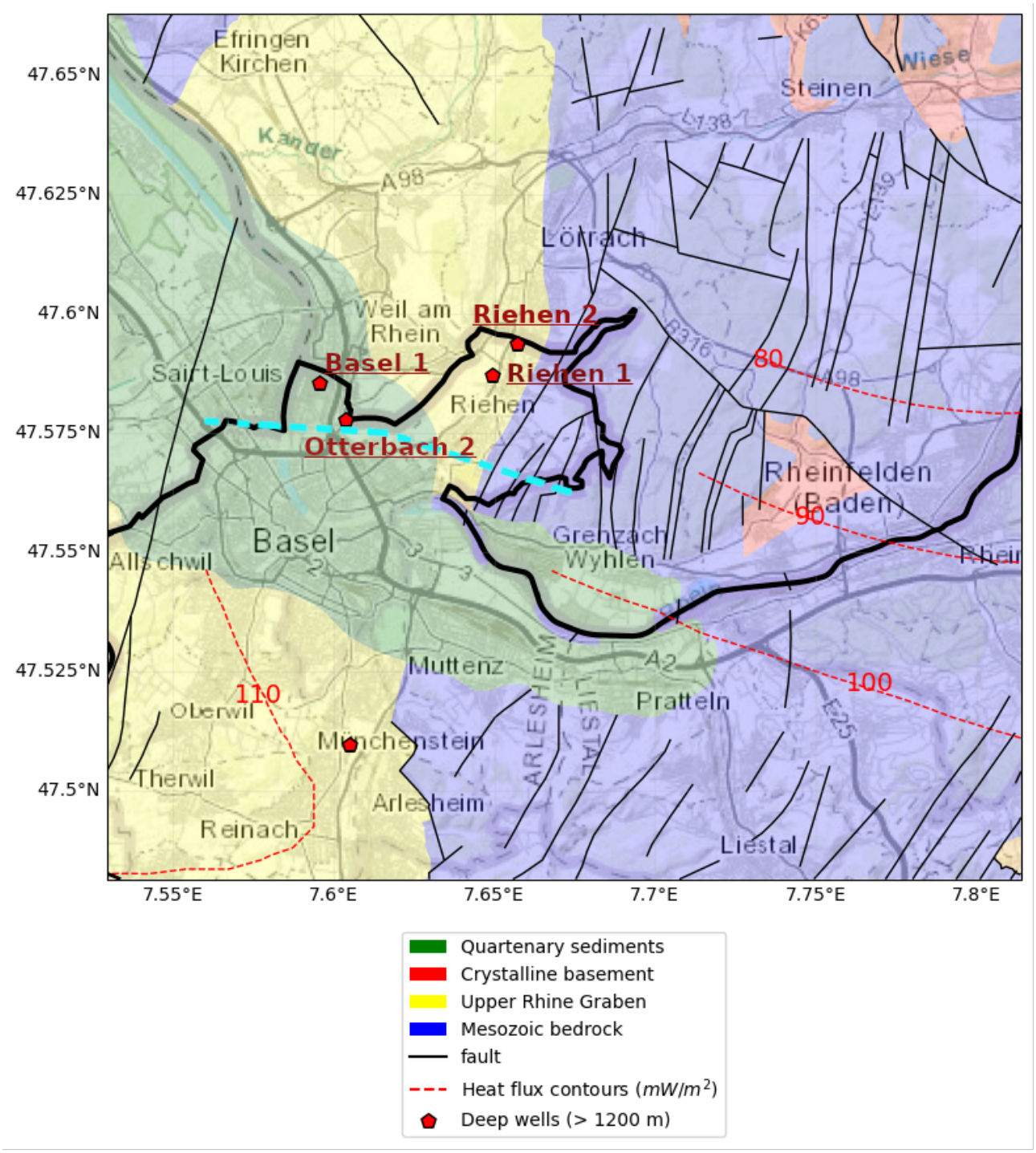


Figure 2.6: Surface geology of the study area according to the Swisstopo geological database. Heat flux contours are shown as red dashed lines and deep wells of more than $1200\,\mathrm{m}$ total depth as red pentagons.

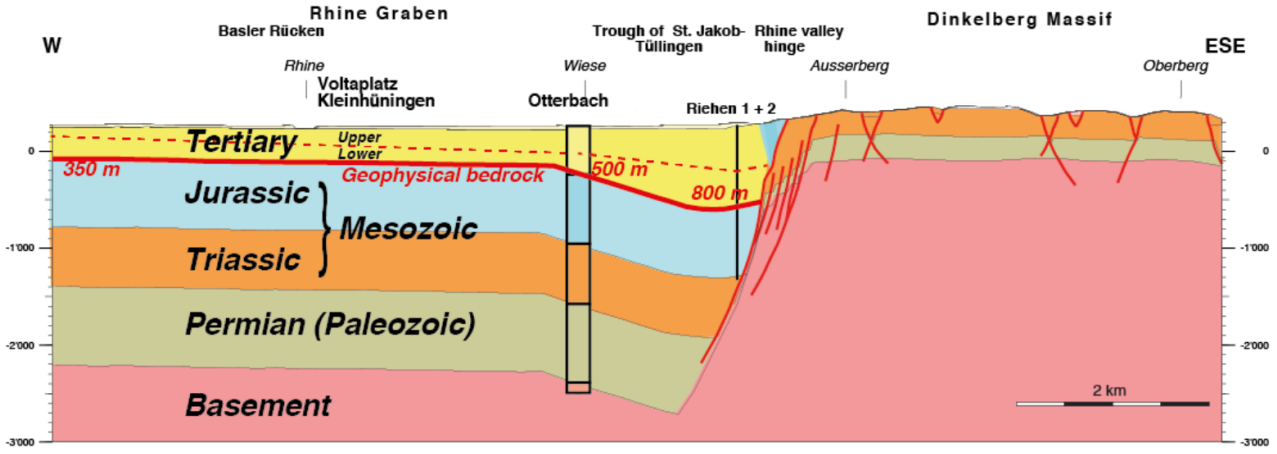
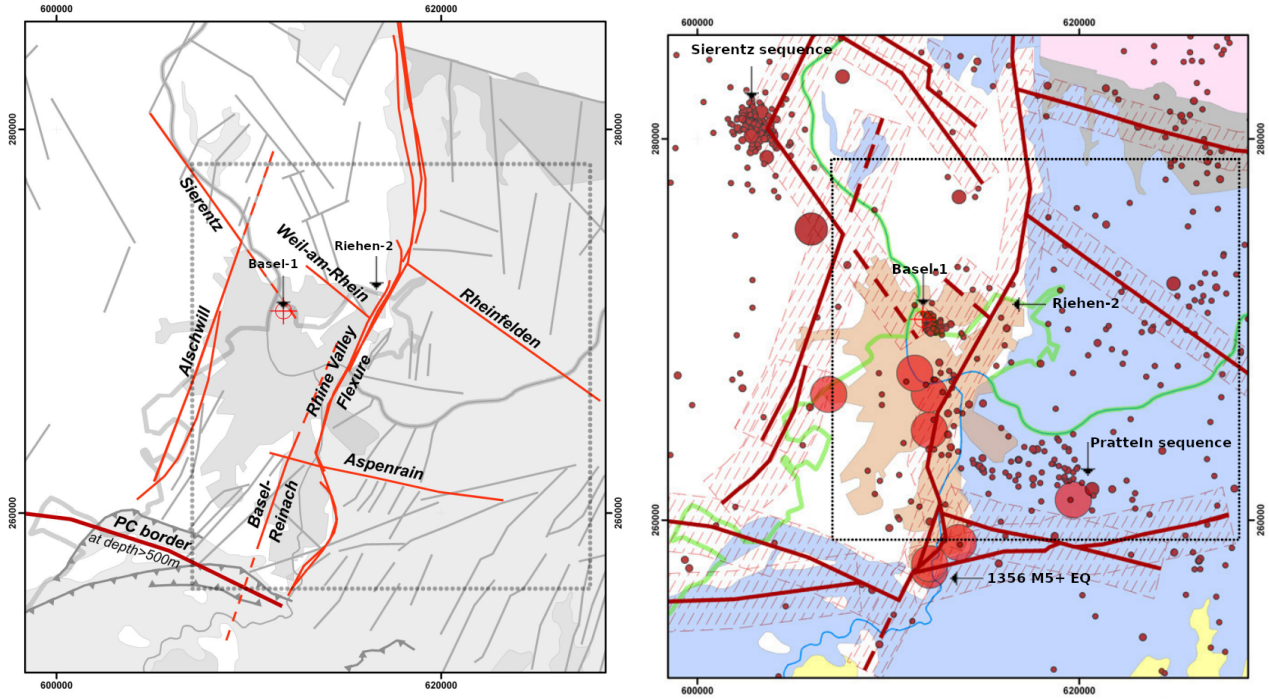


Figure 2.7: Interpreted cross-section through the cyan dashed line of Figure 2.6, modified from Michel et al. [2017].



(a) Faults mapped at the surface

(b) Faults mapped at 5 km depth with historical seismicity

Figure 2.8: Distribution of known faults in the Basel area, according to Delacou et al. [2009]. a) Surface trace of major deep faults used for seismic hazard analysis by SERIANEX in red. Dashed red lines show the hypothesized continuation of faults in areas with no supporting data. Minor or shallow faults in gray. b) Predicted outlines of major deep faults at a depth of 5 km. Dashed bounding boxes represent location uncertainties. Historical seismicity is also shown, with the largest red circles being M>5 events. The dotted rectangle shows our study area for the Riehen NANT experiment. Modified from Delacou et al. [2009].

team leader was previously briefed on the deployment procedure and was assigned a subpart of the network comprising 30 nodes. Actual deployment sites were chosen as close as possible to the planned GPS locations while adjusting for local field conditions and the ability to be as discreet as possible to avoid the chance of equipment disruption or theft. The environmental impact of such installation is minimal, with only a small, shallow hole in the ground required to host the node (about 50 cm deep and 30 cm wide, see Figure 2.9). The top is covered with loose soil and leaves with simple visual markers such as orange flags or rock piles installed to facilitate the recovery of the geophones in the following month. Since some geophones were installed on private properties, consent from the owners had to be requested and we provided an informational flyer (in German, French and English) to give information on the seismic survey and its motivation.



Figure 2.9: Installation of the nodal geophones in the field in Aargau in December 2020. The second picture shows a geophone installed in a shallow hole about a foot deep, which is then completely covered with soil.

The recovery campaign took place over a longer period (January 10th to February 4th, 2021), requiring several distinct trips due to difficult weather conditions and the lesser availability of the deployment team members (and heavy snowfalls). Only two people at a time were mobilized for the retrieval. Despite the various precautions taken during deployment, two nodes were stolen, but one was subsequently recovered. Six nodes were found disturbed, completely pulled out of their hole which compromised the recorded data quality of these sensors. Ten other nodes were found with the soil cover removed, indicating possible human or animal disturbance. During node recovery, each team carefully took notes of the site conditions and re-measured the sensor's magnetic north alignment, tilt and coupling to aid in estimating the reliability and quality to be expected from the recorded data. The horizontal component data of 54 nodes had to be corrected to account for a misaligned north. Figure 2.10 depicts the 210 nodal locations and the number of days of data extracted from each node. The black squares and triangles indicate permanent seismometers and accelerometers respectively, operated by the Swiss Seismological Service (SED). Almost all nodes recorded at least 28 days of data between December 5, 2020, and January 5, 2021, with only a few nodes recording fewer perhaps due to GPS connection issues caused by a burial depth too great, an incorrect setup or partially depleted battery. All nodes could be deployed close to the planned coordinates, resulting in an even spatial distribution.

2.4 NANT deployment in Riehen

The field campaign in Riehen was logistically more complicated than in Aargau in several regards. First, this campaign was only able to occur in September 2022, 2 months before the planned conclusion of PSIGE, due to multiple delays in concluding a contract with Wärmeverbund Riehen AG. In late May 2022, the contract was signed and several weeks later we received recommendations from Wärmeverbund Riehen AG regarding permitting, communication and first points of contact. Since the 3-D seismic campaign had been conducted only a few months prior, the previous permitting information gathered by their subcontractor, Geotest, greatly helped us select public parcels in Riehen and Basel Stadt where we could deploy our geophones under a tight timeline. However, this permitting information did not cover the entire network area that was needed to image the subsurface up to 2 kilometres in depth (the maximum penetration depth of 2 km was suggested by Wärmeverbund Riehen AG).

The network diameter of the deployment is about 18 kilometres centred around Riehen, as shown in Figure 2.11, and covers more than a dozen of distinct communities across three countries, Switzerland, Germany and France. As some of these communities are dense urban environments where it is more difficult or impossible to improvise, we needed a different planning approach than in Aargau. Instead, we sought to obtain permission in advance for every potential node location to minimize the risk of theft and ensure local laws are respected. Hence, a significant amount of work was spent in July and August 2022 researching, for example, cadastral surveys for adequate public property parcels where we could potentially place our nodes and seek the right

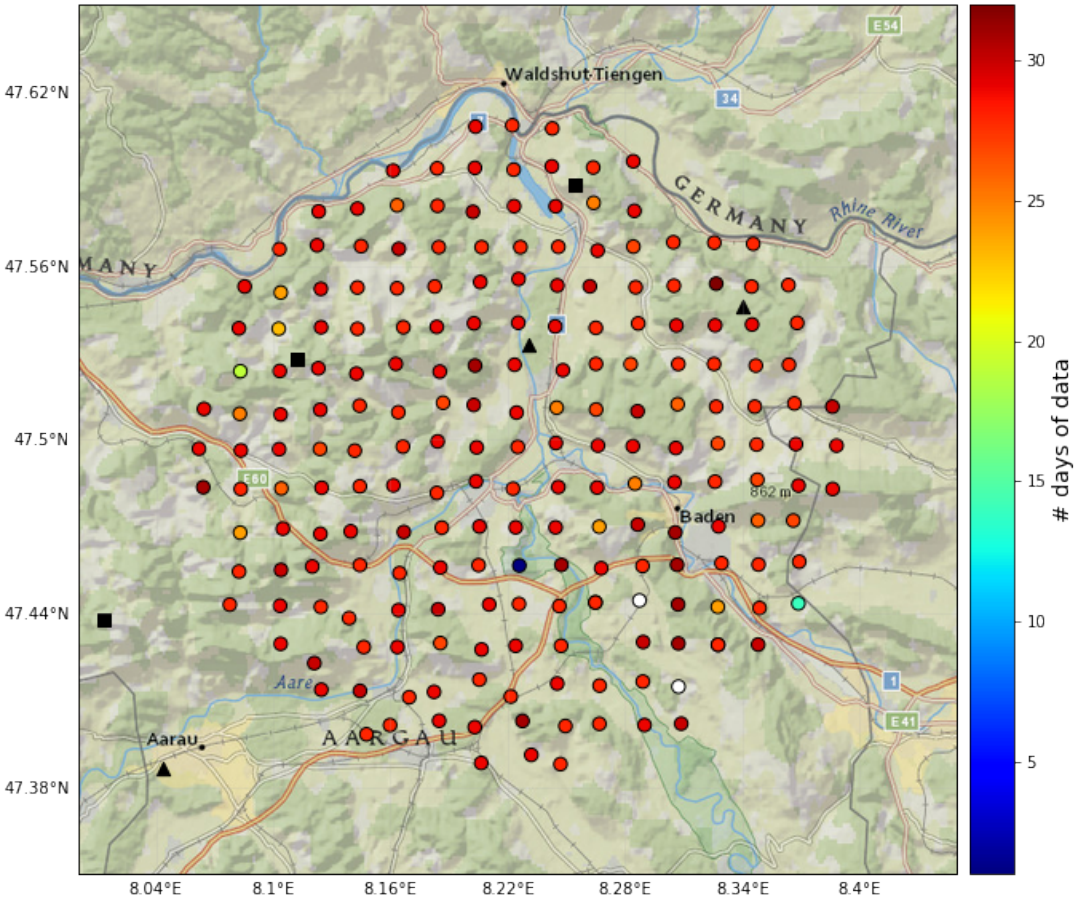


Figure 2.10: Aargau network geometry with the number of days of data collected for each deployed node. The two white circles are nodes for which no data could be retrieved. Black squares and triangles indicate permanent seismometers and accelerometers operated by the Swiss Seismological Service (SED).

administrative people in each community to reach out to. Our planning timeframe coincided with the start of the summer holiday season, which slowed down communication channels significantly and made it difficult to gather all the necessary permissions. In potential future NANT campaigns, more time for the permitting process should be allowed, and a better time for a campaign would be late Fall or early Winter. It is worth mentioning that many communities in Germany and France that we contacted showed interest in our project and requested to have access to our tomography results once the Riehen study is completed. A local German newspaper also made a short article about our experiment.

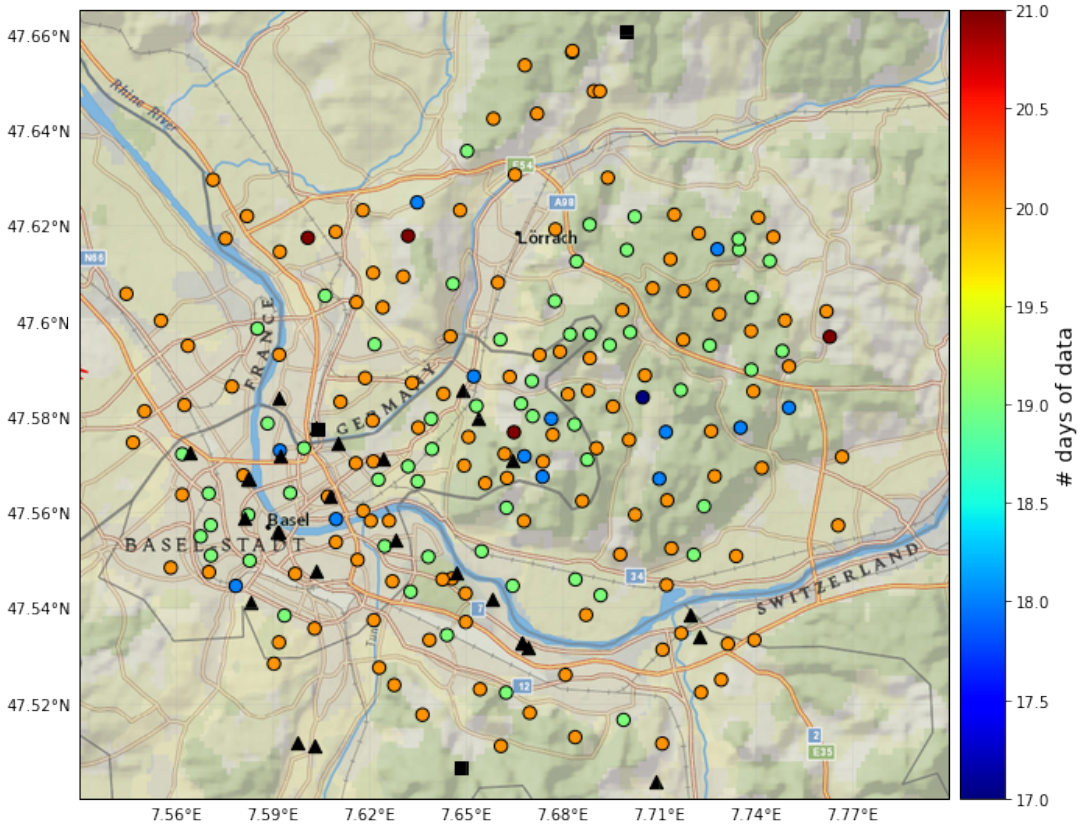


Figure 2.11: Riehen network geometry with the number of days of data collected for each deployed node. Black squares and triangles indicate permanent seismometers and accelerometers operated by the Swiss Seismological Service (SED).

Thankfully, we were able to deploy 200 nodal geophones in late August 2022. As for the Aargau deployment, we were able to recruit young graduate students from our department to help in the field (Figure 2.12). The human resources required were quite similar to Aargau, with 7 teams of 2 people deploying about 15 to 20 nodes per day on average. All 200 stations started recording continuously on September 3 for up to 21 days. The number of recording days for Riehen is smaller than Aargau as the geophones were set to a different GPS setting (Table 2.1) to prevent potential time synchronization issues. Three nodes deployed and recovered did not record any data, perhaps due to errors during setup or equipment malfunction. As shown in Figure 2.11, the distribution of nodes in Riehen is rather uneven compared to Aargau due to the many land access restrictions we had to consider, but our approach allowed the deployment to go smoothly. We also took care to attach information cards that were buried together with the geophone containing information about the goal of the experiment, the nature of the instrument and recorded data along with contact information. We believed this may have helped prevent theft or misunderstandings with residents and passersby as we lost no station.

For both the Aargau and Riehen deployments, recruiting graduate students to help us provided them with a unique experience to get fieldwork experience with seismic deployments and get acquainted with the related methods and instruments. Some of these students have taken on master's projects related to nodal geophone arrays and NANT. Participation in these field campaigns may thus spark curiosity and motivate some students to pursue a career in Geophysics.

2.5 Quality control and data preparation

As mentioned previously, during the recovery of the nodes at Aargau and Riehen, field notes were taken to verify the orientation of the North arrow and tilt of the geophones and report any signs of them being taken out



Figure 2.12: Installation of nodal geophones in September 2022 in the area around Riehen, including Basel-Stadt and Basel-Landschaft, Germany and France

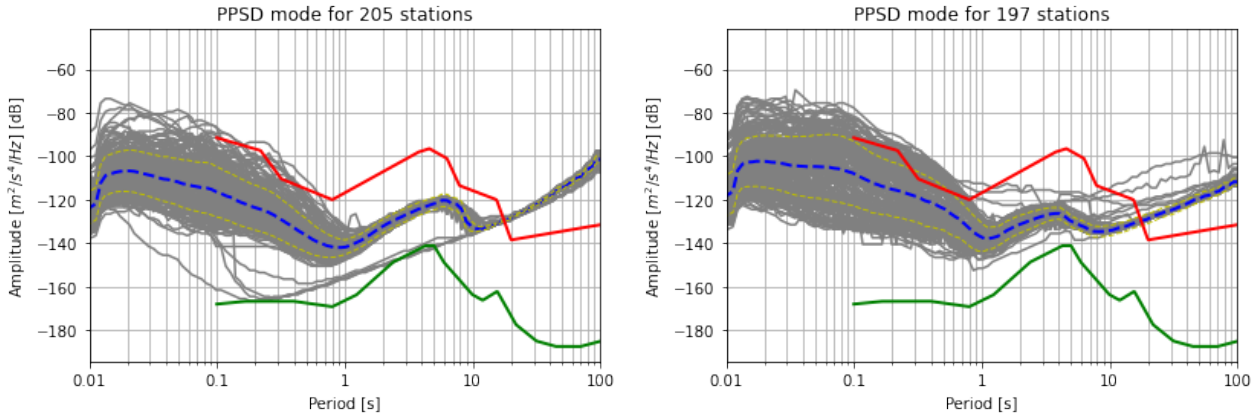
of the ground or disturbed during the recording period. The SmartSolo IGU units also provide a log file where the GPS, position and temperature sensors write information approximately every 10 minutes during recording. Inspection of the metadata gives us a quantitative way of ensuring the data quality of every geophone. This allows us to confirm when/if a node was disturbed and if ground coupling was poor, so corrupted data can be discarded. An example of a metadata log for one of the geophones at Riehen (which was suddenly titled during the experiment around September 16) is shown in the appendices in Figure A.1.

In all, a total of 190 stations were retained for further processing for Aargau, and 220 stations for Riehen, where we benefit from the numerous permanent stations from SED that were operating during our deployment that we combine with our nodal dataset.

3. Methodologies

3.1 Seismic ambient noise conditions

We can make several comparisons between the two datasets in terms of data quality and noise conditions. Figure 3.1 shows the probabilistic power spectral density recorded by all stations, with each grey curve representing the mode of distribution over the entire recording period for a given station. At around 10 seconds, the increasing power with an increasing period is due to the instrument self-noise in both cases. At the lowest frequencies (highest periods) which are commonly used for NANT, between 2 and 10 seconds, there is higher noise and less amplitude variation across stations in the Aargau dataset than in Riehen. This is likely due to the experience in Aargau taking place during the month of December as the sources of ambient noise in this microseismic frequency band, storms in the northern Atlantic, are stronger in winter.



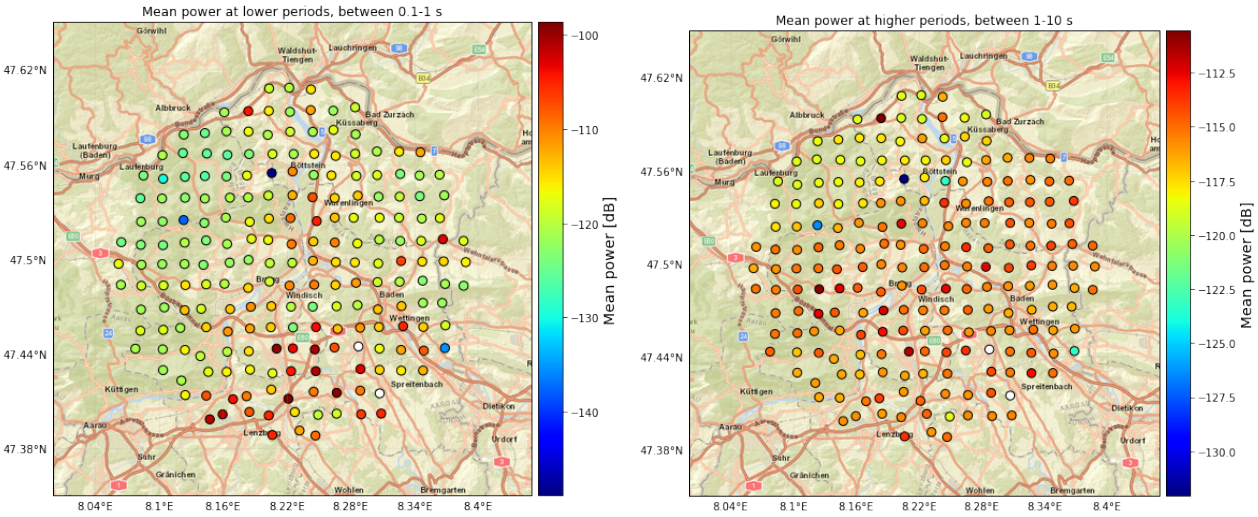
(a) Aargau

(b) Riehen

Figure 3.1: Noise Probabilistic Power Spectral Density (PPSD) in Aargau and Riehen on the vertical component of the 5 Hz geophones. For each station, the mode of all PPSD curves (one per 1-hour-long segment of data) is shown (gray lines). The red and green lines indicate the global High Noise Model and Low Noise Model of McNamara and Buland [2004], while blue and yellow dashed lines are respectively the mean and the power at plus or minus one standard deviation of all PPSD curves.

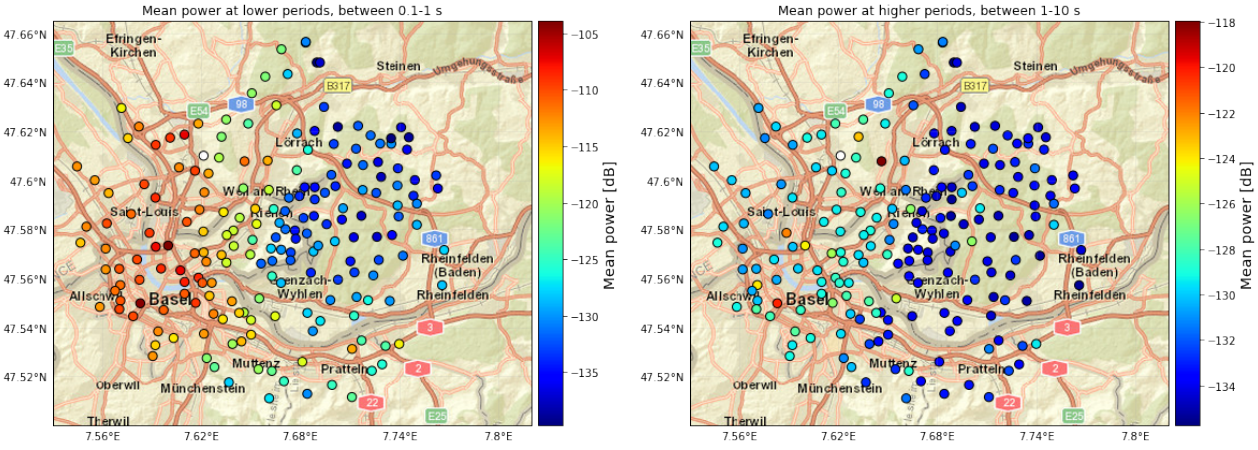
Spatially, the mean power at low frequencies is relatively homogeneous for Aargau as shown in Figures 3.2, apart from the northernmost part of the network in a more forested area that is slightly quieter. In contrast, the spatial distribution of noise intensity is much more heterogenous in Riehen (Figure 3.3). In particular, the contrast between noise conditions recorded at stations in the Dinkelberg forests, Germany, and the stations within the city of Basel, Weil am Rhein and France is obvious. The same pattern is seen at higher frequencies, between 1 and 10 Hz (0.1 and 1 s) where body wave energy is expected in the ambient noise coda based on previous studies. As expected, we see from these maps that anthropogenic noise in this frequency band is contributed by local highways, airports, train tracks, industrial activity, etc. In our application of local ambient noise tomography, our period band of interest, which depends on network configuration, is from around 0.5 to 6 seconds.

In both the Aargau and Riehen experiments, a few permanent velocimeters and accelerometers from the SED were located close to our geophones. Figure 3.4 compares the noise power spectral density between broadband station ACB and a nearby geophone. The 5 Hz geophone has a decreasing sensitivity for periods above 0.2 s due to its instrumental response function. Nevertheless, we can see that the noise power amplitude at periods up to 5 s is remarkably similar to the broadband sensor. In Figure A.2, the spectral amplitude variations over the course of the one-month deployment are shown. An increased amplitude at periods between 3-10 s is observed around December 26-28, 2020 likely due to an ocean storm in the North Atlantic. This event is visible on both the geophone and broadband records. These observations are consistent with a similar



(a) 0.1-1 s (b) 1-10 s

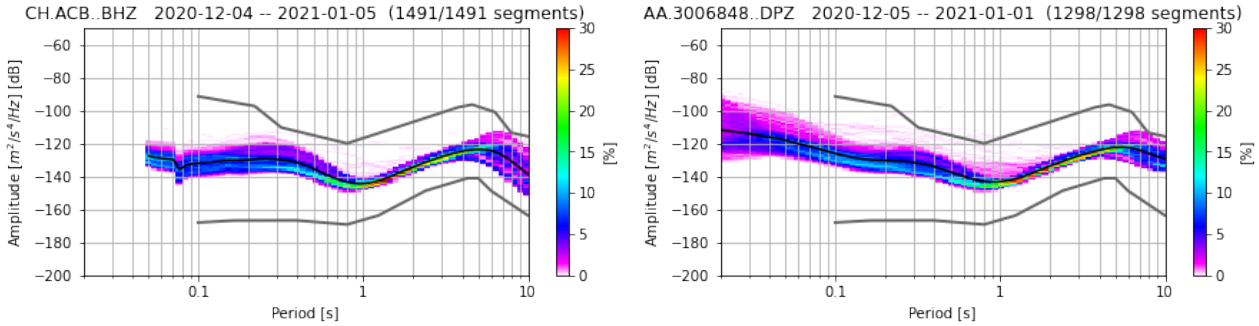
Figure 3.2: Mean PPSD power at each station in the Aargau nodal network in different period bands. Note in panel b the higher energy retrieved from the urban areas of Basel (compared to the countryside regions of Loerrach)



(a) 0.1-1 s (b) 1-10 s

Figure 3.3: Mean PPSD power at each station in the Riehen nodal network in different period bands. Note in panel b the higher energy retrieved from the urban areas of Basel (compared to the countryside regions of Loerrach)

comparison done by Lehujeur et al. [2018], and demonstrate that the use of 5 Hz geophones for dispersion measurements at periods of up to at least 5 s is reasonable.



(a) Broadband station ACB (Nanometrics Trillium 240 s)

(b) SmartSolo 5 Hz geophone (3007367)

Figure 3.4: Comparison of the PPSD for SED broadband station ACB and a geophone located close by between December 4 2020 and January 5 2021.

3.2 Wavefields retrieved from ambient noise and directivity analysis

3.2.1 Cross-correlation and stacking methods

The first step of NANT is to retrieve coherent surface wave arrivals across the network from the recorded ambient noise. This is accomplished by cross-correlating and stacking the continuous waveforms between all station pairs over the entire recording period. Different approaches for pre-processing and cross-correlation are described and discussed in Bensen et al. [2007]. Spectral whitening and temporal normalization are usually applied to reduce the unwanted effect of transient signals such as earthquakes and instrument irregularities and enhance the bandwidth of the recorded ambient noise. I chose to apply spectral whitening using a running mean average scheme to preserve both phase and amplitude information, which is strictly equivalent to coherency [Jiang and Denolle, 2020, Prieto et al., 2009]:

$$\bar{C}_{AB}(f) = \frac{\bar{U}_A^*(f)\bar{U}_B(f)}{\{|\bar{U}_A(f)|\}\{|\bar{U}_B(f)|\}} \tag{3.1}$$

where $\bar{U}_A(f)$ and $\bar{U}_B(f)$ are the Fourier transforms of the time seismograms at station A and B respectively, $||$ and $\{\}$ are the absolute value and smoothing operators respectively.

To fully take advantage of the 3 components of the recorded wavefield, I retain relative amplitude information between different components in the following way: the running mean average amplitude on the vertical component is used for the normalization of the horizontal component, so that the rotation of the ambient noise cross-components NEZ system to RTZ preserves relative amplitudes correctly, as suggested in Lin et al. [2014]. Cross-correlations are calculated for 30 min long windows overlapping by 50% and stacked temporally for the entire recording period. The maximum lag time is taken to be +/- 180 s, so the noise window used for calculating the signal-to-noise ratio of the cross-correlations is not affected by the coda [Bensen et al., 2007]. Individual cross-correlations with anomalous amplitudes more than 10 times above the median absolute deviation are discarded. For stacking, I have tested different methods, including a simple linear stack (geometric mean), phase-weighted stacking [Schimmel and Paulssen, 1997], robust stacking [Yang et al., 2020] and an auto-covariance filter technique [Nakata et al., 2015]. I found that phase-weighted stacking provided the best signal-to-noise ratio, which is defined as:

$$g(t) = \frac{1}{N}\sum_{j=1}^{N} s_j(t)\left[\frac{1}{N}\sum_{k=1}^{N} \exp\left(i\phi_k(t)\right)\right]^2 \tag{3.2}$$

where ϕ is the instantaneous phase of the analytical signal corresponding to the observed seismogram s with N time samples. Due to the huge number of calculations needed to build the cross-correlation stacks, it is essential to leverage parallel computing resources. MPI is used to parallelize this step using a modified version of the NoisePy codes [Jiang and Denolle, 2020] that I have adapted to our own pre-processing requirements. The computation is carried on UniGe's high-performance computing (HPC) cluster Yggdrasil, where a few hundred of CPUs can be leveraged simultaneously.

The final cross-correlation tensor comprises 9 cross-components after rotation: ZZ, ZR, RZ, RR, RT, TR, TT, ZT, TZ, where R refers to the radial component, T is the transverse component and Z is the vertical component.

When looking at positive lag times, the first letter in the cross-component refers to the component of the "source station", while the second refers to the component of the "receiver station". For example, ZR is the cross-correlation of the vertical component at the first station with the radial component at the second station.

Figure 3.5 shows the symmetric cross-correlation tensor for the Aargau dataset while the Riehen dataset is shown in Figure 3.6. "Symmetric" cross-correlations mean the positive (causal) and negative (acausal) time lags were averaged to reduce the effect of the uneven noise distribution around the stations. The cross-correlations shown in these figures are binned into inter-station distance intervals of 150 m to increase signal-to-noise ratio [Nakata et al., 2015]. Each bin stack is normalized by its maximum amplitude for visualization purposes.

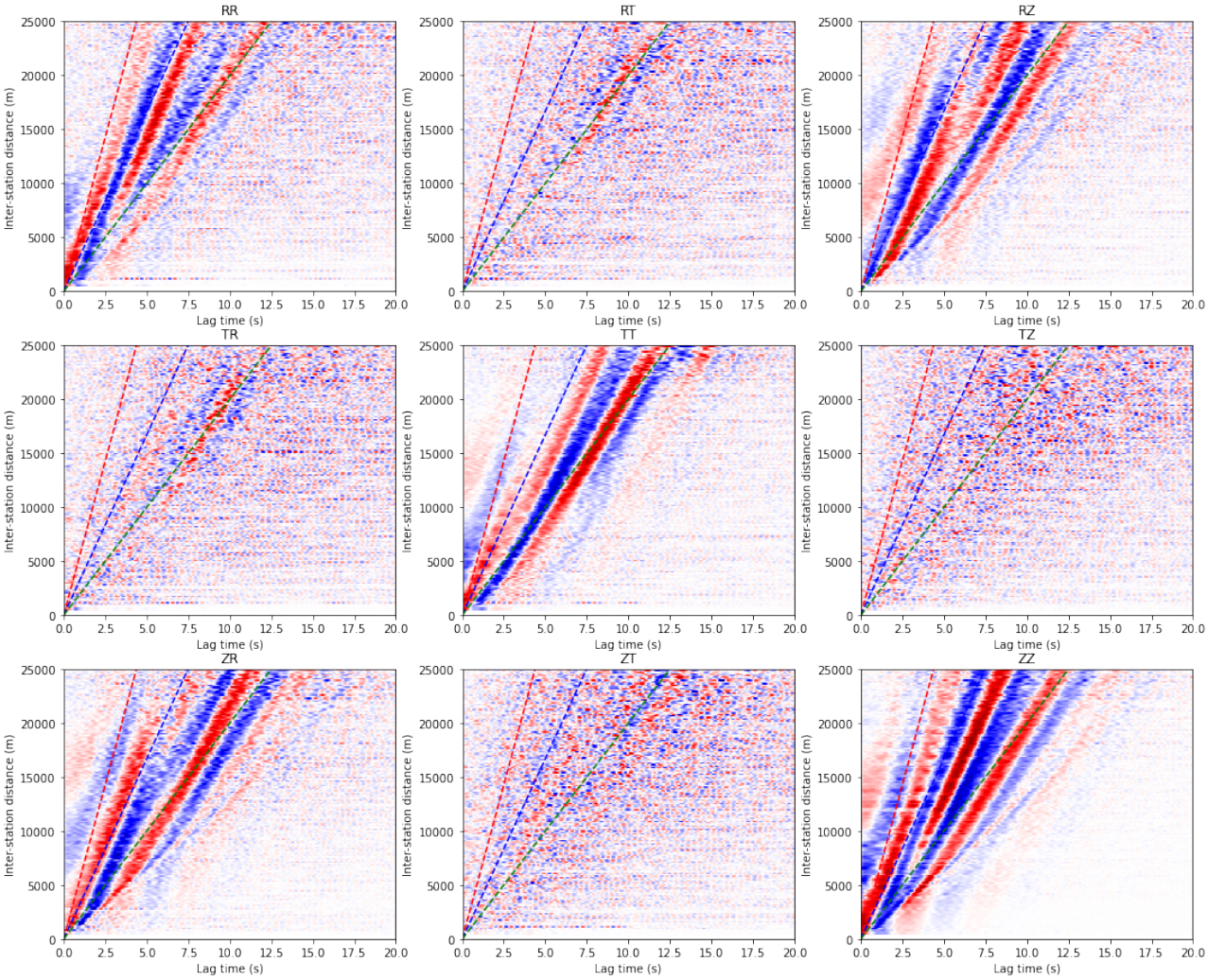


Figure 3.5: Symmetric stacked cross-correlation tensor for the Aargau dataset. The cross-correlations are stacked over the entire 1-month recording period. The red and blue dashed lines indicate velocities equal to P-wave and S-wave average velocities in this area, (5.7 and 3.3 $\mathrm{km\,s^{-1}}$, respectively) according to the latest 3D Swiss velocity model of Diehl et al. [2021] The green line show a velocity of $2\,\mathrm{km\,s^{-1}}$. Red and blue indicate positive and negative amplitudes respectively.

The energetic arrivals on different cross-components as a function of inter-station distance and frequency allow the identification of different seismic wave types. The theory of ambient seismic noise for a diffuse wavefield states that the negative time derivative of the cross-correlation is related to the empirical Green's function for a point force at the first station recorded at the second station [Snieder, 2004]. This is key to interpreting the energy measured on the different cross-component: assuming an isotropic subsurface, cross-components ZZ, ZR and ZT show the wavefield that would be generated by a vertical point force at station 1 (source) on the Z, R and T components of station 2, respectively. We can then expect Rayleigh surface waves to appear on the ZZ, ZR, RZ, and RR components, while the Love waves should appear on the TT cross-component. High energy on the ZT, TZ, RT and TR cross-components could be sign of anisotropy or incorrectly oriented North direction of the sensors that cause Love waves energy to leak on the ZZ, ZR, RZ and RR cross-components (and vice-versa for Rayleigh waves) or could be due to 3D heterogenous velocity structure effects [Nayak et al., 2018, Maupin and Park, 2007]. See Table 3.1 for a hint on how to read different cross-components in terms of source and receiver. Note that due to the reciprocity of Green's function, swapping the order of the cross-components

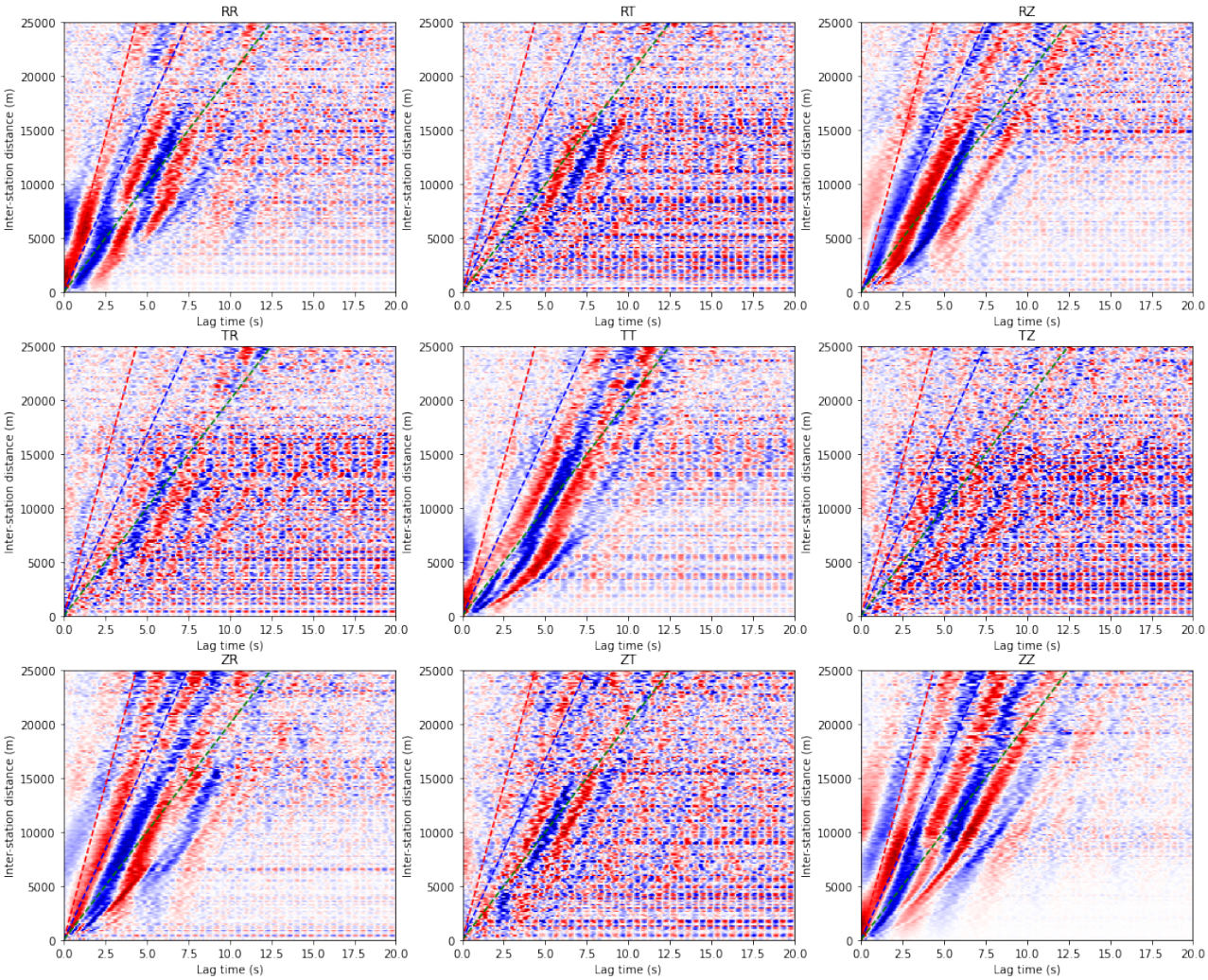


Figure 3.6: Symmetric stack cross-correlation tensor for the Riehen dataset. The cross-correlations are stacked over the entire 1-month recording period. The red and blue dashed lines indicate velocities equal to P-wave and S-wave average velocities in this area, (5.7 and 3.3 km s^{-1}, respectively) according to the latest 3D Swiss velocity model of Diehl et al. [2021] The green line show a velocity of 2 km s^{-1}. Red and blue indicate positive and negative amplitudes respectively.

is equivalent to swapping the first station to be the receiver and the second station to be the source.

		Point force source		
		Vertical	Radial	Transverse
Component	Vertical	ZZ	RZ	TZ
	Radial	ZR	RR	TR
	Transverse	ZT	RT	TT

Table 3.1: Interpreting the cross-components of the Green's function tensor when the first station is taken as the virtual source, and the second station as the virtual receiver (positive time lags of the cross-correlations). In an isotropic medium, Rayleigh wave energy should appear on cross-components highlighted in green and Love wave energy on the one in cyan.

3.2.2 Surface wave observations

Despite the different noise conditions between the two datasets and differences in the number of recorded days, Figure 3.5 and 3.6 show there is a strong surface wave energy observed in the cross-correlations in both cases with a clear dispersive character.

For the Aargau dataset, the strong energy on the TT components with an apparent speed of about $2\,\mathrm{km\,s^{-1}}$ along with the very low coherent energy on the RT/TR and ZT/TZ cross-components demonstrate the fundamental mode Love waves can be confidently retrieved from this dataset. In the appendix, Figure B.1 shows the frequency-wavenumber (FK) decomposition of these cross-correlations stacks, which helps separate the different surface wave mode contributions observed. For the Rayleigh, the strong coherent energy on the ZZ, ZR, RZ and RR cross-components, but more than one coherent move-out can be distinguished and distinct "branches" on the FK plot. This could be the sign that different modes are observed (fundamental and 1st higher mode) but could also be due to strong geological contrasts in the study area. This hypothesis is examined further below.

For the Riehen dataset, there is more energy leaking on the TZ/ZT and RT/TR cross-components, which makes the observations of distinct Love wave dispersion properties more uncertain. For the Rayleigh waves, multiple coherent move-outs can be seen and as in Aargau, this can be an indication of either multiple modes or contrasting geology. The maximum inter-station distance between two nodes is about 18 km. Thanks to the permanent stations of SED, we can extend the dataset to longer move-outs, although with decreasing signal-to-noise ratio due to the lower number of measurements, as can be seen on Figure 3.6 for inter-station distance between 18-25 km.

For seismic tomography, the dispersion characteristics for all these different wave types can be measured and combined into a joint inversion to improve inversion constraints and diminish model non-uniqueness.

3.3 Noise directivity analysis

The directivity of ambient noise sources for the frequency band commonly used for ANT is well known, they predominantly come from standing waves in the ocean and wave interactions with the seafloor. In the Greater Geneva Basin study by Planès et al. [2020], noise directivity was found to be oriented southeastward, consistent with a dominant noise source in the North Atlantic Ocean. For the Aargau and Riehen datasets, we apply beamforming to reveal the noise directivity and its different contributions and the effect of our noise preprocessing. I follow Bowden et al. [2021] to calculate the beam power P for different incident slownesses $\mathbf{s}$ directly from the ambient noise cross-correlations gathers C_{ij}^{obs} between stations at coordinates $\mathbf{x}$:

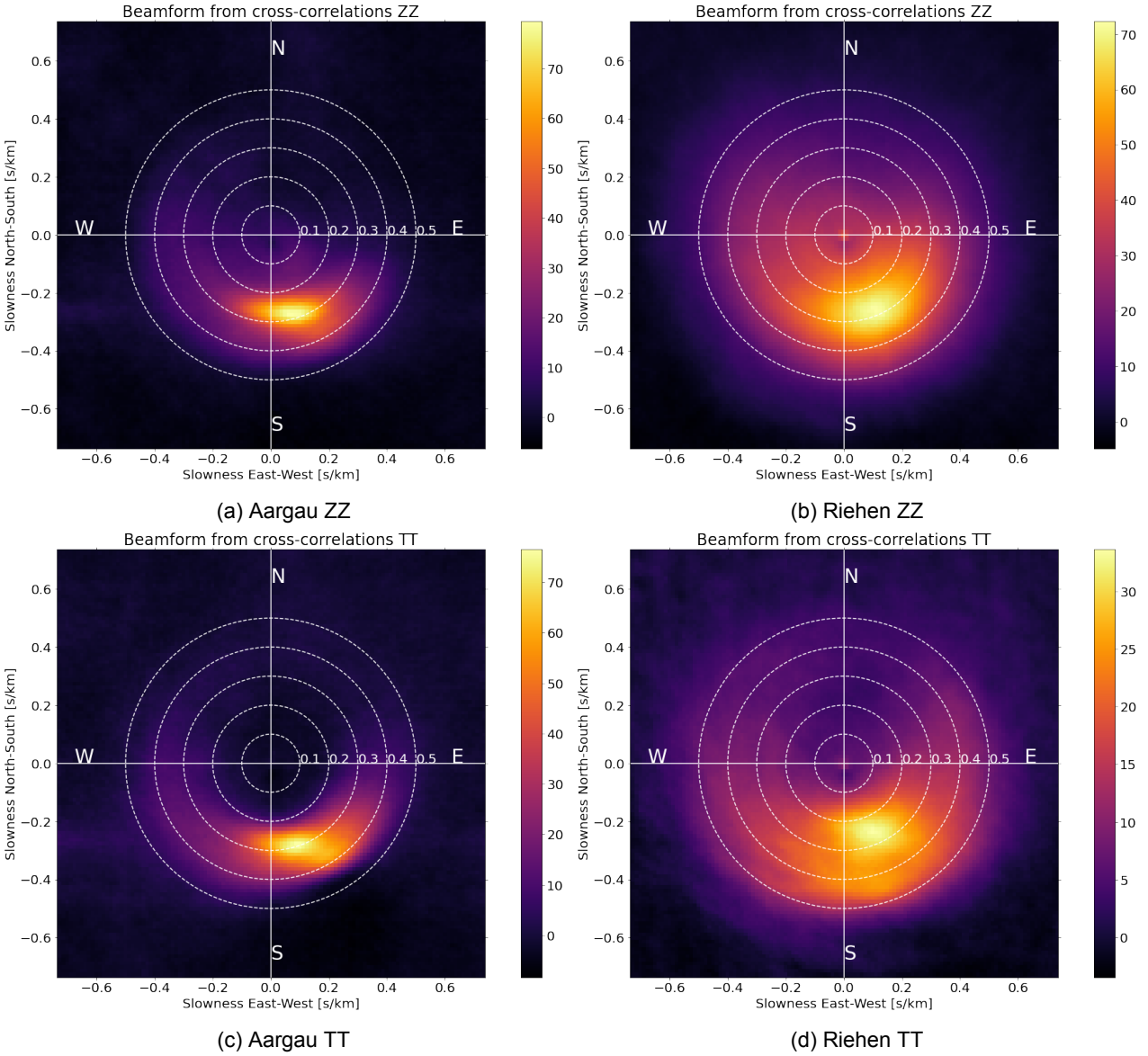
$$P(\mathbf{s}_x, \mathbf{s}_y) = \sum_{i,j} C_{ij}^{obs}(\Delta_{ij}) \tag{3.3}$$

where

$$\Delta_{ij} = \mathbf{s}^T(\mathbf{x}_i - \mathbf{x}_j)$$
$$C_{ij}^{obs} = \int u(\mathbf{x}_i, t - \Delta_{ij}(\mathbf{s}))u(\mathbf{x}_j, t)\,\mathrm{d}t$$

Figure 3.7 shows the beamforming results for the vertical and transverse components applied to our processed, stacked cross-correlations. High beam power in the southeast quadrant at a slowness of around 0.3

s/km indicates surface wave energy is incoming from the NW predominantly for both experiments, consistent with a persistent ambient noise source in the northern Atlantic Ocean. However, the Riehen beamforming results indicate a more azimuthally spread-out ambient noise field, with diffuse contributions coming from almost all azimuths for both Rayleigh and Love waves. A more homogeneous distribution of noise sources is considered more favourable for ambient noise tomography, as the cross-correlations are closer to being accurate Green's function approximations (see e.g. Bensen et al. [2007]). Many studies have however shown that stacking the positive and negative lags alleviate the effects of a heterogeneous distribution of noise sources, which is the approach we take (e.g. Bensen et al. [2007], Hillers et al. [2013], Planès et al. [2020]). A sufficiently strong ambient noise power and the natural scattering properties also help alleviate the effect of the inhomogeneous distribution on retrieving Green's functions [Yang and Ritzwoller, 2008]. However, this solution is debated in other studies where a joint inversion for source directivity is recommended instead (e.g. Lehujeur et al. [2017]).



(a) Aargau ZZ

(b) Riehen ZZ

(c) Aargau TT

(d) Riehen TT

Figure 3.7: Beamforming of the stacked ambient noise cross-correlations for the vertical and transverse components. Colour is proportional to beam power, with higher values indicating a stronger contribution from a noise source in this position in the slowness domain. Concentric white circles correspond to slowness magnitudes of 0.1 to 0.5 s/km.

3.4 Local seismicity during the deployments

The presence of local earthquakes was investigated for both datasets, as earthquakes might influence the stacked cross-correlations if the pre-processing is not adequate.

For Aargau, using an STA-LTA detection algorithm [Trnkoczy, 1998], only two local events were found during

the whole duration of the experiment, which were confirmed to be blasts from the local Gabenchopf quarry in the SED earthquake catalogue (December 10 and 17 at around 1 PM CET).

For Riehen, the timing of our experiment benefited from an exceptional coincidence with the occurrence of a magnitude 4.7 ML earthquake on September 10, 2022, at a depth of 13 km[1], near Mulhouse, France, with the epicentre located just 7.5 kilometres away from our closest geophone (Figure F.1). It was followed by a sequence of 18 reported aftershocks that were also recorded on our nodal network. Waveforms for the mainshock are shown in Appendix F. While earthquake-based analyses are not the focus of this project, the dataset may be interesting for a follow-up in-depth study on this earthquake sequence. See Appendix F for details.

3.5 Frequency-Time ANalysis (FTAN) and group dispersion picking

The second step towards a final 3-D velocity model is the frequency-time analysis and picking of group velocity dispersion for different periods. For different wave types and different modes, surface waves will sample a different depth range of the subsurface for a given period. Figure 3.8 shows the sensitivity kernels for group velocity to shear wave velocity structure along depth. The kernels were calculated with the GPU-accelerated disba[2] software using the minimum 1-D shear wave model for Switzerland of Husen et al. [2011]. For Rayleigh waves of a given period, the kernel shows peak sensitivity to shear-wave structure around depths equal to one-third to one-half the period.

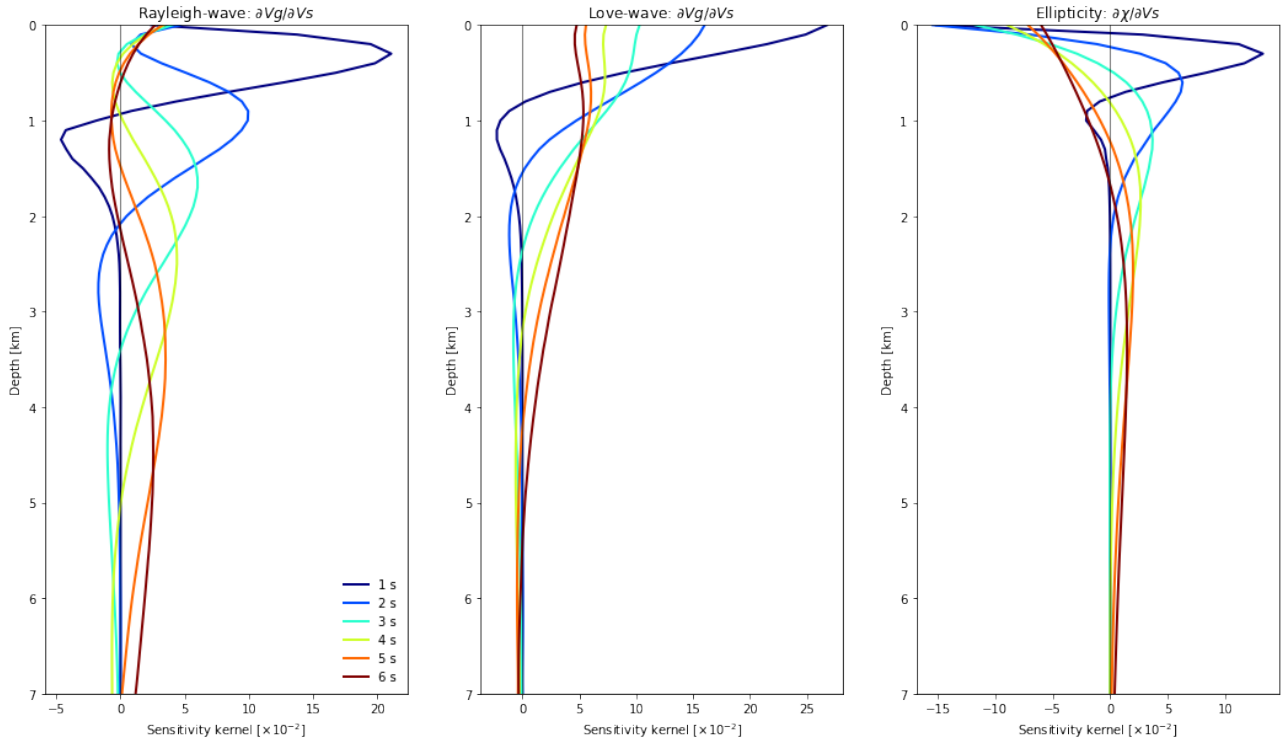


Figure 3.8: Group velocity sensitivity to 1-D shear wave structure for fundamental mode Rayleigh and Love wave dispersion and ellipticity (H/V ratio) calculate with the Swiss 1-D velocity model of Husen et al. [2011].

Dispersion diagrams are obtained through Frequency-Time ANalysis (FTAN) of the cross-correlation functions. The purpose of FTAN is to unravel the propagation of the different frequency components of surface waves [Levshin et al., 1989, Bensen et al., 2007]. FTAN produces for a given cross-correlation function a spectrogram that may reveal the dispersion of different modes of surface waves propagating between the two stations. Instead of using Fourier transforms and narrow-band Gaussian wavelets, I use the continuous wavelet transform as our time-frequency decomposition method [Jiang and Denolle, 2020, Fichtner et al., 2008]. More specifically the Morlet wavelet is selected for the transformation, with the default scaling parameters implemented in the Python package *pycwt*.

[1] https://www.emsc-csem.org/Earthquake/earthquake.php?id=1167423
[2] https://github.com/keurfonluu/disba

3.5.1 Picking approaches

Many ambient noise tomography studies restrict their picking measurements to the vertical-vertical ZZ cross-components. As mentioned previously, Rayleigh wave energy can be observed on multiple cross-components, ZZ, ZR, RZ and RR. Some authors have taken advantage of 3-component records and the redundancy of these cross-components to increase the signal-to-noise ratio of FTAN images and reduce artifacts in the dispersion curve picks. For example, Zigone et al. [2015, 2019] compute the normalized FTAN diagram of each of the four cross-components and for each lag time type (causal and acausal) and then combine these 8 individual images ($N_i(f,U)$) into one ($A_s(f,U)$) using the logarithmic stacking method of Campillo et al. [1996]:

$$A_s(f,U) = [\prod_i N_i(f,U)]^{1/8} \tag{3.4}$$

In Figure 3.9, we show the FTAN images for the 4 individual cross-components and the logarithmic stack of the ZZ*ZR and ZZ*Z*RZ*RR components for a station pair 21.45 km apart from the Aargau nodal network. We see the individual FTAN images present several jumps in amplitude for different periods that would lead to incorrect dispersion curve picks (black dots). On the two variations of combined images (ZZ*ZR and ZZ*Z*RZ*RR), we see these artifacts are significantly reduced and the smoothness of dispersion curve picks is improved.

Usually, only the fundamental mode of surface waves dominates the FTAN spectrogram in energy, although higher modes may be observed at higher frequencies, especially if the subsurface structure is more complex. The logarithmic stacking approach described above is likely to enhance the fundamental mode energy and reduce inconsistencies due to picks from higher mode waves.

For surface wave tomography, dispersion curves (group velocity as a function of period) must be picked from the FTAN image of every station pair. Usually, the dispersion curve for the fundamental mode, and sometimes the first higher mode, is picked manually by an experimented user. However, for our dense acquisition, the amount of data is too large to make manual picking a reasonable option and automated processing is necessary. Our automated picking procedure is as follows. First, all local maxima in the FTAN diagram are gathered. Instead of employing multiple thresholds on peak width, height and separation to select only significant peaks, we use an algorithm derived from the field of topological data analysis (TDA), which has many applications in data science. More specifically, the “persistent homology” approach allows the detection of peaks that are quantified and ranked by their “significance” [Huber, 2021] using a score from 0 (no peak) to 1 (absolute maximum)[3]. Extracting multiple local peaks from the FTAN image is relevant because the absolute maximum might not always correspond to the fundamental mode, but instead to other local maxima. The advantage of the method of Huber [2021] is that no complex thresholds need to be defined and the ”significance” rank was shown to be more robust to complex peak shapes. The local peaks are then culled and selected based on several deterministic criteria, including curve continuity rules (prevent jumps in velocity > $0.1\,\mathrm{km\,s^{-1}}$), outlier detection, signal-to-noise ratios thresholds (broadband and narrowband) and a requirement to pick at periods for which there is at least 1.5 wavelength for the given inter-station distance (assuming a phase velocity of $3\,\mathrm{km\,s^{-1}}$.

3.5.2 Bi-modal distribution of group velocities

For the Aargau and Riehen datasets, the distribution of measured group dispersion velocities for some periods shows a more complex distribution than is expected if only one surface wave mode was observed propagating in a medium with velocity perturbations around a mean 1D structure following a Gaussian distribution in amplitudes. This may indicate either more than one wave mode is present (e.g. 1st higher mode present or leaking of Love wave energy on other cross-components) or that the velocity structure over the study area shows distinct regions of starkly contrasting velocity anomaly distributions. To examine if the latter hypothesis is correct, the velocity picks for a given period are classified into two groups using Gaussian Mixture Models (GMM) clustering. In Figures 3.12 and 3.13, the ray path density spatial distribution for the slow and fast clusters are mapped separately, along with the distribution of ray path azimuths and path lengths. In both case there is a distinct pattern in the ray path distribution. For Aargau, the slow velocities are concentrated for paths travelling almost exclusively between the Jura Main Thrust and the Mandach Thrust, which corresponds to the location of the Permo-Carboniferous sediment-filled basement trough. It is evident from the distribution of ray path azimuths, that are nearly parallel to the strike of the trough boundaries. For Riehen, another clear pattern is found with ray paths with fast velocities concentrating over the Dinkelberg massif in contrast to slow velocity ray paths concentrating west of the Rhine Valley Flexure, where ray paths travel through the Upper Rhine Graben. The same observations are consistent at other periods, and support the conclusion that the bi-modal distribution of dispersion curve picks is due to contrasting subsurface velocities rather than inaccurate pick identification.

[3] https://www.sthu.org/blog/13-perstopology-peakdetection/index.html

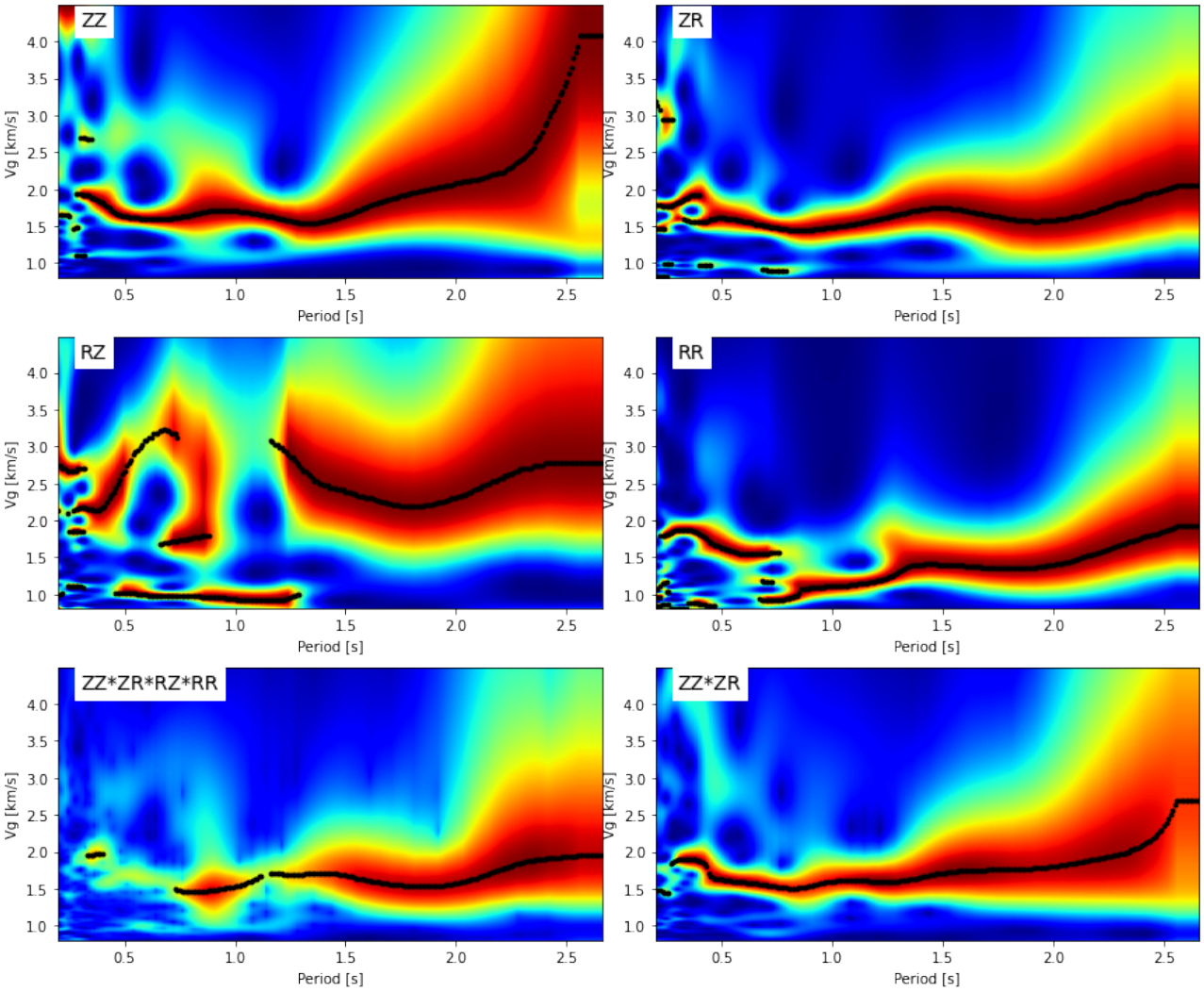


Figure 3.9: FTAN images produced from different stacked cross-correlations for a pair of stations in the Riehen network 11.4 km apart. The picked group velocity with our algorithm is shown as black dots. In some images, the FTAN images of two or more cross-components are multiplied to enhance the signal-to-noise ratio and reduce artifacts.

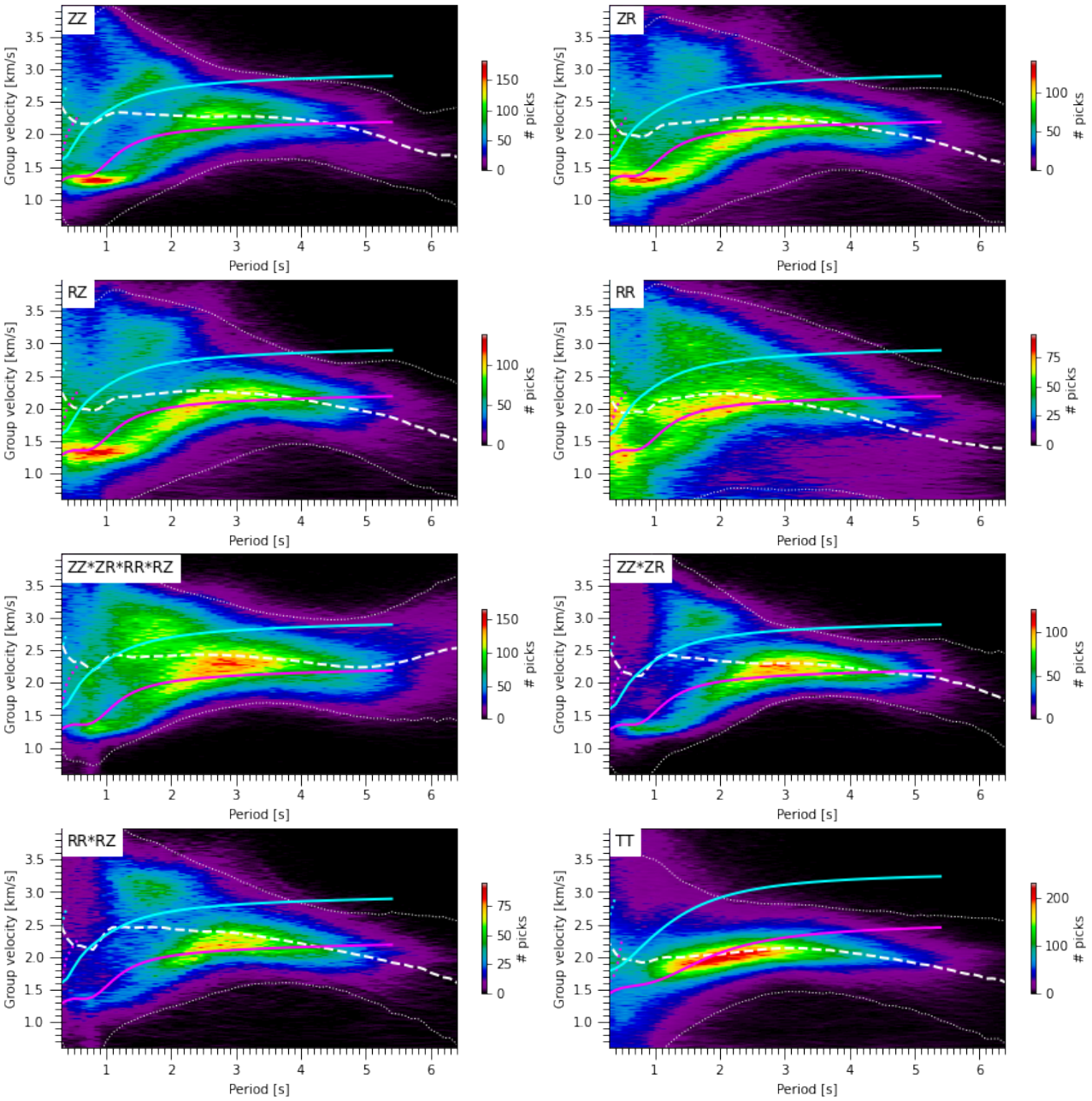


Figure 3.10: Histogram of all dispersion curve picks for all station pairs in the Aargau network using different cross-correlation cross-components. The thick and thin white dashed lines show the mean group velocity for each period and the interval defined by two standard deviations from this mean. The cyan and pink solid lines show the predicted Rayleigh wave fundament mode dispersion from the measured P-wave interval velocities in the well logs of Boettstein and Riniken, respectively, using a constant Vp/Vs ratio.

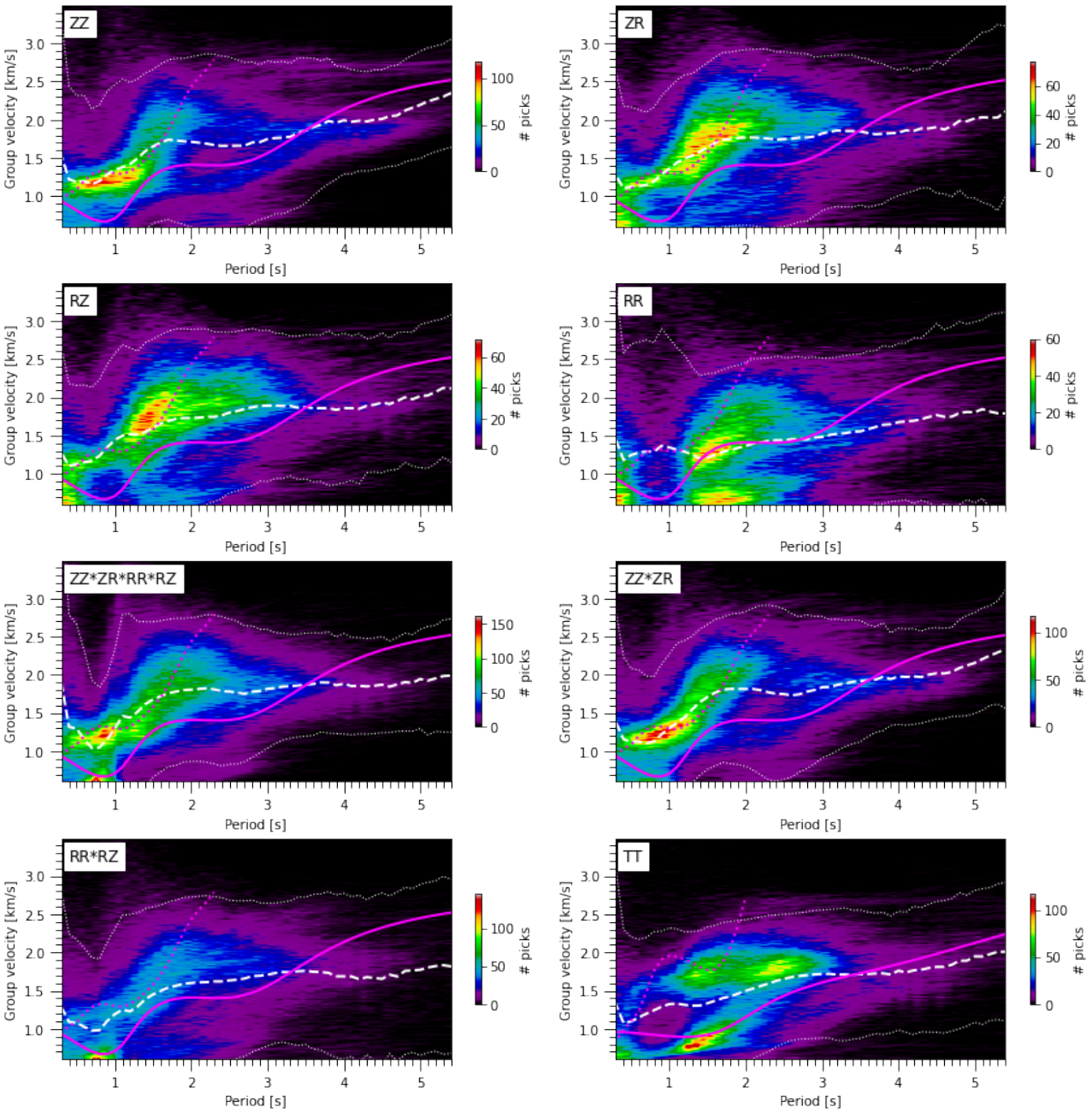


Figure 3.11: Same as Figure 3.10, but for the Riehen dataset. Here the solid and dashed magenta lines refer to the predicted Rayleigh fundamental mode and first higher mode dispersion based on the velocity model of Michel et al. [2017], which is based on the well logs at the Basel-1 and Otterbach-2 deep wells.

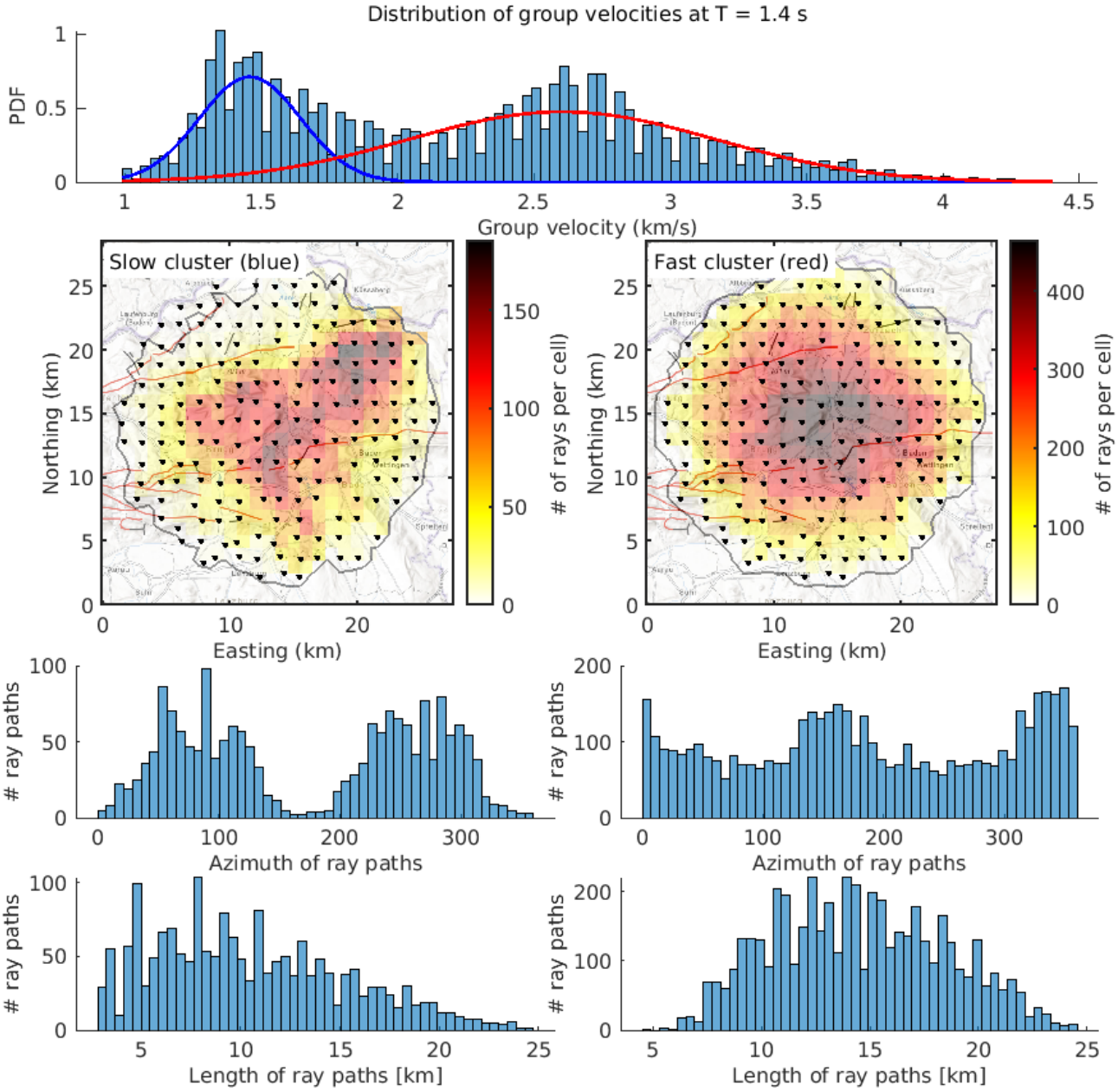


Figure 3.12: Gaussian Mixture Models (GMM) clustering of group velocity picks at a period of 1.4 s for the Aargau dataset. The top panel shows the histogram of group velocity measurements for all station pairs for the given period (shown here as density instead of counts). The blue and red curves show the best fit GMM components that match the data and that are used to cluster the individual picks, with a probability threshold of 70%. The density of ray paths corresponding to the slow (blue curve) and fast (red curve) clusters are mapped and the distribution of azimuths and lengths for these ray paths are displayed below.

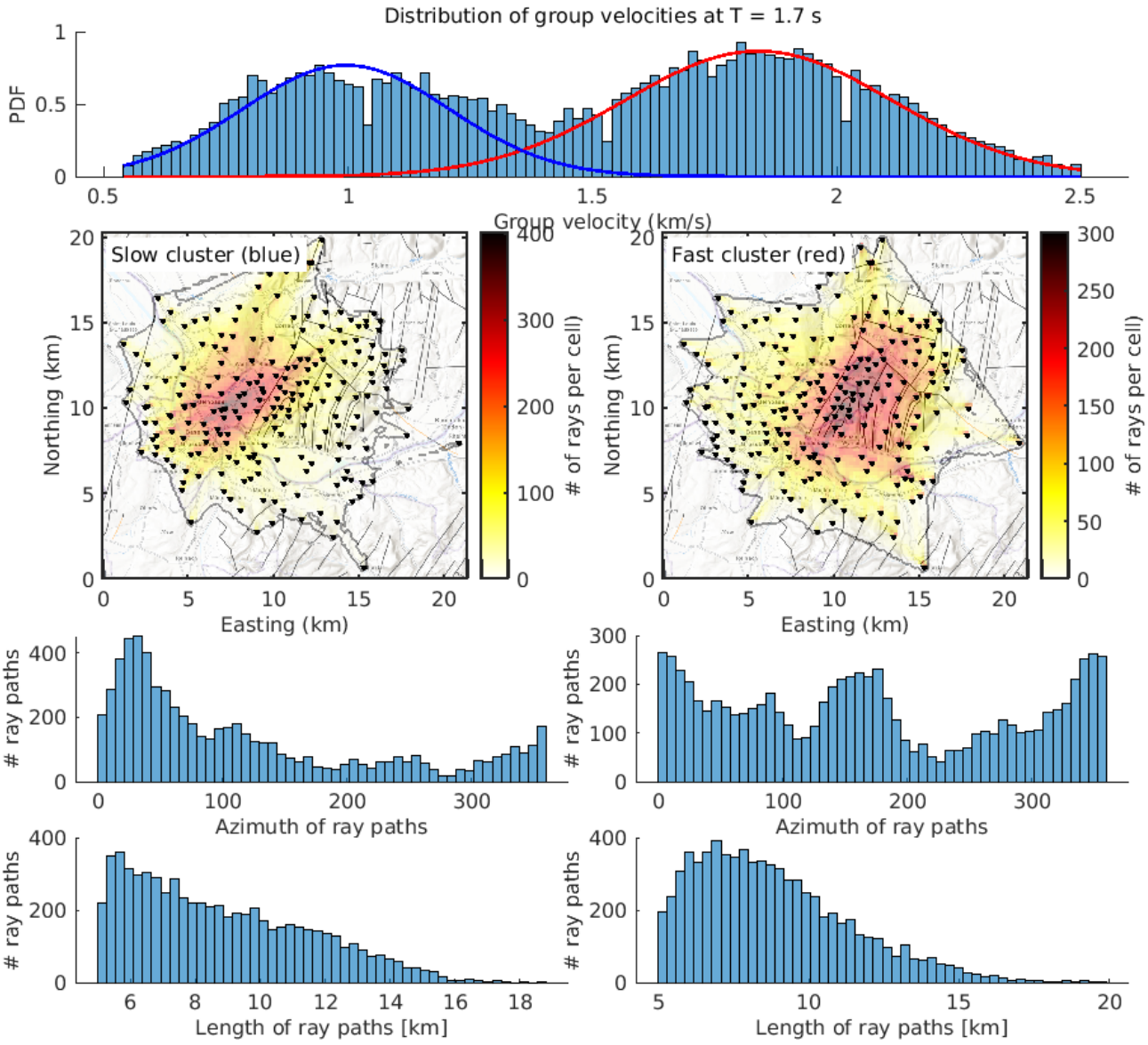


Figure 3.13: GMM clustering of group velocity picks. Same as Figure 3.12 but for a period of 1.7 s for the Riehen dataset.

3.5.3 Outlier rejection

Because the picking approach is fully automated and a manual review of each FTAN pick would be impossible to carry on by one person for such a large dataset, it is important to post-process the picking dataset for outliers. Looking at the measurement distributions in Figures 3.10 and 3.11, one straightforward solution that we can afford thanks to the huge number of measurements is to exclude all measurements falling outside a specified multiple of the standard deviation (σ) around the mean, for each picked period. This outlier filtering can be applied recursively until no additional measurement falls outside the specified bounds. The effect of this filtering is shown in Figure 3.14. For Aargau, a threshold of 3σ is chosen, while for Riehen, a more severe criterion of 2σ helps stabilize the group velocity map solutions.

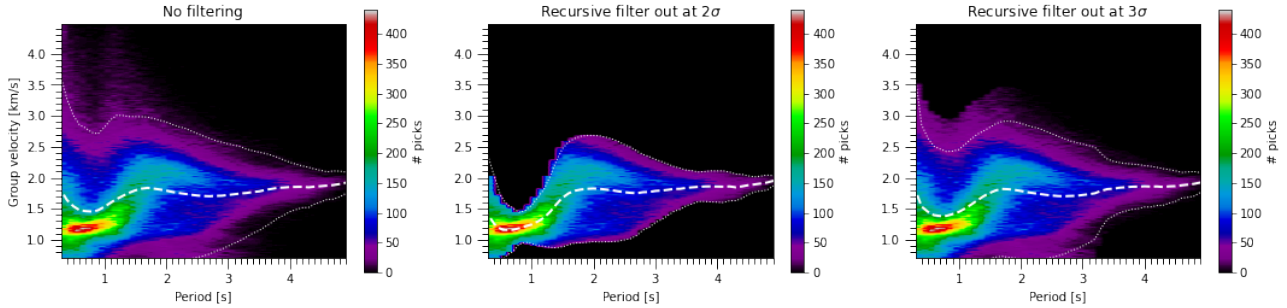


Figure 3.14: Effect of outlier filtering for Riehen group velocity picks (ZZ cross-components) for thresholds of two and three standard deviations (σ). A threshold of 2σ is chosen in this study. The thick dashed white lines show the mean dispersion curves, while the dotted lines show the 2σ threshold limits.

3.6 Group velocity maps

Once group velocity dispersion picks have been gathered for all station pairs, a group velocity map can be derived for each picked period. The dispersion velocity measured between two stations depends on the local group velocity at each point along the ray path, which is a function of the 1-D shear wave velocity structure below that point. The inverse problem for the group velocity map can be formulated this way: given all measurements of group velocity at a given period between all station pairs, find the local group velocity at each point in the study area, which is sampled by multiple ray paths. Given a model parameterization as a discrete grid and an uneven distribution of ray paths, the inverse problems become ill-conditioned due to uneven sampling of each grid cell. Damping is also needed to reduce the influence of data errors. The tomographic technique first presented by Montagner [1986] is an elegant matrix-based approach to this problem. It is derived from the regularized linear least-square inversion formulation of Tarantola and Valette [1982a], which is based on a Bayesian approach to typical nonlinear inverse problems in geophysics [Tarantola and Valette, 1982b]. The objective function assumes data errors have a Gaussian distribution and the least square criterion ensures the best fit while keeping close to the prior model. In this approach, damping and smoothing are applied via data and model prior covariance matrices that have physics-based and intuitively interpreted parameters. The model prior covariance matrix acts as a spatially-varying local smoothing operator to ensure nearby model parameters vary smoothly despite different resolutions. This one-step matrix inversion equation in a discrete form is defined as:

$$\mathbf{m}_{est} = \mathbf{m}_{prior} + (\mathbf{G}^T\mathbf{C}_{d0}^{-1}\mathbf{G} + \mathbf{C}_{m0}^{-1})^{-1}\mathbf{G}^T\mathbf{C}_{d0}^{-1}(\mathbf{d} - \mathbf{G}\mathbf{m}_{prior}) \tag{3.5}$$

where

$$\mathbf{C}_{m0} = (\sigma\frac{L_C}{L_0})^2 \exp(-\frac{\Delta}{L_C})$$
$$\mathbf{C}_{d0} = \sigma_d\mathbf{I}$$

Here L_C is the correlation length that controls the scale of the local smoothing. σ_d is data error applied to the group time data, which we fix to a percentage of 5%, as longer ray paths are more likely to have larger errors than short ones. σ is a damping parameter that controls the model fit (the larger its value, the more the solution is allowed to fit the data and get away from the prior). This parameter must be carefully chosen to avoid over-fitting of the data and unrealistic group velocity values in the solution. Δ is inter-station distances between all measurements of group travel time **d**. The parameterization of the model **m** is chosen to be a regular 2-D grid.

The choice of grid cell size may be as small as ray path density allows for resolution, but large enough so that it is not much smaller than the smallest wavelength considered and unnecessarily computationally expensive.

Equation 3.6 is applied three times, modifying the data covariance matrix as suggested by Liu and Yao [2017] at the second and third iterations. In the first inversion, the data error percentage is assumed to be uniform for all data. In the second and third inversions, outliers are down-weighted following:

$$\{\bar{\sigma}_d^i\}^2 = \{\sigma_d^i\}^2 \exp\left(\frac{\epsilon^i}{2\bar{\sigma}} - 1\right) \tag{3.6}$$

where

$$\epsilon^i = |d_{obs}^i - d_{pred}^i|$$

Here ϵ^i is the data misfit for datum i and $\bar{\sigma}$ is the standard error of all data misfits. This 3-step approach helps further reduce the effect of outliers which is important to consider given the automated picking approach, and also enhance the amplitude of well-constrained model features and reduces variance further.

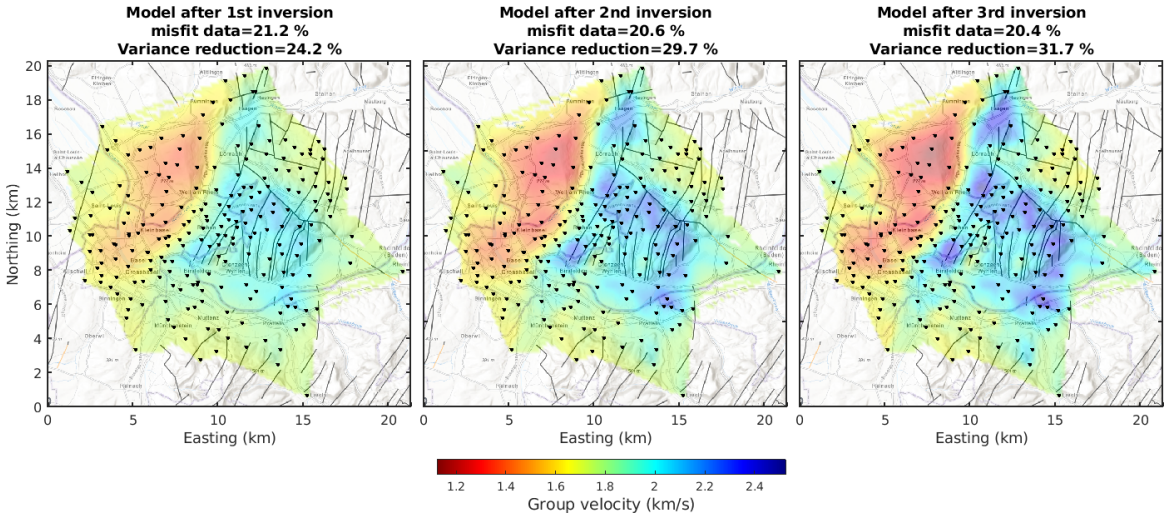
One potential caveat of this inversion approach is the assumption of straight-line propagation and neglected topography effects, which is usually a reasonable assumption in the absence of very strong velocity anomalies or topography. These assumptions could be relaxed by using the Fast Marching Method [Sethian and Popovici, 1999, Rawlinson and Sambridge, 2004] instead for ray tracing. However, we note that a recent study [Karimpour et al., 2022] suggests that the improvement of more accurate ray tracing may in some local-scale cases be negligible. This of course would depend on the amplitude of the local velocity anomalies. If the difference in path length between the straight ray path and the real ray path (accounting for topography and velocity anomalies) produces an error of less than 5% on group travel time, then the assumptions of our methodology should hold well. A comparison of the curved vs straight ray paths effect on tomography may be the subject of future methodological improvement.

3.7 Depth inversion

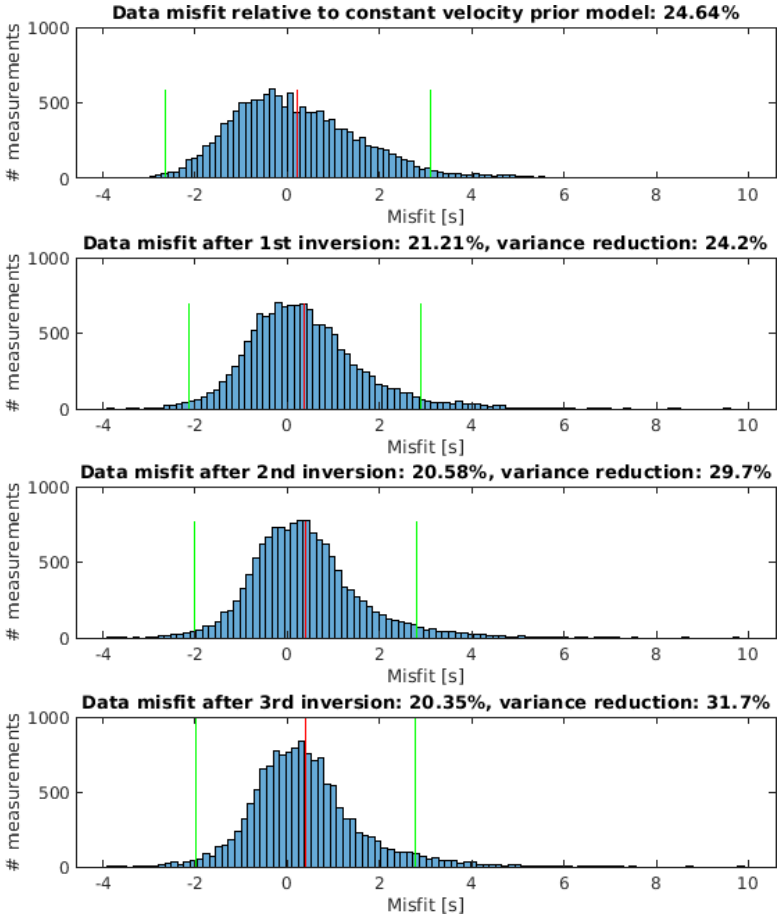
The final step of NANT is to combine the 2-D group velocity maps together to retrieve a local dispersion curve at each point in the horizontal grid and invert these dispersion curves for local 1-D velocity depth profiles. The models shown in the following chapters use automated picks for the fundamental mode dispersion for the Rayleigh waves only. The 1-D profiles at each grid location are then combined and smoothed to obtain a 3-D model. The approach I employed is similar to Planès et al. (2020), who used a non-linear, probabilistic search inversion approach along with the Neighborhood Algorithm of Sambridge (1999) specifically adapted to surface wave dispersion inversion (Wathelet, 2008). The 1-D velocity profiles were parametrized by 14 1-D Voronoi cells, i.e., 14 layers with the depth and velocity allowed to vary within specified prior bounds (from 500 to 4500 m/s for Vs, and 50 to 5000 m for depth). The inversion can be forced to have velocity monotonically increase with depth (no low-velocity layer/domain, “no LVL” model), or low-velocity layers can be allowed (“with LVL” model), with the latter slowing the convergence of the Monte Carlo inversion due to increased solution non-uniqueness. The sequence for the inversion of each 1-D profile is as follows: 30 000 initial models are randomly created within the prior bounds, the 100 best models are then selected based on misfit to observations and regularization constraints, and 5 new models are generated in the neighbourhood of these models via a random walk scheme. These steps are repeated 100 times, after which the final model is constructed from the average of the best 100 models at the final iteration. The final 3D model is constructed by merging all 1D profiles at each grid location and applying horizontal and lateral smoothing, with a 3-cell box kernel.

3.8 Rayleigh wave ellipticity (H/V ratio)

We conclude the methodology chapter by describing recent efforts in retrieving Rayleigh wave ellipticity from ambient noise cross-correlations. Rayleigh wave ellipticity is equivalent to the H/V ratio, a well-known seismological parameter used to quantify ground amplification effects. As the sensitivity kernels in Figure 3.8 show, ellipticity is a measurement sensitive to shallower velocity structures, which is complementary to dispersion measurements where picking below 1 s is challenging. By jointly inverting ellipticity with dispersion measurements, the shallower part of the velocity model can be better constrained and in return, improve greatly the overall subsurface model retrieved and its uncertainty. Several studies have demonstrated this for large-scale imaging (regional to continental scale) in the past decade. However, it is only recently that shallow-scale applications have emerged, such as the studies of Wells et al. [2022] and Zeng et al. [2022]. Here we follow Lin et al. [2014] and Berg et al. [2021] to calculate Rayleigh ellipticity from the stacked cross-correlations. The ellipticity is a measurement that applies spatially to one individual station location at a specific period. For a given station, all the cross-correlations between that station and the others are used to estimate the ellipticity. The stacked



(a) Solution after each of the three inversion steps



(b) Distribution of misfits at each iteration

Figure 3.15: Example of group velocity map inversion at a period of 1.5 s for the Riehen dataset, showing the effect of the three inversion steps on the solution. a) Group velocity maps share the same colour map. Notice the increase in anomaly amplitude at the third inversion, with smaller scale details revealed. b) Misfit distribution relative to the prior model and after the three inversions. The red and green vertical lines show the mean and 3 standard deviation bounds for the misfit distribution.

cross-correlations for ZZ, ZR, RZ and RR cross-components are narrow-band filtered with a Gaussian kernel. We then take the negative time derivative of the cross-correlation as Green's function which allows the ZZ and ZR cross-components to be interpreted as the wavefield produced by a vertical point force on the vertical direction at the first station and recorded on the vertical and radial components of the second station (Table 3.1). The ellipticity (or H/V ratio) is then taken by calculating the ratio of the maximum amplitude of the envelope of the radial component over the maximum amplitude of the envelope of the vertical component in the predicted time window for a realistic group velocity range for Rayleigh waves. The H/V ratio is calculated for the negative and positive time lags separately and for the cross-components corresponding to the vertical point force excitation (ZR/ZZ) and radial point force excitation (RR/RZ), which gives a total of 4 measurements of the H/V ratio for each station pair. Several quality control criteria are then applied. We retain only cross-correlations with an SNR larger than 5 on all 4 cross-components and inter-station distances larger than 3 wavelengths. The final H/V ratio is the mean of all measurements for a given station, and the spatial distribution of station-wise standard deviations gives its uncertainty. The logarithm of H/V ratios at all station locations are interpolated on a grid with inverse-distance weighting and linear radial basis functions.

4. Results: Aargau subsurface model

We now present the result of the different inversions applied to the measured dispersion curves for the Aargau dataset. By subsurface model, we refer to: a set of 2D group velocity maps at different frequencies, a 3D model of shear-wave velocity and a set of 2D maps of ellipticity (H/V ratio) at different frequencies.

4.1 Group velocity maps

4.1.1 Rayleigh waves

As illustrated earlier in Figure 3.8, group velocity at a given period is affected by average subsurface shear-wave velocities sampled by its sensitivity kernel. For a period T, peak sensitivity is typically roughly around T/3 to T/2 km in depth, so this help interprets roughly group velocity maps as shear-wave velocity averages across a depth range. Figure 4.1 shows Rayleigh group velocity maps at periods of 0.5 to 2 seconds, corresponding roughly to shallower structure in the top 1.5 km of the crust. Comparing with the superficial geology map in Figure 2.2, the slow anomalies are quite consistent with where the faster Mesozoic bedrock units of the Tabular Jura and Folded Jura are found and the slower rocks and sediments of the Molasse Basin and Quaternary deposits. At 1.5 and 2 s, the signature of the Constance-Frick Trough becomes visible, with two slow velocity zones separated by a high-velocity gap in the middle (15 km Easting) that also happens to coincide with the peak heat flow contours.

The deeper structure is sampled by the higher periods. In Figure 4.1, group velocity maps above 3 s show the signature of the trough clearly, but the trough appears persistently split in two by a narrow high velocity near the Aare River. At 4.8 s, this high-velocity body has a shape that resembles the heat flow contour of $140\,\mathrm{mW/m^2}$). The Riniken well is just outside the western edge of this anomaly and the low velocities just below this well remain consistent with the Permo-Carboniferous formations encountered down to $1800\,\mathrm{m}$ there. The high velocities expected for the crystalline basement under the Folded Jura follow remarkably well the trace of the Jura Main Thrust. The high velocities to the north, under the Boettstein and Leuggern wells, are also consistent with the crystalline basement that was encountered at very shallow depths there.

One of the most interesting observations from the group velocity maps is the high-velocity splitting of the low velocities in the axis of the trough. Madritsch et al. [2018] also found from reinterpreted 2D reflection lines that the depth of the trough varies along its axis, with a western and an eastern segment separated by a basement high. We note that this basement high on their maps is however more to the east than we observed on our maps

4.1.2 Love waves

Looking at group velocity maps for Love waves in Figure 4.2 (measured from TT cross-correlations as opposed to ZZ cross-correlations), we must keep in mind the difference in sensitivity kernels of Love waves vs Rayleigh waves. In the appendix, in Figures C.3 and C.4, sensitivity kernels calculated from layered models derives from the Riniken and Boettstein well geological interval Vp log are shown. A constant Vp/Vs ratio of 1.73 is assumed to derive a Vs reference model to calculate these kernels, which is an important assumption, but the kernels facilitate the interpretation of the Love group velocity maps. These kernels show that for a given period, the sensitivity is more continuous in-depth, and averages the Vs velocities from the surface down to a depth that increases with period. As seen in the appendix C, the depths of sensitivity change with respect to the Vs model itself (shallow vs deep crystalline basement), but we can still make some first-order interpretations from the Love maps.

What we see on the Love wave group velocity maps confirms the general interpretation from Rayleigh wave maps. From 1 to 3.5 s, high-velocity anomalies north of the Mandach Thrust confirm a shallow crystalline basement, which is supported by well logs at Böttstein and Leuggern that encounter the crystalline basement at 317 and 229 m depth respectively. Low-velocity anomalies to the south of the Jura Main Thrust are consistent with the Molasse basin cover. Intermediate velocities above the through are consistent with the Mesozoic cover.

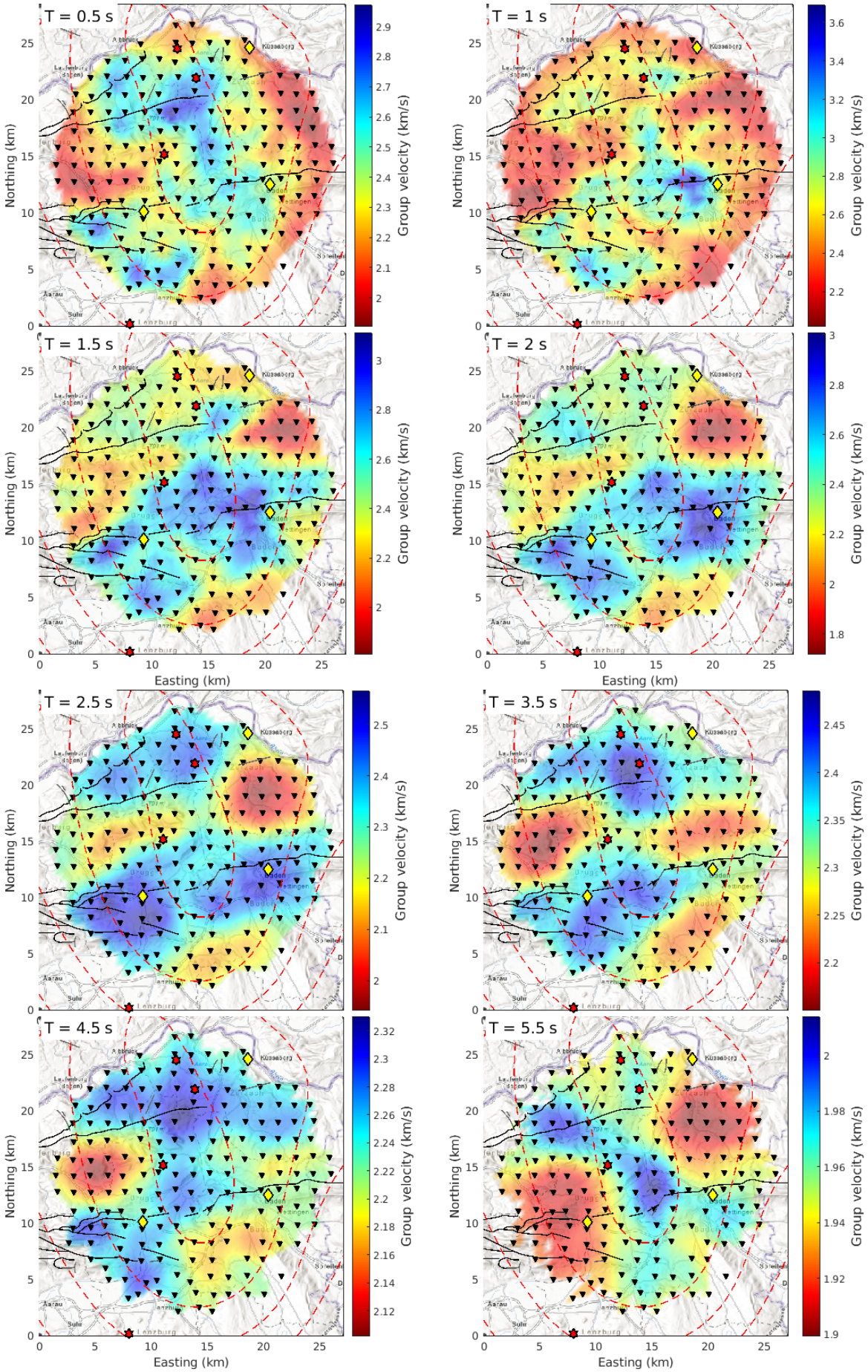


Figure 4.1: Rayleigh wave fundamental mode group velocity maps for the Aargau dataset at periods of 0.5 to 5.5 seconds. Yellow diamonds show hot spring sources and red hexagrams show deep wells. Red dashed lines show heat flow contours. The black solid lines are surface fault traces from the Swisstopo geodatabase.

The low-velocity anomalies of the trough emerge in the maps at 2.5 and 3.5 s. At 4.5 to 6 s, where we are sampling near the bottom of the trough and below, an interesting NW-SE trend showing low velocity appears, which is most obvious at 6 s. Note that the absolute velocities vary on a small scale, so these anomalies are subtle. But the NW to SE apparent trend resembles the Rayleigh map at 5.5 s, and this trend agrees remarkably well with the continuation of the Eggberg and Vorwald Faults (see Figure 2.4). This seems to support the observation of a basement high, possibly enabled by a weakness in the crust caused by these two major Faults that more or less parallel each other.

4.2 3D shear wave velocity model

We now focus on the 3D shear wave velocity (Vs) model which was constructed from the group velocity maps presented previously at periods between 0.6 and 5.0 s and inverted for depth. We followed the methodology described earlier and developed two models: one with low-velocity domains allowed ("with LVL"), and one without ("no LVL"). Figure 4.3 shows a map slice at 2.5 km through the 3D Vs model, which is plotted as percentage anomalies from the mean Vs to simplify interpretation. It shows the trace of the 4 depth cross-sections in Figure 4.4. The distance along the depth cross-sections goes from south to north (V1-V1', V2-V2', V3-V3') and west to east (H1-H1').

For the "no LVL" model in Figure 4.5, we can easily identify discontinuities by examining sharp lateral gradients in velocity. Looking at the surface expression of the faults crossing the profile trace, a clear gradient is associated to the Jura Main Thrust (JMT) and the Mandach Thrust (MT) bounding the basement trough. The velocity isocontours near the Mandach Thrust dip more steeply from the surface than for the JMT, which is consistent with seismic reflection line observations [Madritsch et al., 2018]. Associating the low velocities to the Permo-Carboniferous sediment, we would estimate the bottom depth of the trough on the cross-section V1-V1' to be about 4 km, et slightly shallower (3 km) on V2-V2', which is a trend that is again consistent with seismic reflection lines. Madritsch et al. [2018] choose to analyze the seismic reflection lines as prestack time migrations because of the poorly constrained P-wave velocity model available, especially at depth, that must be used to convert two-way traveltimes to depth. They also highlight the very high degree of uncertainty in resolving the bottom depth of the trough, especially away from deep wells and towards its southern boundary, where the high scattering caused by the Folded Jura structures obscure clear reflection arrivals from below. This highlights how complementary additional models like ours are to reduce interpretation uncertainty.

On cross-section V2-V2', there are also apparent faults or fractures reaching the basement south of the JMT, as the velocity anomalies should have "finger-like" shapes, that can indicate fluid pathways into the basement. In V2-V2' and V3-V3', around a distance of 15 km along the Northing, we start to see a high-velocity anomaly starting from the edge of our model at 5 km depth to 2 km depth on V3-V3'. This bulging high-velocity anomaly peaks under the low points in the trough structure. On V3-V3', the shallower point of the basement bulge has a slightly smaller anomaly amplitude, which potentially indicates increased hydration. The low velocities above this basement bulge are associated to the sediment in the trough but the amplitude anomaly is also particularly pronounced which we interpreted as the contribution of increased underground fluids as well. Interestingly, the Zurzach thermal springs are also located near this area, which helps support this interpretation. Finally, the horizontal cross-sections H1-H1' shows clearly a saddle-like high-velocity structure that split the trough into two segments and that could be clearly seen on the group velocity maps as well. We highlight that this structure that we interpret as a basement high coincides almost exactly with the peak flow anomaly contour, elongated in the N-S direction (Figure 4.3). Due to radioactive decay in granitic rocks, a shallower granitic basement would explain the increased heat flow. We note that Madritsch et al. [2018] mapped the basement high more to the east (near the eastern edge of our study area) than we see in our observations. They interpreted the segmentation of the trough as caused by preexisting Late Variscan strike-slip faults, more specifically the Vorwald Fault continuation southeastward. We note that the Eggberg Fault, located just south and parallel to the Vorwald Fault, is also suspected by the authors to continue southeastward and this fault trace would cross the trough where we observe our crystalline basement high. We interpret that the preexisting Eggberg and Vorwald faults created increased weaknesses in the crust where these faults meet the rift that formed the Constance-Frick Trough and this may have allowed the bulging of the crystalline basement and the increased surface heat flow.

The 3D model with LVLs in Figure 4.5 fits significantly better the dispersion data than the model without LVLs. Some features of the dispersion data cannot be reproduced with a model with monotonically increasing velocity with depth. Anomalies due to aquifers at depth are likely to manifest as low-velocity domains, so this model is particularly useful to interpret the presence of fluids that is overprinting the contribution of rock composition. In Figure 4.5, we kept the same annotations for tectonic discontinuities from Figure 4.4 since they are easier to identify on the «no LVL» model. Several features stand out from these cross-sections. First, there are horizontal LVLs near 500-1000 m depth that are consistently observed on the shoulders of the trough. Referring back to the Nagra conceptual sketch in Figure 2.5, this would be consistent with thermal waters accumulating at the base of the Mesozoic cover. Another deeper LVL around 3-4 km depth is consistently observed north of the Mandach Fault. Inside the trough, the low velocities are also pronounced, which may indicate contributions

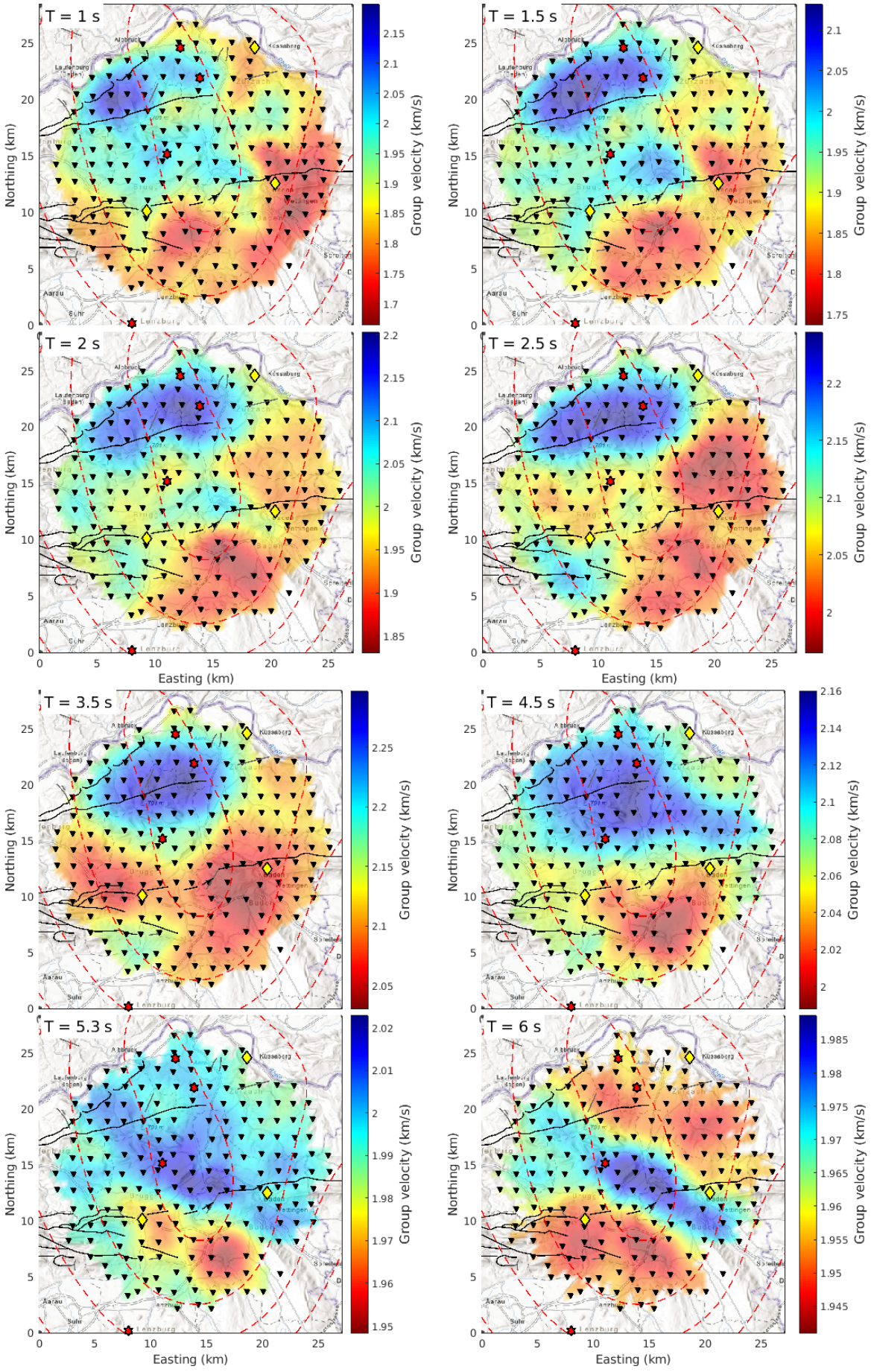


Figure 4.2: Love wave fundamental mode group velocity maps for the Aargau dataset at periods of 0.5 to 6 seconds. Yellow diamonds show hot spring sources and red hexagrams show deep wells. Red dashed lines show heat flow contours. The black solid lines are surface fault traces from the Swisstopo geodatabase.

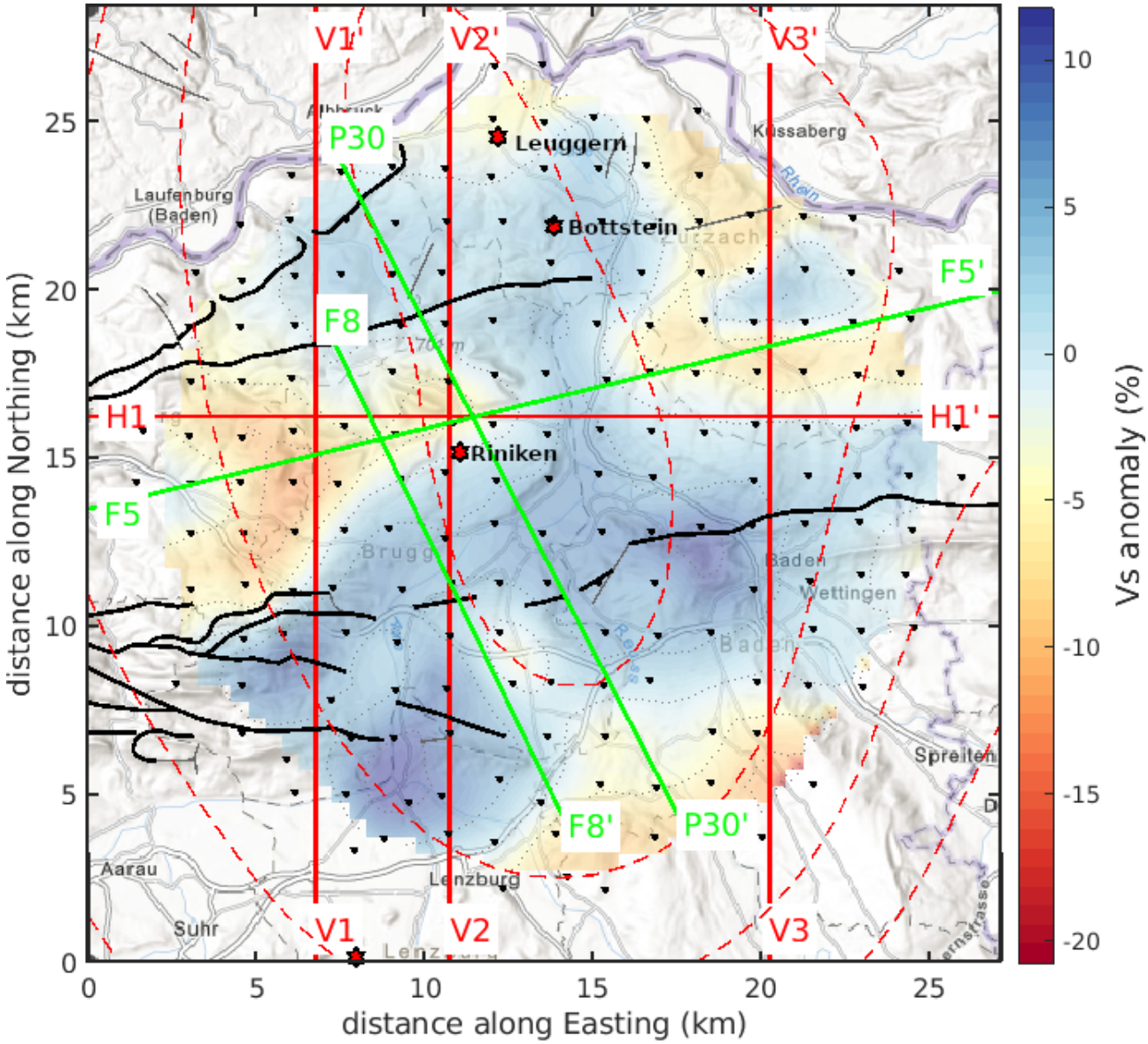


Figure 4.3: Slice of the 3-D Vs model of Aargau at 2.5 km depth with the traces of the depth cross-sections. Green lines are cross-sections attempting to match 2D seismic reflection lines.

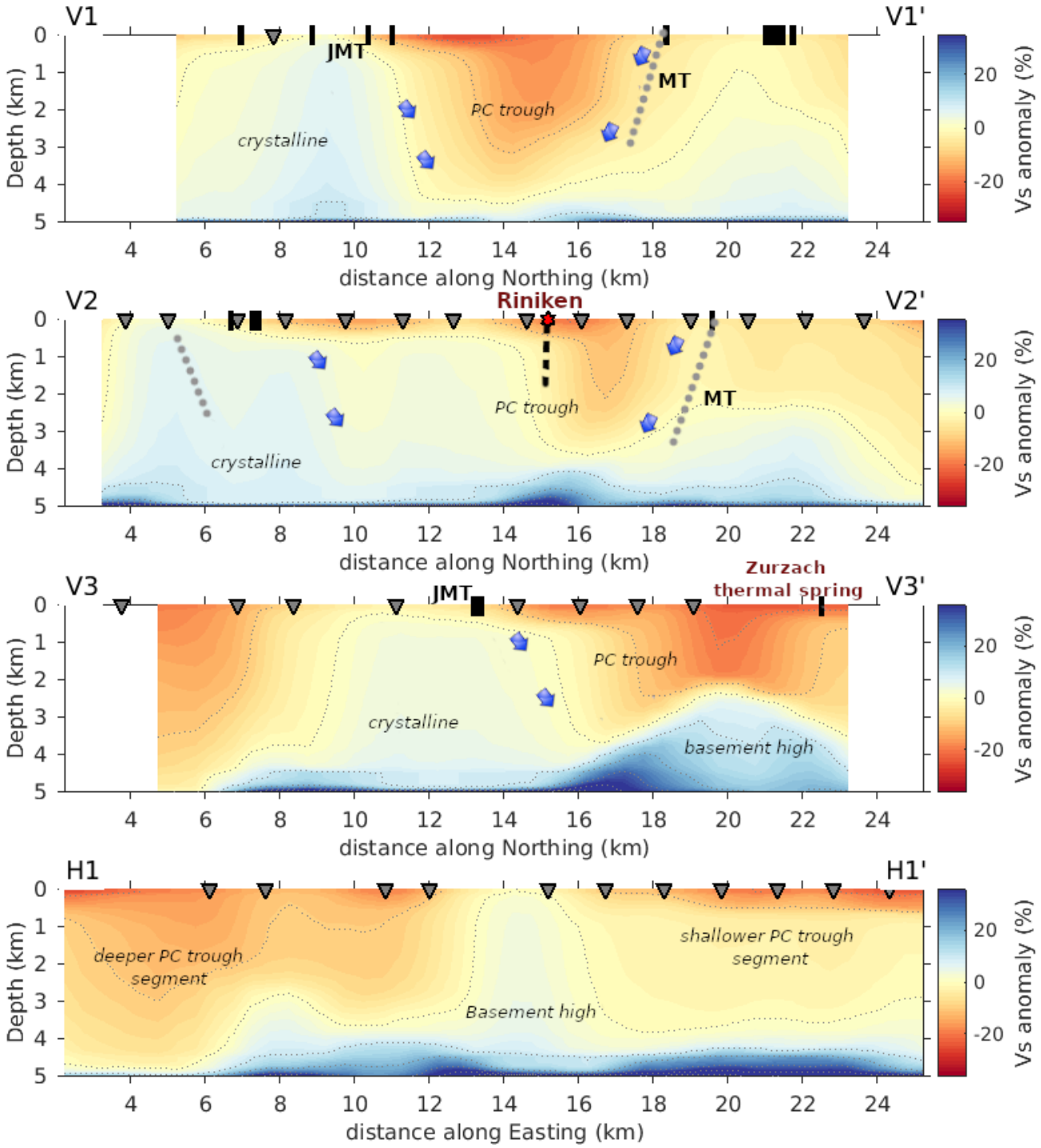


Figure 4.4: Depth slices through the 3-D «no LVL» Vs model along latitude according to the profiles shown in Figure 4.3. Grey dotted lines indicate the speculated discontinuities such as fault zones or structural contrasts. Blue arrows represent possible fluid pathways. Inverted gray triangles and black tick marks at the surface show stations and fault lines respectively, located near the cross-section trace

from not only the low-velocity sediments but also hydrocarbon fluids, as suggested in Figure 2.5. The black arrows also indicate deep fluid anomalies near the edge of our model, at 4.5-5 km depth, that coincide with the depth continuation of the JMT, MT and other discontinuities. The JMT and MT are major, well-developed fault zones that would provide obvious pathways for fluids to reach these depths.

4.3 Comparison to seismic reflection

We will limit the comparison to a few 2D reflection profiles found Madritsch et al. [2018]. There exists a 3D reflection survey overlapping with our study area (Figure 2.4), but we do not have easy access to these data at the time of writing. Figure 4.7 and 4.6 show the two depth cross-sections corresponding to lines F5-F5' and F8-F8' in Figure 4.3, respectively. We show both the corresponding cross-section in the models with LVLs and no LVLs. The model with LVLs fits significantly better the dispersion data than the model without LVLs, so the former should be given more weight in the comparison.

The seismic reflection profiles show the Common Midpoint on the x-axis and the Two-Way-Traveltime in milliseconds on the y-axis instead of distance and depth in kilometres. The seismic reflection images are also vertically exaggerated, so dip and orientation of linear features are not expected to match closely with the NANT images below. As explained in Madritsch et al. [2018], migration of seismic reflection data to depth is a challenging task and some important assumptions must be made, so this step of processing is not always completed or easily interpreted. For this reason, care must be taken when comparing the two different types of images. Because seismic reflection uses high-frequency compressional (P) waves to image impedance contrasts corresponding to stratigraphic layers, faults can be detected by looking at horizons and their discontinuities. The NANT images, in comparison, use surface waves with low frequencies to image shear (S) wave velocity, hence the two very different kinds of images. We should keep in mind these two methods provide complimentary information as they image different subsurface properties.

In Figure 4.6, the profile runs across the trough, near the Riniken deep well. A steeply dipping low-velocity anomaly is consistent with the steeply dipping Mandach Thrust evidenced in seismic reflection. In the NANT models, S-wave velocity is especially low along the fault outline, suggesting it may be a particularly efficient fluid pathway. To the south, the boundary of the Jura Main Thrust is less obvious and less steep, as in the reflection image. On the seismic reflection image, the structures of the crystalline basement under the Jura Main Thrust and south of it are poorly resolved due to high scattering from shallow structures obscuring deeper reflections. In the NANT images, low-velocity anomalies with an amplitude similar to the known PCT persist toward the south, which suggests Permo-Carboniferous sediments are also found there. We also note a possible deep fluid reservoir near 5 km depth is suggested at the edge of our model, below the JMT, but velocity values at the edge of the model should be interpreted with caution. Another feature that stands out in the model with LVLs is the pronounced high-velocity anomaly with a thickness consistent with the Mesozoic cover as imaged in seismic reflection.

Figure 4.7 shows a profile along the middle of the Constance-Frick Trough. In both NANT and seismic reflection images, the trough bottom depth appears deeper west of the Aare River compared to the east. Interestingly, the clarity of the Mesozoic cover bottom reflection becomes unclear below the Aare River, and several faults are suspected on the basis of the reflection data, albeit with poor confidence. In the NANT image, a very clear lateral contrast arises in the same location, which suggests there is a real feature in this area, suspected to be the signature of Vorwald or Eggberg Faults. This location, near the Aare River axis, is also where we see the highest heat flow anomaly, which suggests a causal link. A recent local-scale NANT study found known fault zones appearing on tomographic images as high-velocity anomalies, that they interpreted as cooled magma intrusions that welded shut these faults, making them less active [Gu et al., 2022]. It is conceivable that the near vertical high-velocity discontinuity we see below the Aare River may be caused by a fault zone as well.

4.4 H/V ratios

Figure 4.8 shows the logarithm of H/V ratios measured at each station in the Aargau network at different periods. As shown in Figure 3.8, Rayleigh ellipticity is sensitive to very shallow velocities and progressively increased depth with an increased period, so thick Quaternary deposits should have a clear shallow velocity structure [Okamoto and Tsuno, 2018]. The Swiss sediment thickness model available from Swisstopo, is shown as black contours in the maps. The thick sediment basin (> 150 m) near the southern end of the network correlates nicely with high H/V ratios with values exceeding 2, as expected from ground amplification effects of unconsolidated sediment. This pronounced basin of sediments south along the Aare River is known as the Birrfeld basin. These structures are subglacial overdeepenings, closed troughs eroded below fluvial base level [Gegg et al., 2021]. The low H/V ratio measurements on the other hand concentrate near latitude 47.45-47.5 N, along the Jura Main Thrust that bounds the southern end of the Constance-Frick Trough. Okamoto et al. [2021] found that fluids can explain drops in H/V spectral ratio in geothermal areas. We may thus interpret these low values

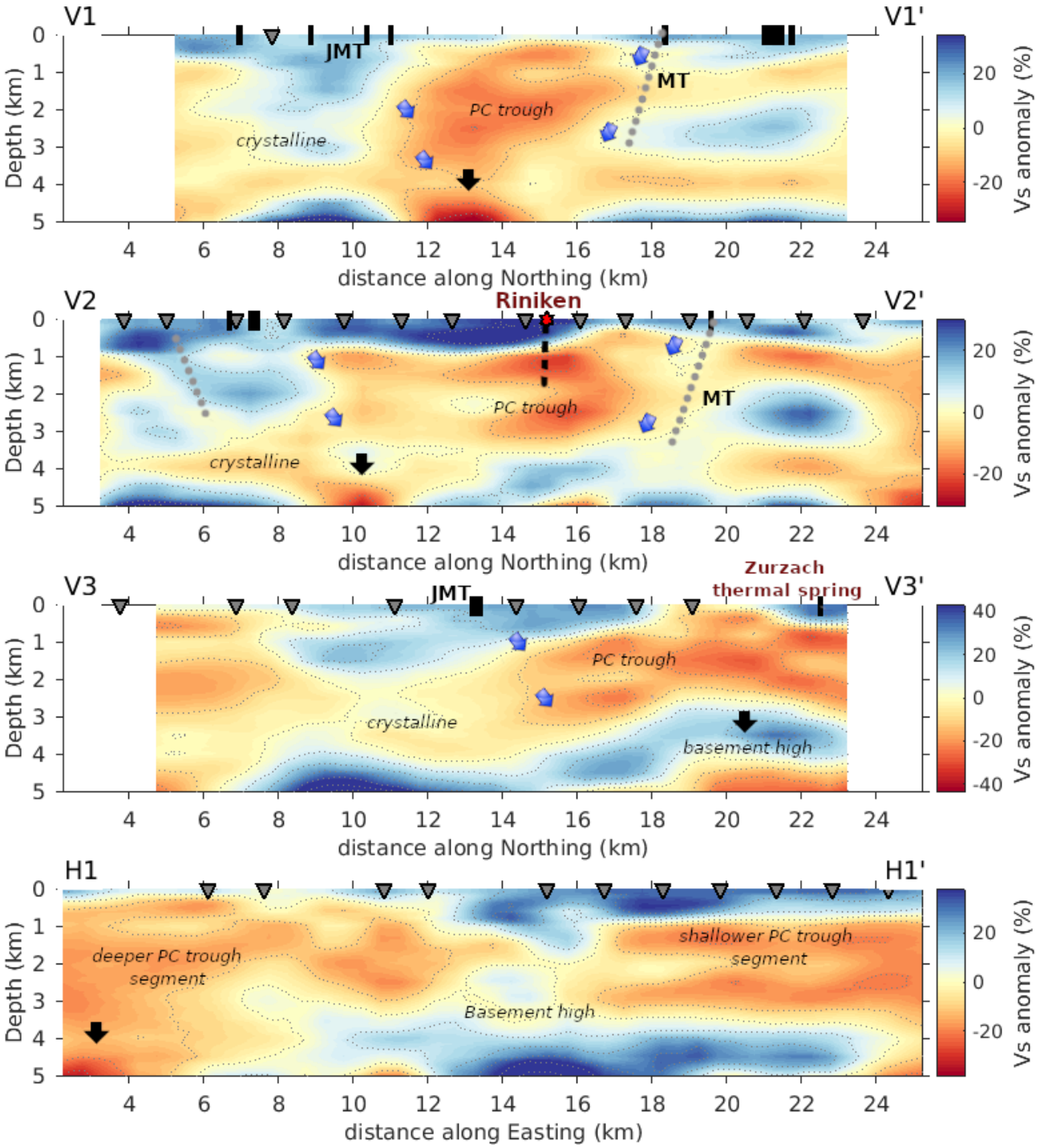


Figure 4.5: Depth slices through the 3-D «with LVL» Vs model along latitude according to the profiles shown in Figure 4.3. The interpreted symbols (gray lines and blue arrows) are the same as in Figure 4.4, from which they are identified. Black arrows indicate very deep low-velocity anomalies that suggest deep underground water accumulation zones.

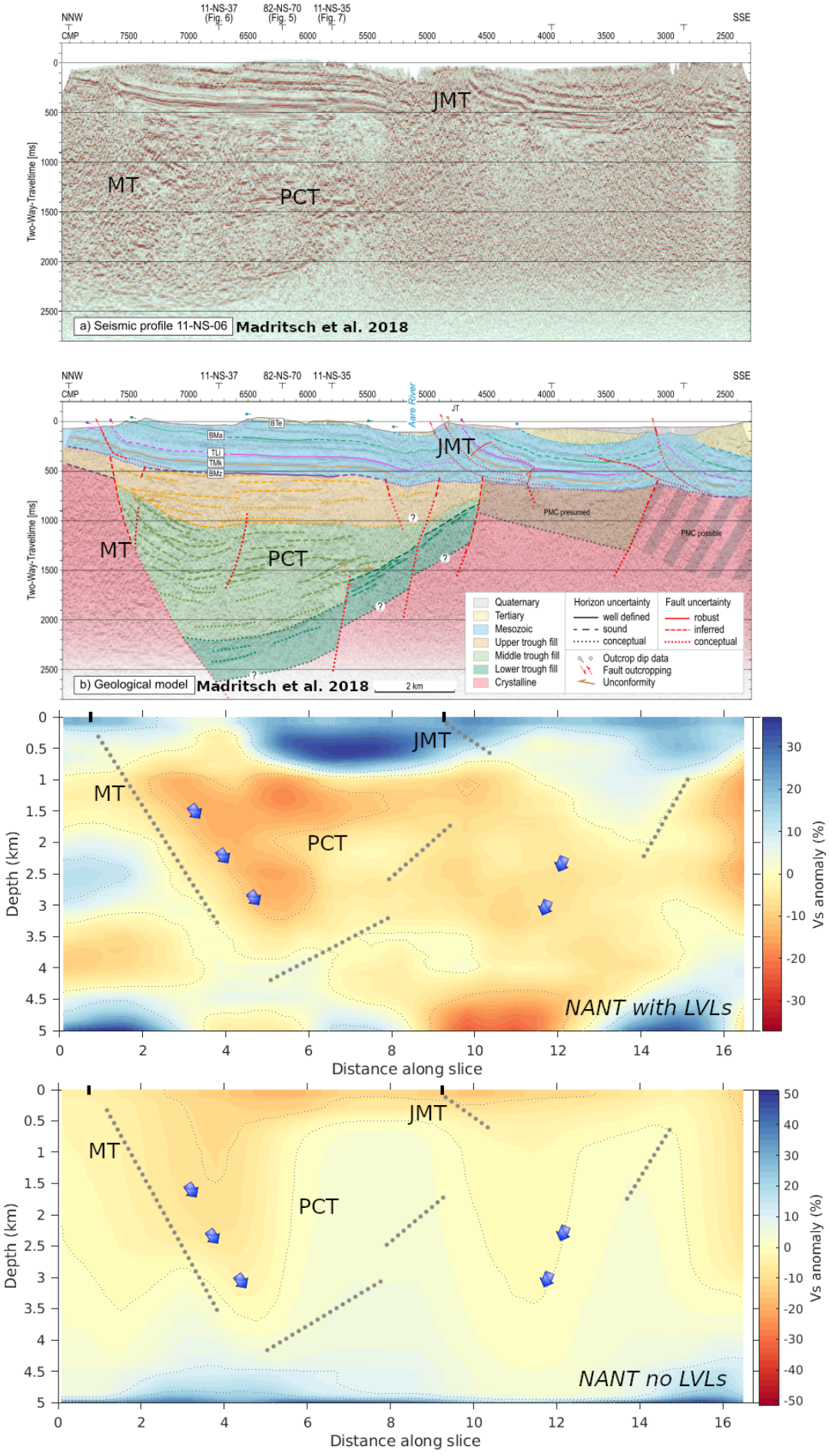


Figure 4.6: Comparison of the 2D seismic reflection images modified from Figure 8 in Madritsch et al. [2018] with the 3D Vs models from NANT (with and without LVLs allowed in the depth inversion) along line F8-F8' in Figure 4.3.

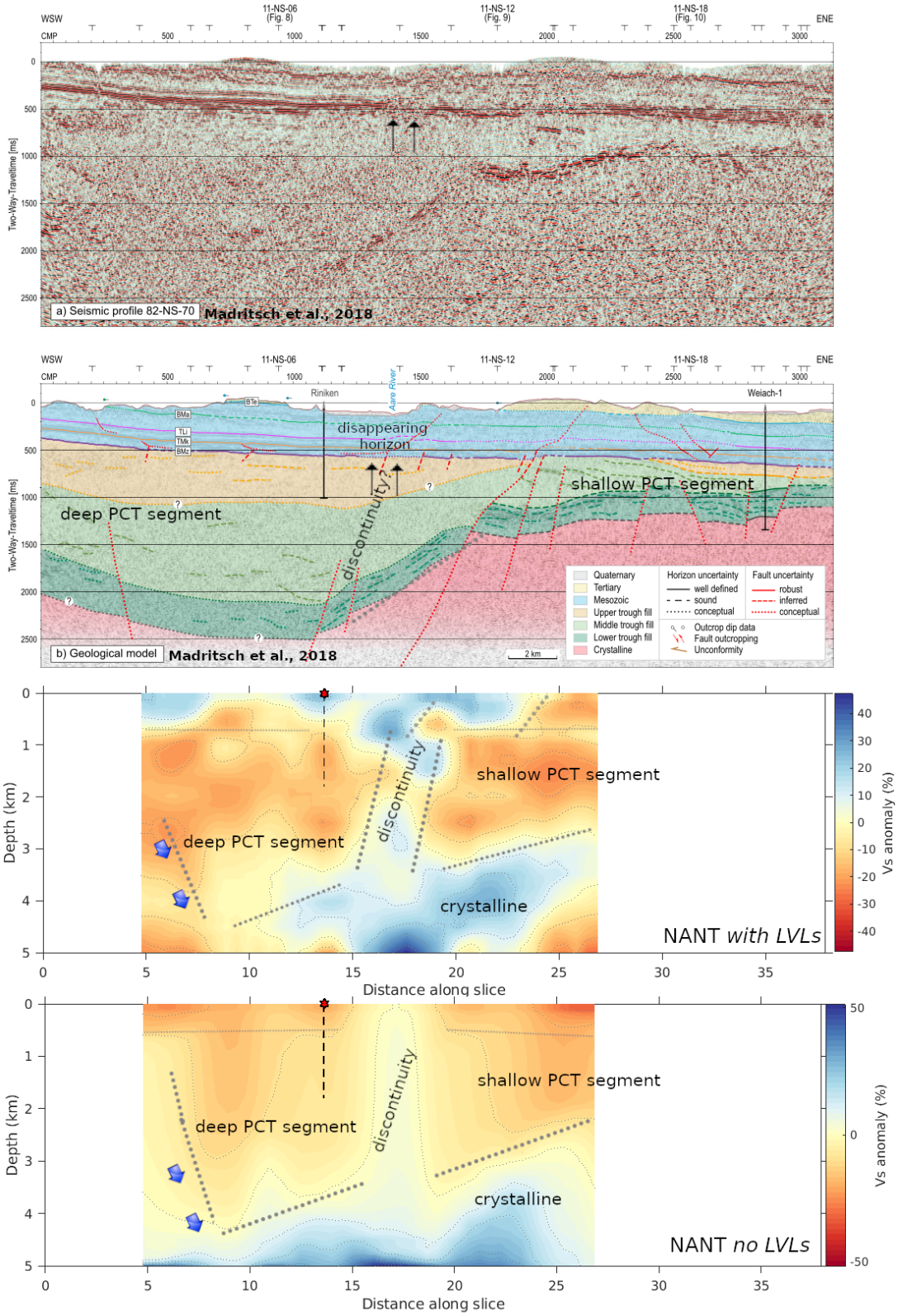


Figure 4.7: Comparison of the 2D seismic reflection images modified from Figure 5 in Madritsch et al. [2018] with the 3D Vs models from NANT (with and without LVLs allowed in the depth inversion) along line F5-F5' in Figure 4.3.

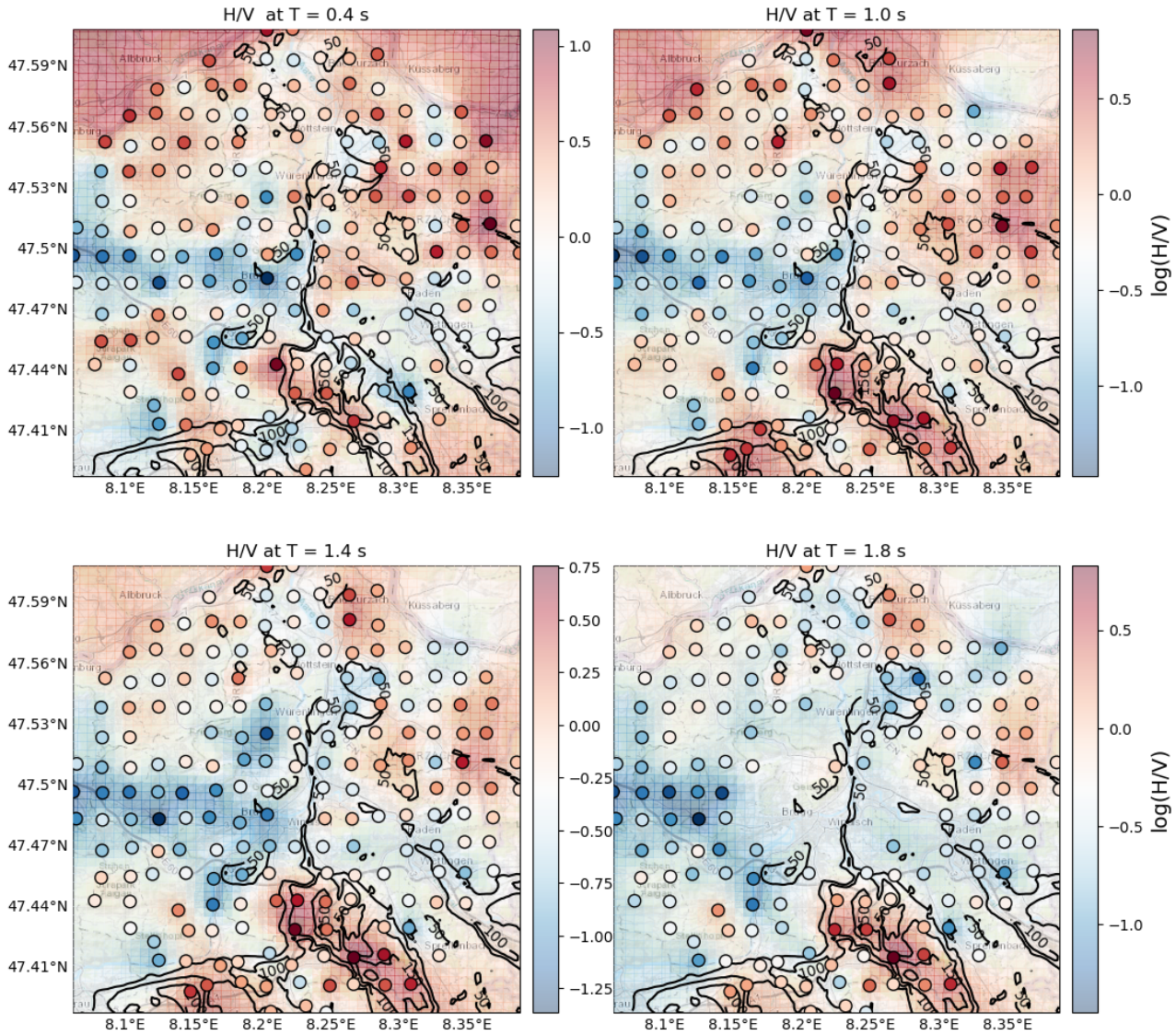


Figure 4.8: Rayleigh wave ellipticity (H/V ratio) from ambient noise cross-correlations for Aargau. Single station measurements of log(H/V) at different periods are interpolated on a grid with a radial basis function scheme. Contours in black show Switzerland's sediment thickness model, obtained from Swisstopo, with contours shown for every 50 m increase in thickness

as shallow fluids, which is consistent with the numerous faults found in the Mesozoic bedrock of the Folded Jura based on Nagra 2D reflection lines and the karstic groundwater character of these formations that facilitate penetration of fluids from the surface. The coherence of our measurements with the sediment model suggests our methodology and data are adequate for H/V analysis and this dataset can be combined with the 3D Vs model from NANT to get a robust estimate of structures from surface to depth.

5. Results: Riehen area subsurface model

We now present the inversion results for the Riehen dataset. As for Aargau, the subsurface model package comprises a series of group velocity maps (from 0.5 to 4.5 seconds), a 3D Vs model based on Rayleigh wave dispersion and H/V ratios calculated from Rayleigh wave ellipticity.

5.1 Group velocity maps

5.1.1 Rayleigh waves

Figure 5.1 shows group velocity relevant to the shallow subsurface (<1.5 km depth). The fault lines shown on the maps are from the Swisstopo database, but not all these faults are expected to reach the crystalline basement. For example, based on multiple studies, the dense network of short faults in the Dinkelberg block may only cut through the outcropping Mesozoic units, unroofing the Triassic cover, and these faults are not thought to affect the crystalline basement [Delacou et al., 2009]. We however plot all these fault lines to help provide a spatial reference for the velocity anomalies. To highlight which fault lines are known deep faults, Figure 2.8 shows the faults selected by company Serianex for seismic risk modelling ahead of the Basel Deep Heat Mining project [Delacou et al., 2009]. These faults were selected for their potential to host M>5 events, due to their suspected deep extent into the crust. The Rhine Valley Flexure crosses our study area in the middle and is modelled to reach 25 km depth. The cross-section shows the Basel Deep Heat Mining well location. As this figure shows, Basel-Stadt and the western half of Riehen are part of a block in the Graben defined by the Rhine Valley Flexure to the east and the Alschwill fault to the west. The Rhine Valley Flexure is not believed to be continuous, but instead to be comprised of several fault patches, resolved with varying confidence by previous geophysical observations. The lateral extent of several faults including the Sierentz fault, is not well constrained by previous studies. Rheinfelden, Weil-am-Rhein and Aspenrein are important NW trending inherited faults that cut through the Mesozoic cover of the Tabular Jura and likely reach the crystalline basement below.

Looking at the group velocity map at 1.5 s, the contrast between the low velocities of the Upper Rhine Graben and the high velocities of the Mesozoic Jura becomes clear, with a very well-defined boundary. At 1.5 and 2 s, a group velocity contrast also appears consistent with the Alschwill fault. At 0.5 and 1 s, there is a clear low-velocity anomaly corresponding to the area of Riehen, which may indicate shallow fluids. This would be supported by the successful hydrothermal operations so far from the Geo2Riehen wells (Peter Meier of GES, personal communication).

For the group velocity maps at 2.5 to 4 s (Figure 5.1), the Upper Rhine Graben structure is the clearest feature. There is however an interesting low-velocity anomaly south of the Dinkelberg massif, with a clear NW trending north boundary. This clear trend may agree with the southeast extension of the Sierentz Fault. It is however remarkable that at 4 s, the Riehen-1 and Riehen-2 wells, which are close to the current successful wells of Geo2Riehen, are located at the edge of a pronounced low-velocity anomaly.

5.1.2 Love waves

The Love wave group velocity maps shown in Figure 5.2 can be interpreted in terms of depth by using the sensitivity kernels calculated for the 1D Vs model of Michel et al. [2017] and shown in the appendix in Figure C.1. As we mentioned in the Methodologies section, the coherent energy on the ZT, TZ, RT, TR components (Figure 3.6) suggested some Rayleigh wave energy might be leaking on the TT components. However, the dispersion curve pick histograms for the TT cross-component showed a trend that seems consistent with the predicted Love wave dispersion (Figure 3.11). So we decide to cautiously interpret the Love wave maps as well.

At 1 s, the image reflects the average velocity in the first 1 km of the crust and reflects clearly the contrast between the faster Mesozoic rocks in the Dinkelberg block and the slower sedimentary sequences filling the

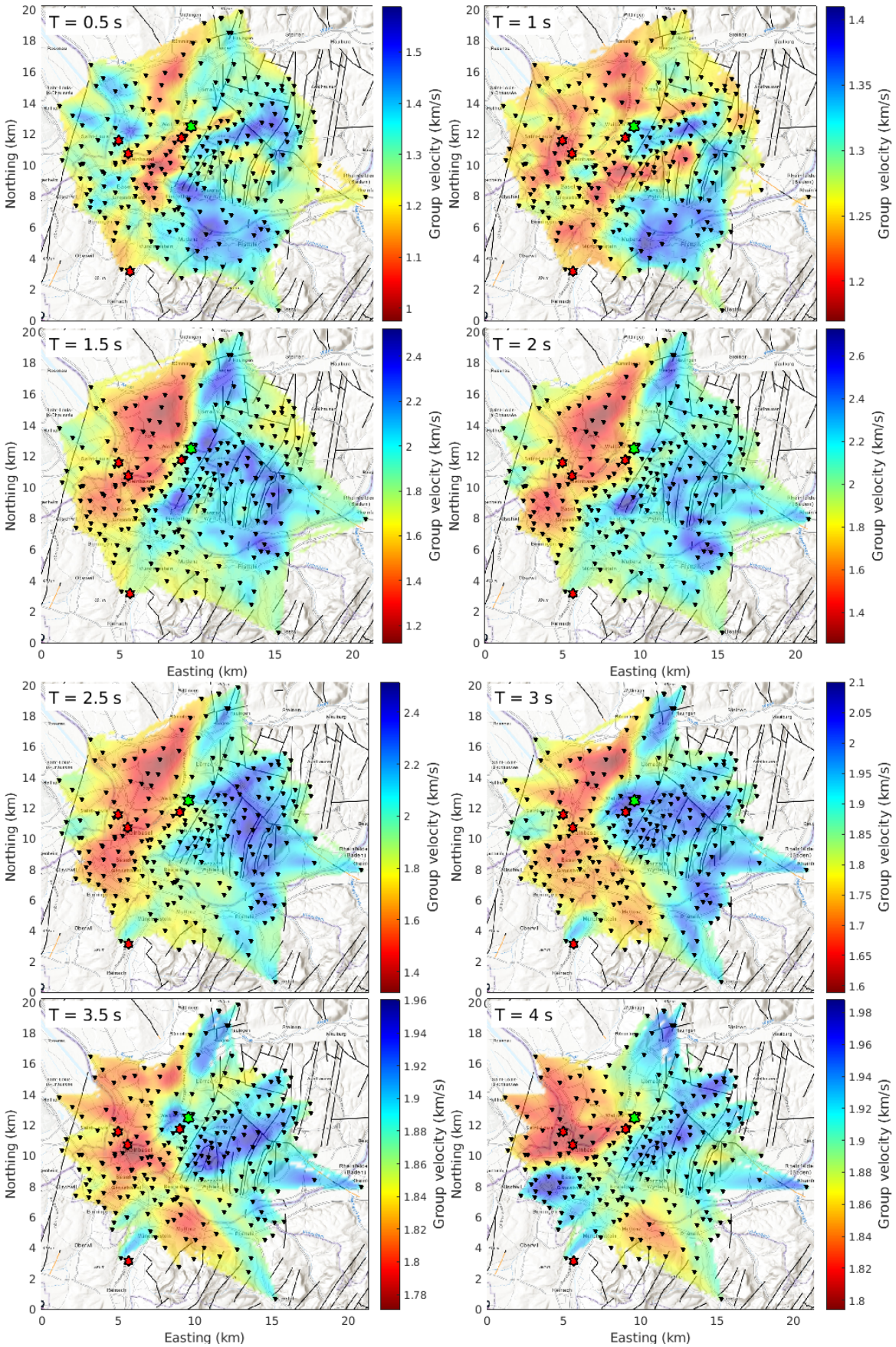


Figure 5.1: Rayleigh wave fundamental mode group velocity maps for the Riehen dataset at periods of 0.5 to 4.5 seconds. Red hexagrams show deep wells with the green hexagram showing well Riehen-2 for reference. The black solid lines are surface fault traces from the Swisstopo geodatabase, which is shown for reference, but note that the faults in the Dinkelberg block are understood to be shallow.

Rhine Graben. The maps at 2, 3 and 4 s show an interesting trend, where the Riehen-1 and Riehen-2 wells sit clearly at the edge of very pronounced low-velocity anomalies. At 2 s, there may be a contribution to the velocity anomaly from the Quaternary sediments along the Rhine River (see Figure 2.6). The subtle high-velocity anomaly at 4 s located south of the Basel-1 and Otterbach-2 wells seems consistent with the Rayleigh maps at 3.5 and 4 s, indicating a possible crystalline basement high below the Rhine Graben.

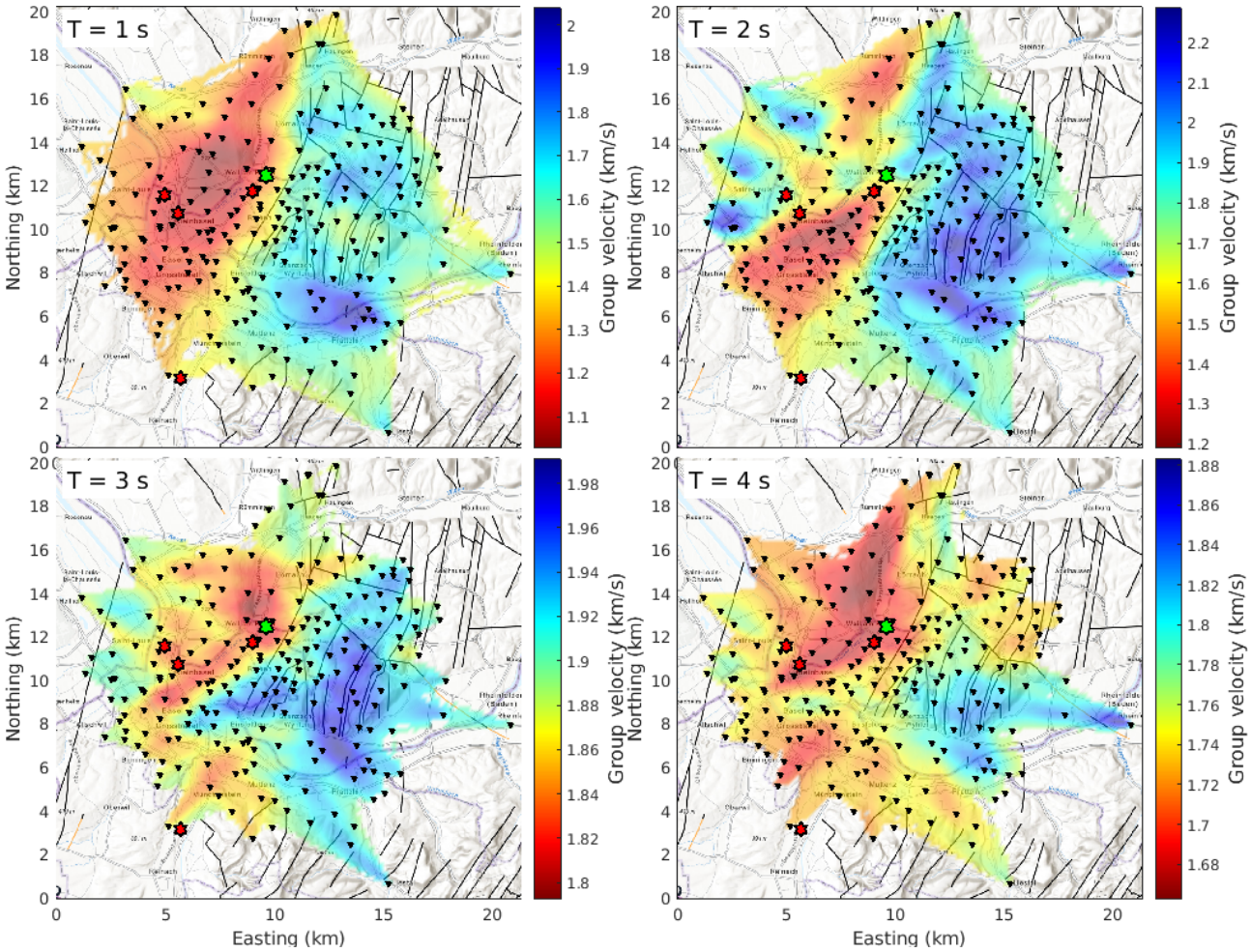


Figure 5.2: Love wave fundamental mode group velocity maps for the Riehen dataset at periods of 1 to 4 seconds. Red hexagrams show deep wells with the green hexagram showing well Riehen-2 for reference. The black solid lines are surface fault traces from the Swisstopo geodatabase, which are shown for reference, but note that the faults in the Dinkelberg block are understood to be shallow.

5.2 3D shear wave velocity model

The 3D shear-wave velocity model shown below is for an inversion with no LVLs. The model with LVLs is still in development, but we report that the no LVLs model fits the dispersion data comparatively significantly better than in the case of Aargau. The depth inversion was done with a half-space layer with a maximum depth of 5 km for the top of the layer, as in the case of Aargau. However the Riehen network aperture was smaller, and the group velocity maps up to 4.5 s are used, in comparison to 5.5 s for Aargau. This means the last 1 km in depth of the model may not be well-constrained. The saturated high-velocity horizon between 4-5 km is then potentially an artifact of the band-limited dispersion measurements.

Figure 5.3 shows a horizontal slice at 3.3 km depth through the 3D Vs model. The Rhine Valley Flexure boundary is imaged very clearly. We focus our interpretation on four E-W cross-sections (Figure 5.4) and two S-N cross-sections (Figure 5.5) that intersect the deep boreholes in this area. The low-velocity signature of the Rhine Graben is obvious in all cross-sections. West of the Rhine Valley Flexure (RVF),

The syncline in the Tertiary deposits in slice H2-H2' just east of the Otterbach-2 well (around 5-8 km distance along the slice) is consistent with Figure 12 in Haering [2006] and Kind [2002]. This structure is known as the St. Jacob Tüellingen syncline and runs along the RVF. As in Figure 2 of 2.7, the "geophysical bedrock" is found at 500 m depth at Otterbach-2, but 800 m near the Riehen-1 and Riehen-2 wells.

The granitic basement at the Otterbach-2 well was reached at 2.6 km depth. In our Vs model, there is a sudden velocity increase near 2.8-3 km, which is a relatively close match to the borehole data, if we consider the Vs model is smoothed in the three directions with a 3-cell box kernel. In profile H3-H3', we see the Riehen-2 well is located just at the edge of RVF. A deep low-velocity anomaly sits at the edge of the RVF in H2-H2' and H3-H3', which suggests the RVF may provide a pathway for deep fluids infiltration into the basement. It is possible that the topography of the Dinkelberg Massif to the east facilitates fluid flow in this direction as well.

In sections H1-H1' and H4-H4', the crystalline basement below the URG appears to have a dome-like shape. While we do not aim to explain in this report every feature of our model, we point out that a lithospheric scale study by Cloetingh et al. [2005] found that the URG was likely experiencing crustal stresses in response to lithospheric folding. In this situation, they could demonstrate with a physical model that folding/bulging driven by mantle forces can propagate upward and create pronounced extensional stress in the upper 5 km of the crust. We refer the readers to Figure 11 of Cloetingh et al. [2005] for an interesting similarity in geometry. Our Vs model must however be interpreted with caution below 4 km depth, as mentioned above.

In the N-S cross-sections in Figure 5.5, we find an interesting feature related to the Riehen wells. As seen also in Figure 5.3, the lateral velocity contrast we associate with the RVF appears to bend sharply near Riehen wells and deep low-velocity anomalies sit at 3-5 km depth, at the edge of this boundary. These features might help explain why the Geo2Riehen hydrothermal wells have been successful. In section V1-V1', we note that the top of the granitic basement appears close to 3 km depth near the Basel-1 well, a value that is again close to the well-log-derived Vs model of Michel et al. [2017] (see also Figure C.1).

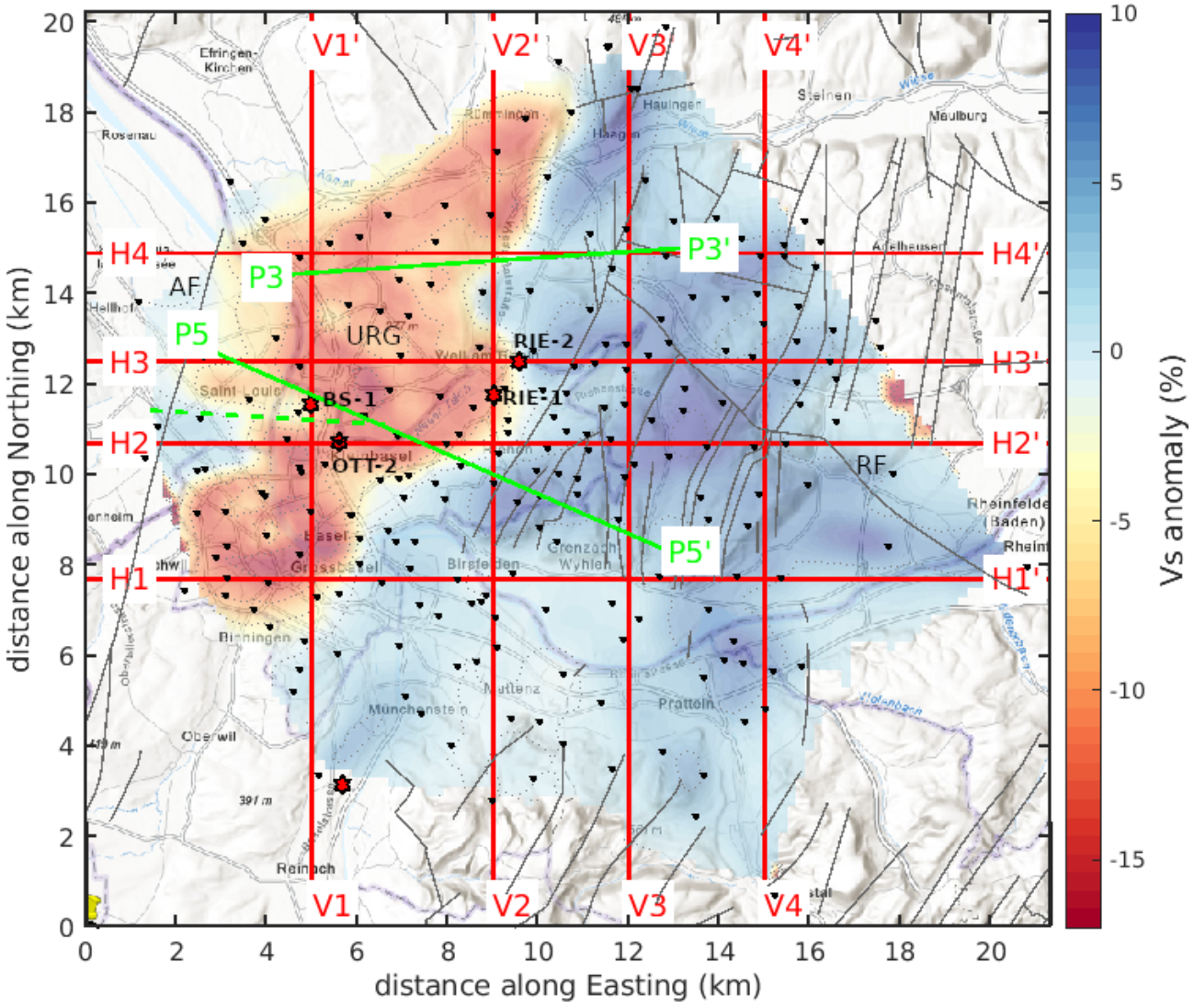


Figure 5.3: Map section at 3.3 km depth through the 3D Vs model of Riehen

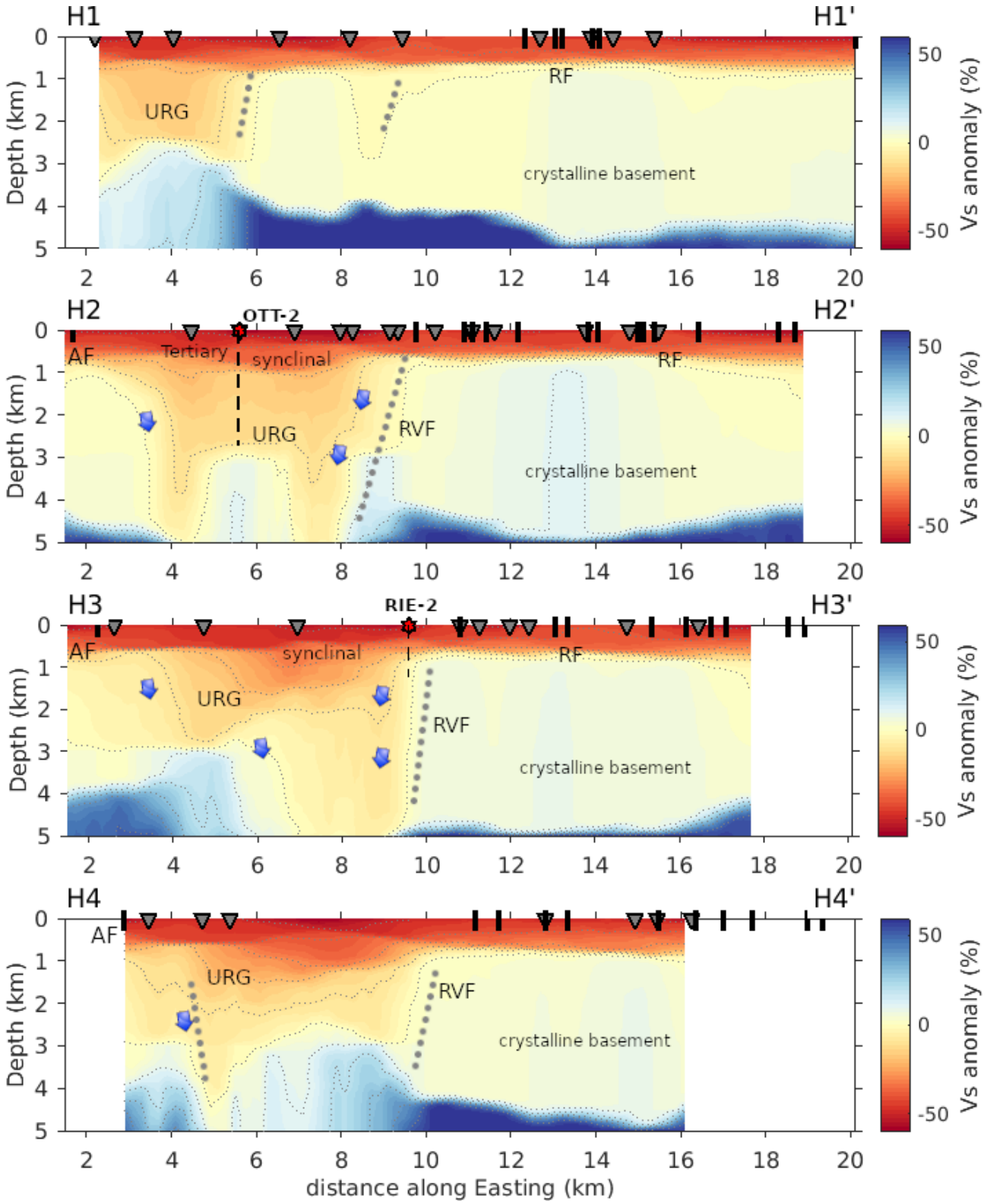


Figure 5.4: Riehen 3-D Vs model depth cross-sections along the W-E direction

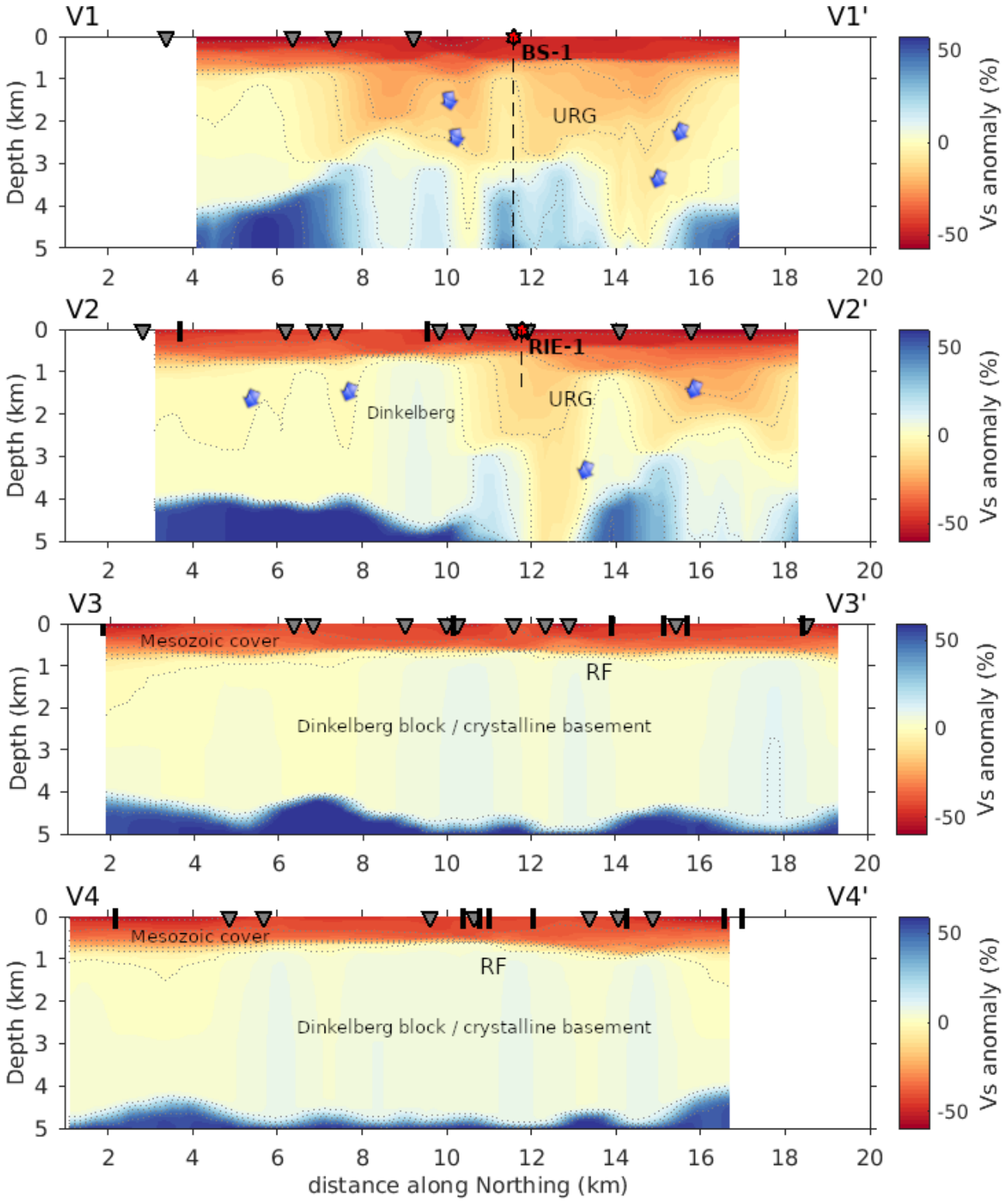


Figure 5.5: Riehen 3-D Vs model depth cross-sections along the S-N direction

5.3 Comparison to seismic reflection

At the time of writing, we did not yet have access to the results of the 3D seismic reflection survey that was made in the context of Geo2Riehen, so we limit our comparison to 2D reflection profiles from Gurler et al. [1987]. The seismic reflectivity images themselves are not present in the report of Gurler et al. [1987], only interpreted stratigraphic profiles at up to 2 km depth. We compare these interpreted cross-sections with our NANT model along the lines of profile P5-P5' (Figure 5.6) and P3-P3' (Figure 5.7). In profile P5-P5', the western endpoint of the cross-section through the NANT model does not match perfectly the real 2D reflection profile, which has a sharp bend (dashed green line in Figure 5.3), so the two profiles are not exactly the same. Nevertheless, we find a good match in the syncline position, the position of the RVF and lateral contrasts that indicate matching suspected fault lines. In the NANT image, we gain information below 2 km, where a low-velocity anomaly sits at 3 to 5 km depth, between the two faults/discontinuities. In Figure 5.7, we find again a reasonably good match in the thickness of the sedimentary cover and lateral discontinuities. Unfortunately, the "bulging" shape of the granitic basement under the URG, at around 3-4 km depth in the NANT image, can't be corroborated with these seismic reflection data. We highlight that the ability of NANT to image seamlessly at depths corresponding to the crystalline basement is one of the major advantages of this method.

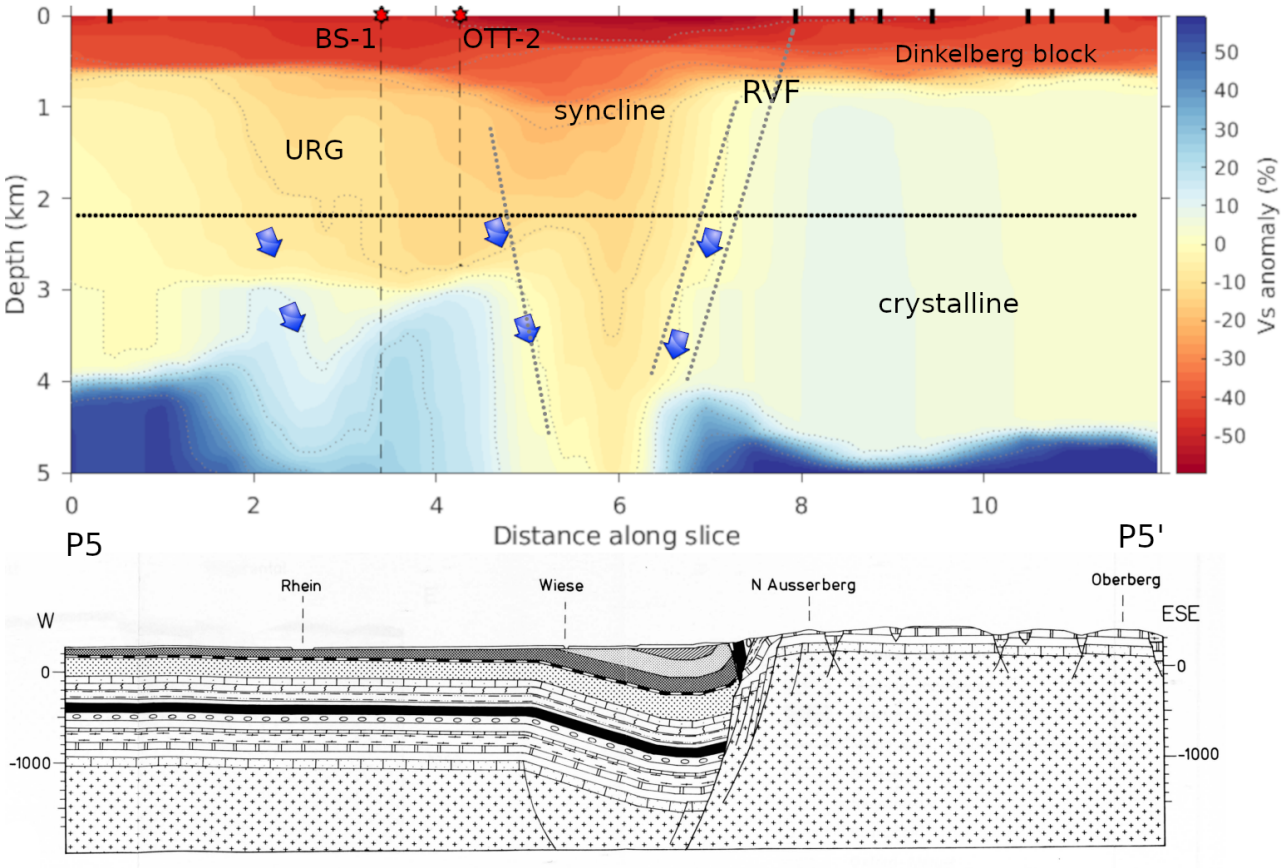


Figure 5.6: Comparison of the NANT Vs model with the interpreted model derived from the 2D seismic reflection line P5 in Gurler et al. [1987]. The black horizontal dotted line in the NANT image shows the depth limit of the 2D seismic reflection data. Dotted gray lines show suspected faults or discontinuities and blue arrows show supposed fluid pathways.

5.4 H/V ratios

Figure 5.8 shows the logarithm of H/V calculated with the same method as in Aargau. These results must however be interpreted cautiously as the Rayleigh and Love wave energy is not as well separated across the radial and transverse components as in the Aargau dataset, which may cause some inaccurate measurements. In comparison to Aargau, there are more extreme values of H/V measured, in particular along the Rhine River in Basel-Stadt, in Riehen and Lörrach. This may reflect the Quaternary sediment cover along the Rhine River (Figure 2.6) and the presence of the St. Jacob Tüellingen syncline, but the spatial pattern is not as clear at 0.4 s. The lowest values of H/V are located west of the network, where the Mesozoic bedrock cover and a shallow

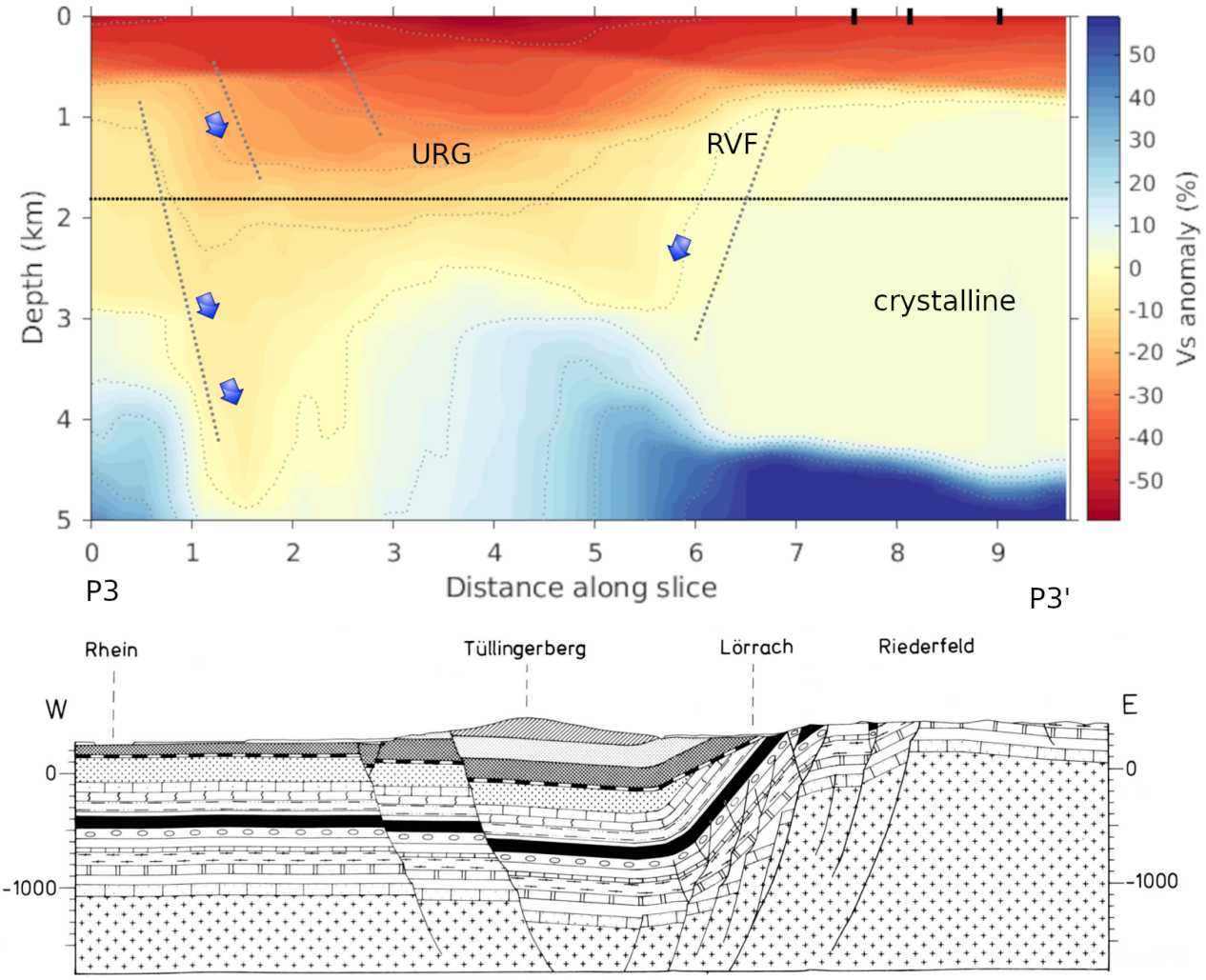


Figure 5.7: Same as Figure 5.6 but for profile P3-P3'.

crystalline basement depth are encountered. There are however obvious outlier data points, as evidenced where two neighbouring stations show drastically different H/V values, which is especially the case at 0.4 s.

At relatively high periods, H/V maps are not as easily interpreted as velocity anomalies in terms of structure. The thickness of sediments is not the only factor that can affect the H/V ratio. Okamoto et al. [2021] discovered that subsurface fluid anomalies could also have an influence. They demonstrated with numerical modelling that increasing subsurface fluids decreases the H/V ratio. Without further interpreting the H/V results presented here for Riehen, we highlight that these measurements can be used to improve the 3D Vs models via joint inversion approaches, provided outlier measurements are more carefully removed.

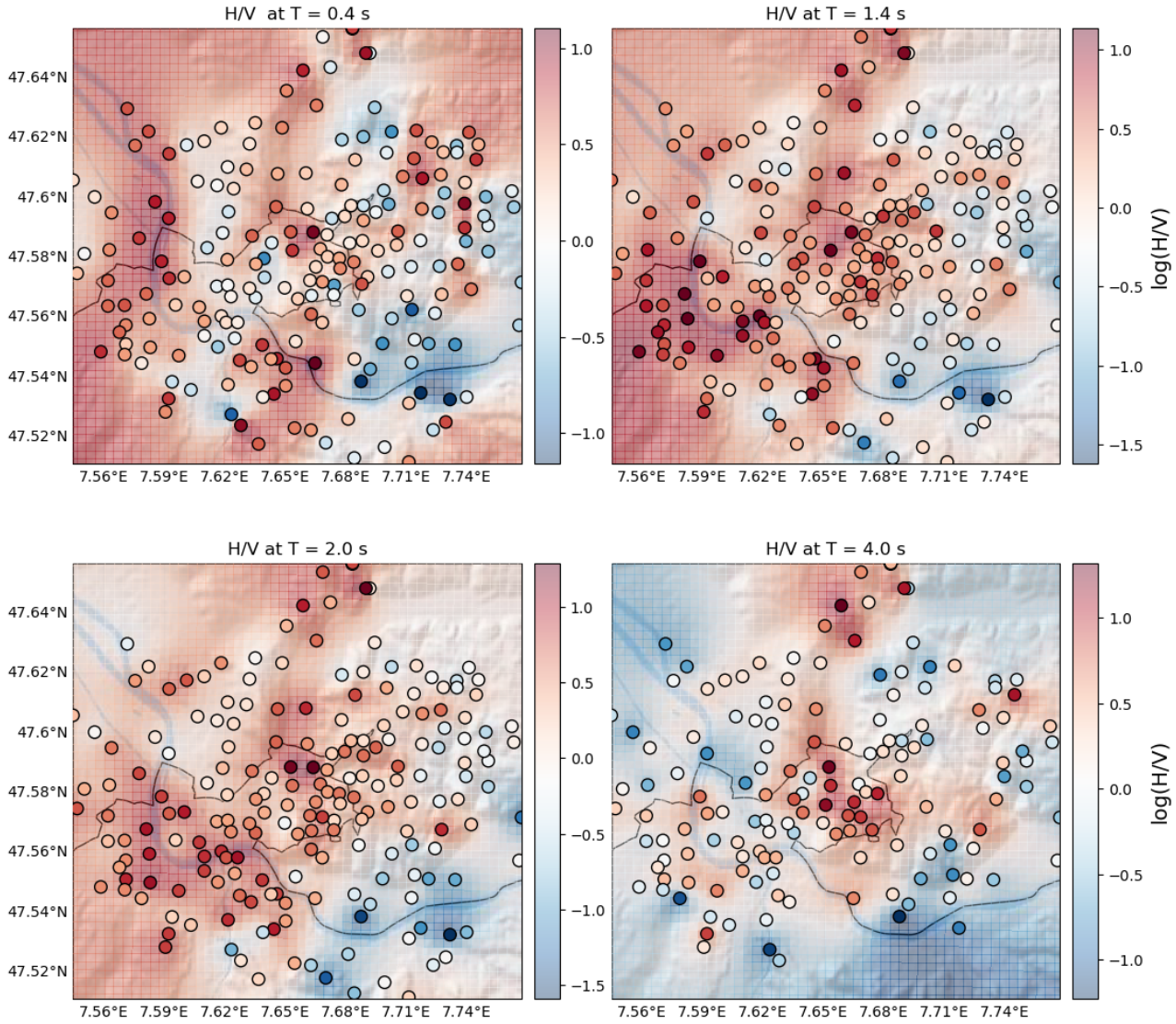


Figure 5.8: Rayleigh wave ellipticity (H/V ratio) from ambient noise cross-correlations for Riehen. Single station measurements of log(H/V) at different periods are interpolated on a grid with a radial basis function scheme.

6. Discussion of results

The PSIGE project aimed to demonstrate the potential of NANT as a geothermal exploration method. In the previous chapter, we showed that the NANT images show several consistent features with previous geological and geophysical investigations but also new information such as low-velocity domains at depth that may be linked to fluids. While we provided some preliminary interpretations in terms of structure and fluids, we stress that proper interpretations in terms of tectonics and hydrology will require future dedicated discussion among geologists and geophysicists with prior expertise in these geographic areas, including SwissTopo, SED, Erdwärme-Riehen, Nagra, etc.

6.1 Comparison to other methods

In the previous chapter, we have shown comparisons between NANT and a few 2D seismic reflection profiles. There is however a fundamental difference in resolution between the two methods. The high frequencies of body waves allow imaging of thin layers with a thickness larger or equal to a quarter of the wavelength (equal to velocity times period). However, identifying seismic reflections from deep layers is difficult, in particular when there are strong shallow scatterers, such as under the Jura Main Thrust. Lateral resolution in migrated seismic reflection data is limited by namely trace spacing and noise. With ambient noise tomography, we can also obtain high lateral resolution by increasing sensor density, but there exists a fundamental resolution limit that is about a third of the wavelength of surface waves. Since the high periods of surface waves are used to image the deeper structures, the resolution also decreases with depth. One way to improve resolution at depth is to incorporate phase velocity measurements or higher modes of surface waves, which have a higher sensitivity at depth for the same frequencies as the fundamental group velocity. Another way to improve NANT sensitivity at depth is to extract body waves, a cutting-edge topic of research in ambient noise seismology, as we mention in the Introduction. For this purpose, we have explored some techniques to extract body waves from our datasets, but have not yet succeeded, as we document in Appendix E.

We have also compared the NANT images to deep borehole data. In Riehen, there was a good match in the depth of strong vertical contrasts in the 3D model and the Vs model developed from the well logs at Basel-1 and Otterbach-2. For Aargau, there is no Vs information from the well logs at Riniken, Böttstein and Leuggern, but on a first order, strong jumps in velocities such as from the shallow crystalline basement interface at Leuggern and Böttstein, are supported by the NANT images as well.

In Appendix G, we also compared the NANT images with the Swiss 3D Vs model of Diehl et al. [2021], obtained from earthquake joint hypocenter-velocity inversion and interpolated on a 3D grid of 1 km spacing for all of Switzerland. Resolution from local earthquake tomography is inherently limited in areas of low seismicity and low station density such as Aargau, but large wavelength features in the NANT image appear consistent with the Swiss earthquake tomography model on a first order.

The assessment of uncertainties in a 3D geophysical model is important for interpretation in terms of plausible geological and hydrological features and for deciding on drilling locations with the highest likelihood of success. We have explored different ways of assessing resolution and confidence in the group velocity maps in the appendix D. For depth inversion of group velocity dispersion, we can evaluate the uncertainty bounds for the depth and velocity of each layer by examining the distribution of models generated and their misfit. In the case of both seismic reflection and NANT, the seismic models developed should be carefully interpreted with input from experienced geophysicists with a good understanding of wave physics and the methods' sensitivity, resolution and uncertainty.

We highlight that NANT allows the identification of low-velocity domains which are likely to be caused by crustal fluids, the target of geothermal exploration. Another strength of NANT is its ability to image the crystalline basement without requiring strong impedance contrasts or being limited by strong scattering from shallower structures. For geothermal electricity generation in Switzerland, the wells must reach around 5 kilometres depth, into the crystalline basement, to reach the required temperatures. With NANT, we can obtain subsurface information for arbitrarily deep targets in the upper and lower crust, and even though the resolution decreases with depth, controlled-source seismic methods cannot provide this luxury, unless at a prohibitively high financial cost and logistical burden.

6.2 NANT as a geothermal exploration tool: finding a drilling target

The ideal exploration method would be able to pinpoint exactly where to drill to find economically viable geothermal resources. Still today, 3D seismic reflection is considered the gold standard in the industry, despite failing to provide the necessary information to improve the success rate of geothermal projects in Switzerland. In a political climate where every new unsuccessful well drilled provides fuel for opponents of future geothermal projects, any new method that can image the subsurface and provide information where seismic reflection cannot deserves attention. If NANT can help explain the success or failure of past or future projects, it has the potential to be a game changer.

While NANT images should be interpreted in conjunction with other geological, geochemical and geophysical observations, as an academic exercise, we may suggest where to find promising drilling targets based on the NANT images from our two surveyed regions. In simple terms, when searching for fluids, one of the key ingredients of a successful geothermal target, we must look for low group velocity or low shear wave anomalies in the NANT images.

In the case of the Riehen campaign, the western half of Riehen itself, on the west side of the Rhine Valley Flexure and the Dinkelberg Massif, is characterized by consistently low group velocity anomalies for both Rayleigh and Love wave observations at a wide range of periods and in the inverted 3D shear wave velocity model. We found that these anomalies persist to up to 4-5 kilometre depth, into the crystalline basement, which suggests that the Rhine Valley Flexure provides the right permeability zone for circulation of crustal fluids at depth. This area is also east of an apparent bulging in the crystalline basement relief, under the Upper Rhine Graben, which would hypothetically drive a locally higher geothermal gradient at depth. The success of the Geo2Riehen hydrothermal wells supports the conclusion that the low velocities we imaged in this area indicate a promising target. New wells might benefit from targeting the same NANT anomalies, i.e. further south in Riehen or northwest in Germany, in Weil am Reich and southern Lörrach, along the same velocity contrast that the Riehen wells currently sit on.

In Aargau, we were able to image the geometry of the Constance-Frick Trough with NANT. The permeable fault zones bounding the trough and reaching deep into the crystalline basement are considered good targets for geothermal energy [Eberhard, 2016]. We found a particularly prominent low-velocity domain along the Mandach Thrust, west of the Aare River, which may indicate a particularly efficient fluid pathway. Numerical modelling of heat transport processes and a probabilistic model analysis suggested the fault zones bounding the trough may experience local fluid upflow (advective heat transport) that is not observed in existing borehole data but that may be needed to explain the heat flux distribution [Niederau, 2022]. Fluid flow is observed at the Bad Zurzach well, at the NE end of the survey area, where we see a nearby high in the topography of the crystalline basement and a strong low-velocity anomaly extending across the PC trough from the Jura Main Thrust towards the surface near Bad Zurzach (Profile V3-V3' in Figures 4.5 and 4.4). These features might suggest the heat generated from the granitic basement high encourages advection and upward flow of crustal fluids that originally seeped through a deep-reaching permeable zone, such as the southern trough boundary or from the north, along the Black Forest Massif.

Detailed characterization of the geothermal potential of Riehen and Aargau from NANT in conjunction with previous observations and modeling is out of scope for this final report, and we reserve this topic for future work and collaborations.

While the Constance-Frick Trough is well-studied thanks to decades of geophysical investigations by Nagra, such Permo-Carboniferous troughs are believed to be present in many other locations in Switzerland based on deep well logs and gravity data [Leu, 2008, Abdelfettah et al., 2014] and remain poorly constrained in geometry. In this context, NANT may be the only economically viable exploration method for systematically surveying Permo-Carboniferous troughs across Switzerland, with the aim of defining these structures' spatial extent and better constraining their role in crustal-scale fluid flow and heat flux distribution. In this sense, NANT may be a game changer for geothermal exploration in Switzerland.

7. Conclusions and outlook

The aim of PSIGE was to demonstrate the potential of passive seismic methods for geothermal exploration. PSIGE applied ambient noise tomography to data recorded with temporary dense nodal geophone arrays to image the subsurface structure. We have acquired 210 nodal geophones for the purpose of testing this method in two areas of Switzerland particularly promising for deep geothermal: the canton of Aargau and the area surrounding Riehen, Basel-Stadt. Models of the subsurface were successfully retrieved from ambient noise recordings for both regions, with characteristics consistent with the known geology in these areas but also revealing deeper structures and anomalies that were previously speculative or poorly constrained in depth. We suggest that nodal ambient noise tomography (NANT) is a reliable method to reduce subsurface uncertainty and image major structural boundaries, deep aquifers and fluid anomalies related to faults. Interpretation of NANT images benefits from other geophysical and geological data to distinguish between velocity anomalies due to fluids or geological composition, but it is complementary to traditional exploration methods that provide different subsurface information. Because of its low cost, ease of deployment and flexibility in imaging structures of varying depth, the method could be used for early prospection in regions with low to modest topography and may be applied to survey large areas for example to image the numerous Permo-Carboniferous Troughs that exist in Switzerland.

Our local campaigns in Aargau and Riehen are likely to have a positive impact for these cantons. In Aargau, local politicians have highlighted the need for further subsurface studies to encourage the exploitation of the favourable geothermal situation in this area and are building a repository of geophysical data to encourage development[1]. As for our second campaign around Riehen, we have received strong interest from representatives of several communities for our findings, as they seek to also encourage the development of successful geothermal energy projects. We will be happy to transfer the information we acquired to the competent authorities and engage with them for the further exploration of geothermal resources in these regions.

On June 18, 2023, Switzerland adopted the net-zero climate law and Swiss voters showed their support to accelerate the transition from fossil fuels to renewable energy. Moreover, the ongoing war in Ukraine has also highlighted the urgency for Europe to accelerate the path to energy supply independence. Geothermal energy is an important player in the renewable energy ecosystem because it is unaffected by environmental and atmospheric conditions the way wind, solar and hydroelectric energy are. Subsurface uncertainty and the high cost of traditional exploration methods remain important concerns for the development of geothermal energy. Now more than ever, innovative subsurface exploration approaches are needed. We believe that the NANT method can be a game changer to address these two challenges in the future.

[1] https://www.thinkgeoenergy.com/calls-for-mapping-of-geothermal-potential-in-aargau-switzerland/

8. Publications

Conference abstracts

Savard, G., Planès, T., and Lupi, M.: Ambient Noise Tomography applied to a large-N nodal network in Aargau, Switzerland, EGU General Assembly 2022, Vienna, Austria, 23–27 May 2022, EGU22-10870, https://doi.org/10.5194/egusph egu22-10870, 2022. (sollicited)

Savard G., Planès T., Lupi M. and the Crustal Deformation and Fluid Flow Group: Imaging deep shear-wave velocity structures for geothermal exploration with Ambient Noise Tomography and dense geophone arrays: a tale of two case studies at Aargau and Riehen, Switzerland, Swiss Geoscience Meeting 2022, Lausanne, Switzerland, November 19, 2022.

Bibliography

Y. Abdelfettah, E. Schill, and P. Kuhn. Characterization of geothermally relevant structures at the top of crystalline basement in Switzerland by filters and gravity forward modelling. *Geophysical Journal International*, 199(1):226–241, 08 2014. ISSN 0956-540X. doi: 10.1093/gji/ggu255. URL https://doi.org/10.1093/gji/ggu255.

G. D. Bensen, M. H. Ritzwoller, M. P. Barmin, A. L. Levshin, F.-C. Lin, M. P. Moschetti, N. M. Shapiro, and Y. Yang. Processing seismic ambient noise data to obtain reliable broad-band surface wave dispersion measurements. *Geophysical Journal International*, 169(3):1239–1260, jun 2007. ISSN 0956540X. doi: 10.1111/j.1365-246X.2007.03374.x.

E. M. Berg, F.-C. Lin, V. Schulte-Pelkum, A. Allam, H. Qiu, and K. Gkogkas. Shallow Crustal Shear Velocity and Vp/Vs Across Southern California: Joint Inversion of Short-Period Rayleigh Wave Ellipticity, Phase Velocity, and Teleseismic Receiver Functions. *Geophysical Research Letters*, 48(15):1–11, 2021. ISSN 19448007. doi: 10.1029/2021GL092626.

D. C. Bowden, K. Sager, A. Fichtner, and M. Chmiel. Connecting beamforming and kernel-based noise source inversion. *Geophysical Journal International*, 224(3):1607–1620, 2021. ISSN 1365246X. doi: 10.1093/gji/ggaa539.

M. Campillo, S. K. Singh, N. Shapiro, J. Pacheco, and R. B. Herrmann. Crustal structure south of the Mexican volcanic belt, based on group velocity dispersion. *Geofisica Internacional*, 35(4):361–370, 1996. ISSN 00167169. doi: 10.22201/igeof.00167169p.1996.35.4.529.

S. Cloetingh, P. A. Ziegler, F. Beekman, P. A. Andriessen, N. Hardebol, and P. Dèzes. Intraplate deformation and 3D rheological structure of the Rhine Rift System and adjacent areas of the northern Alpine foreland. *International Journal of Earth Sciences*, 94(4):758–778, 2005. ISSN 14373254. doi: 10.1007/s00531-005-0502-3.

B. Delacou, M. Sartori, F. Philippossian, J. Savary, and G. Grosjean. Deep heat mining basel - seismic risk analysis - serianex - geological model ap 2000 report - structural model of potential seismogenic faults. 11 2009.

T. Diehl, E. Kissling, M. Herwegh, and S. M. Schmid. Improving Absolute Hypocenter Accuracy With 3D Pg and Sg Body-Wave Inversion Procedures and Application to Earthquakes in the Central Alps Region. *Journal of Geophysical Research: Solid Earth*, 126(12), 2021. ISSN 21699356. doi: 10.1029/2021JB022155.

M. Eberhard. Geothermie im kanton aargau. *Aarg. Naturf. Ges. Mitt.*, 38:81–112, 2016.

A. Fichtner, B. L. Kennett, H. Igel, and H. P. Bunge. Theoretical background for continental- and global-scale full-waveform inversion in the time-frequency domain. *Geophysical Journal International*, 175(2):665–685, 2008. ISSN 0956540X. doi: 10.1111/j.1365-246X.2008.03923.x.

L. Gegg, G. Deplazes, L. Keller, H. Madritsch, T. Spillmann, F. S. Anselmetti, and M. W. Buechi. 3D morphology of a glacially overdeepened trough controlled by underlying bedrock geology. *Geomorphology*, 394 (September), 2021. ISSN 0169555X. doi: 10.1016/j.geomorph.2021.107950.

N. Gu, J. Gao, B. Wang, R. Lu, B. Liu, X. Xu, and H. Zhang. Ambient noise tomography of local shallow structure of the southern segment of tanlu fault zone at suqian, eastern china. *Tectonophysics*, 825:229234, 2022. ISSN 0040-1951. doi: https://doi.org/10.1016/j.tecto.2022.229234. URL https://www.sciencedirect.com/science/article/pii/S0040195122000282.

B. Gurler, L. Hauber, and M. Schwander. Die geologie der umgebung von basel mit hinweisen über die nutzungsmöglichkeiten der erdwärme. *Beiträge zur geologischen Karte der Schweiz*, 160, 1987.

M. Haering. technischer bericht geothermie-sondierbohrung otterbach 2. Technical report, basel. technical report. Geothermal Explorer Ldt. Pratteln, switzerland, 2006.

E. Hand. A boom in boomless seismology. *Science*, 345(6198):720–721, 2014. ISSN 10959203. doi: 10.1126/science.345.6198.720.

C. Harvey, G. Beardsmore, I. S. Moeck, H. D. Ruter, and S. Bauer. Best Practices Guide for Geothermal Exploration. Technical report, IGA Service GmbH, Bochum, Germany, 2014.

G. Hillers, M. Campillo, Y. Ben-Zion, and M. Landès. Interaction of microseisms with crustal heterogeneity: A case study from the San Jacinto fault zone area. *Geochemistry, Geophysics, Geosystems*, 14(7):2182–2197, 2013. ISSN 15252027. doi: 10.1002/ggge.20140.

G. Hillers, S. Husen, A. Obermann, T. Planès, E. Larose, and M. Campillo. Noise-based monitoring and imaging of aseismic transient deformation induced by the 2006 Basel reservoir stimulation. *Geophysics*, 80(4):KS51–KS68, 2015. ISSN 19422156. doi: 10.1190/geo2014-0455.1.

S. Huber. Persistent Homology in Data Science. *Data Science – Analytics and Applications*, pages 81–88, 2021. doi: 10.1007/978-3-658-32182-6_13.

S. Husen, E. Kissling, and J. F. Clinton. Local and regional minimum 1D models for earthquake location and data quality assessment in complex tectonic regions: Application to Switzerland. *Swiss Journal of Geosciences*, 104(3):455–469, dec 2011. ISSN 16618726. doi: 10.1007/s00015-011-0071-3.

M. Huwiler. Das geothermie-project der stadt st. gallen – aktueller stand. Presentation at the roundtable Tiefengeothermie 2012, 2012.

S. Jenne, K. Young, and H. Thorsteinsson. Development of Metric for Measuring the Impact of Rd&D Funding on Gto'S Geothermal Exploration Goals. In *PROCEEDINGS, Thirty-Eighth Workshop on Geothermal Reservoir Engineering*, 2013. URL `http://en.openei.org/wiki/Exploration_Techniques`.

C. Jiang and M. A. Denolle. NoisePy: A New High-Performance Python Tool for Ambient-Noise Seismology. *Seismological Research Letters*, (May), 2020. ISSN 0895-0695. doi: 10.1785/0220190364.

M. Karimpour, E. Slob, and L. V. Socco. Comparison of straight-ray and curved-ray surface wave tomography approaches in near-surface studies. *Solid Earth*, 13(10):1569–1583, 2022. ISSN 18699529. doi: 10.5194/se-13-1569-2022.

F. J. P. Kind. *Development of microzonation methods. application to Basle, Switzerland*. Doctoral thesis, ETH Zurich, Zürich, 2002. Diss., Naturwissenschaften ETH Zürich, Nr. 14548, 2002.

M. Lehujeur, J. Vergne, J. Schmittbuhl, and A. Maggi. Characterization of ambient seismic noise near a deep geothermal reservoir and implications for interferometric methods: a case study in northern Alsace, France. *Geothermal Energy*, 3(1), jan 2015. ISSN 21959706. doi: 10.1186/s40517-014-0020-2.

M. Lehujeur, J. Vergne, A. Maggi, and J. Schmittbuhl. Ambient noise tomography with non-uniform noise sources and low aperture networks: Case study of deep geothermal reservoirs in northern Alsace, France. *Geophysical Journal International*, 208(1):193–210, jan 2017. ISSN 1365246X. doi: 10.1093/gji/ggw373.

M. Lehujeur, J. Vergne, J. Schmittbuhl, D. Zigone, and A. Le Chenadec. Reservoir Imaging Using Ambient Noise Correlation From a Dense Seismic Network. *Journal of Geophysical Research: Solid Earth*, 123(8):6671–6686, aug 2018. ISSN 21699356. doi: 10.1029/2018JB015440.

W. Leu. Permokarbon-kartenskizze kompilation eines gis-datensatzes auf der basis von bestehenden unterlagen (bereich schweizer mittelland). Technical report, Nagra Arbeitsber NAB 08-49, 2008.

A. L. Levshin, A.L, Yanovskaya, T.B, Lander, A.V, Bukchin, B.G, Barmin, M.P, Ratnikova, L.I, and Its. Seismic Surface Waves in Laterally Inhomogeneous Earth. (February), 1989. URL `https://www.researchgate.net/publication/235641683_Seismic_Surface_Waves_in_Laterally_Inhomogeneous_Earth`.

F.-C. Lin, V. C. Tsai, and B. Schmandt. 3-D crustal structure of the western United States: Application of Rayleigh-wave ellipticity extracted from noise cross-correlations. *Geophysical Journal International*, 198(2):656–670, 2014. ISSN 1365246X. doi: 10.1093/gji/ggu160.

C. Liu and H. Yao. Surface Wave Tomography with Spatially Varying Smoothing Based on Continuous Model Regionalization. *Pure and Applied Geophysics*, 174(3):937–953, 2017. ISSN 14209136. doi: 10.1007/s00024-016-1434-5.

H. Madritsch, H. Naef, B. Meier, H. J. Franzke, and G. Schreurs. Architecture and Kinematics of the Constance-Frick Trough (Northern Switzerland): Implications for the Formation of Post-Variscan Basins in the Foreland of the Alps and Scenarios of Their Neogene Reactivation. *Tectonics*, 37(7):2197–2220, 2018. ISSN 19449194. doi: 10.1029/2017TC004945.

V. Maupin and J. Park. *Theory and Observations – Wave Propagation in Anisotropic Media*, volume 1-10. 2007. ISBN 9780444527486. doi: 10.1016/B978-044452748-6.00007-9.

D. E. McNamara and R. P. Buland. Ambiente noise levels in the continental United States. *Bulletin of the Seismological Society of America*, 94(4):1517–1527, 2004. ISSN 00371106. doi: 10.1785/012003001.

C. Michel, D. Fäh, B. Edwards, and C. Cauzzi. Site amplification at the city scale in Basel (Switzerland) from geophysical site characterization and spectral modelling of recorded earthquakes. *Physics and Chemistry of the Earth*, 98:27–40, 2017. ISSN 14747065. doi: 10.1016/j.pce.2016.07.005.

J. P. Montagner. Regional three-dimensional structures using long-period surface waves. *Annales Geophysicae, Series B*, 4 B(3):283–294, 1986.

N. Nakata, J. P. Chang, J. F. Lawrence, and P. Boué. Body wave extraction and tomography at Long Beach, California, with ambient-noise interferometry. *Journal of Geophysical Research: Solid Earth*, 120(2):1159–1173, 2015. ISSN 21699356. doi: 10.1002/2015JB011870.

A. Nayak, T. Taira, D. S. Dreger, and R. Gritto. Empirical Green's tensor retrieved from ambient noise cross-correlations at The Geysers geothermal field, Northern California. *Geophysical Journal International*, 213(1): 340–369, 2018. ISSN 1365246X. doi: 10.1093/gji/ggx534.

J. Niederau. Pilot study to determine the geothermal heat flux distribution in the canton of aargau. Technical report, ETH Zürich, 2022.

A. Obermann, T. Kraft, E. Larose, and S. Wiemer. Potential of ambient seismic noise techniques tomonitor the St. Gallen geothermal site (Switzerland). *Journal of Geophysical Research: Solid Earth*, 120(6):4301–4316, 2015. ISSN 21699356. doi: 10.1002/2014JB011817.

K. Okamoto and S. Tsuno. Numerical Studies of Effects of Dipping Structures on Horizontal/Vertical Spectral Ratios. *Pure and Applied Geophysics*, 175(8):2837–2852, 2018. ISSN 14209136. doi: 10.1007/s00024-018-1825-x.

K. Okamoto, H. Asanuma, and H. Nimiya. Fluid activity detection in geothermal areas using a single seismic station by monitoring horizontal-to-vertical spectral ratios. *Scientific Reports*, 11(1):1–9, 2021. ISSN 20452322. doi: 10.1038/s41598-021-86775-1. URL https://doi.org/10.1038/s41598-021-86775-1.

T. Planès, A. Obermann, V. Antunes, and M. Lupi. Ambient-noise tomography of the Greater Geneva Basin in a geothermal exploration context. *Geophysical Journal International*, 220(1):370–383, jan 2020. ISSN 1365246X. doi: 10.1093/gji/ggz457.

G. A. Prieto, J. F. Lawrence, and G. C. Beroza. Anelastic Earth structure from the coherency of the ambient seismic field. *Journal of Geophysical Research: Solid Earth*, 114(7):1–15, 2009. ISSN 21699356. doi: 10.1029/2008JB006067.

N. Rawlinson and M. Sambridge. Wave front evolution in strongly heterogeneous layered media using the fast marching method. *Geophysical Journal International*, 156(3):631–647, 2004. ISSN 0956540X. doi: 10.1111/j.1365-246X.2004.02153.x.

N. Rawlinson and W. Spakman. On the use of sensitivity tests in seismic tomography. *Geophysical Journal International*, 205(2):1221–1243, 2016. ISSN 1365246X. doi: 10.1093/gji/ggw084.

P. Sánchez-Pastor, A. Obermann, M. Schimmel, C. Weemstra, A. Verdel, and P. Jousset. Short- and Long-Term Variations in the Reykjanes Geothermal Reservoir From Seismic Noise Interferometry. *Geophysical Research Letters*, 46(11):5788–5798, 2019. ISSN 19448007. doi: 10.1029/2019GL082352.

M. Schimmel and H. Paulssen. Noise reduction and detection of weak, coherent signals through phase-weighted stacks. *Geophysical Journal International*, 130(2):497–505, 1997. ISSN 0956540X. doi: 10.1111/j.1365-246X.1997.tb05664.x.

S. Schnaidt and G. Heinson. Bootstrap resampling as a tool for uncertainty analysis in 2-D magnetotelluric inversion modelling. *Geophysical Journal International*, 203(1):92–106, 08 2015. ISSN 0956-540X. doi: 10.1093/gji/ggv264. URL https://doi.org/10.1093/gji/ggv264.

J. A. Sethian and A. M. Popovici. 3-D traveltime computation using the fast marching method. *Geophysics*, 64 (2):516–523, 1999. ISSN 00168033. doi: 10.1190/1.1444558.

R. Snieder. Extracting the Green's function from the correlation of coda waves: A derivation based on stationary phase. *Physical Review E - Statistical Physics, Plasmas, Fluids, and Related Interdisciplinary Topics*, 69(4): 8, apr 2004. ISSN 1063651X. doi: 10.1103/PhysRevE.69.046610. URL http://link.aps.org/doi/10.1103/PhysRevE.69.046610.

T. Taira, N. Avinash, F. Brenguier, and M. Manga. Monitoring reservoir response to earthquakes and fluid extraction, salton sea geothermal field, California. *Science Advances*, 4(1):1–11, 2018. ISSN 23752548. doi: 10.1126/sciadv.1701536.

A. Tarantola and B. Valette. Generalized nonlinear inverse problems solved using the least squares criterion. *Reviews of Geophysics*, 20(2):219, 1982a.

A. Tarantola and B. Valette. Inverse problems = quest for information. *Journal of Geophysics - Zeitschrift fur Geophysik*, 50(3):159–170, 1982b.

A. Trnkoczy. Understanding and Setting STA/LTA Trigger Algorithm Parameters for the K2. (August), 1998.

D. Wells, F.-C. Lin, K. Pankow, B. Baker, and J. Bartley. Combining Dense Seismic Arrays and Broadband Data to Image the Subsurface Velocity Structure in Geothermally Active South-Central Utah. *Journal of Geophysical Research: Solid Earth*, 127(7), jul 2022. ISSN 21699356. doi: 10.1029/2022JB024070.

X. Yang, Y. Luo, H. Xu, and K. Zhao. Shear wave velocity and radial anisotropy structures beneath the central Pacific from surface wave analysis of OBS records. *Earth and Planetary Science Letters*, 534:116086, 2020. ISSN 0012821X. doi: 10.1016/j.epsl.2020.116086. URL https://doi.org/10.1016/j.epsl.2020.116086.

Y. Yang and M. H. Ritzwoller. Characteristics of ambient seismic noise as a source for surface wave tomography. *Geochemistry, Geophysics, Geosystems*, 9(2), 2008. ISSN 15252027. doi: 10.1029/2007GC001814.

Q. Zeng, F.-C. Lin, and A. A. Allam. 3D Shear Wave Velocity Model of Salt Lake Valley via Rayleigh Wave Ellipticity across a Temporary Geophone Array. *The Seismic Record*, 2(2):127–136, 2022. ISSN 2694-4006. doi: 10.1785/0320220016.

D. Zigone, Y. Ben-Zion, M. Campillo, and P. Roux. Seismic Tomography of the Southern California Plate Boundary Region from Noise-Based Rayleigh and Love Waves. *Pure and Applied Geophysics*, 172(5): 1007–1032, 2015. ISSN 14209136. doi: 10.1007/s00024-014-0872-1.

D. Zigone, Y. Ben-Zion, M. Lehujeur, M. Campillo, G. Hillers, and F. L. Vernon. Imaging subsurface structures in the San Jacinto fault zone with high-frequency noise recorded by dense linear arrays. *Geophysical Journal International*, 217(2):879–893, 2019. ISSN 1365246X. doi: 10.1093/gji/ggz069.

A. Data quality control

A.1 Node metadata

Example of quality control record for one of the geophone deployed in Riehen. Inspection of this metadata facilitates the indentification of bad records or stations poorly coupled to the ground motion. See section 2.5 in the main text.

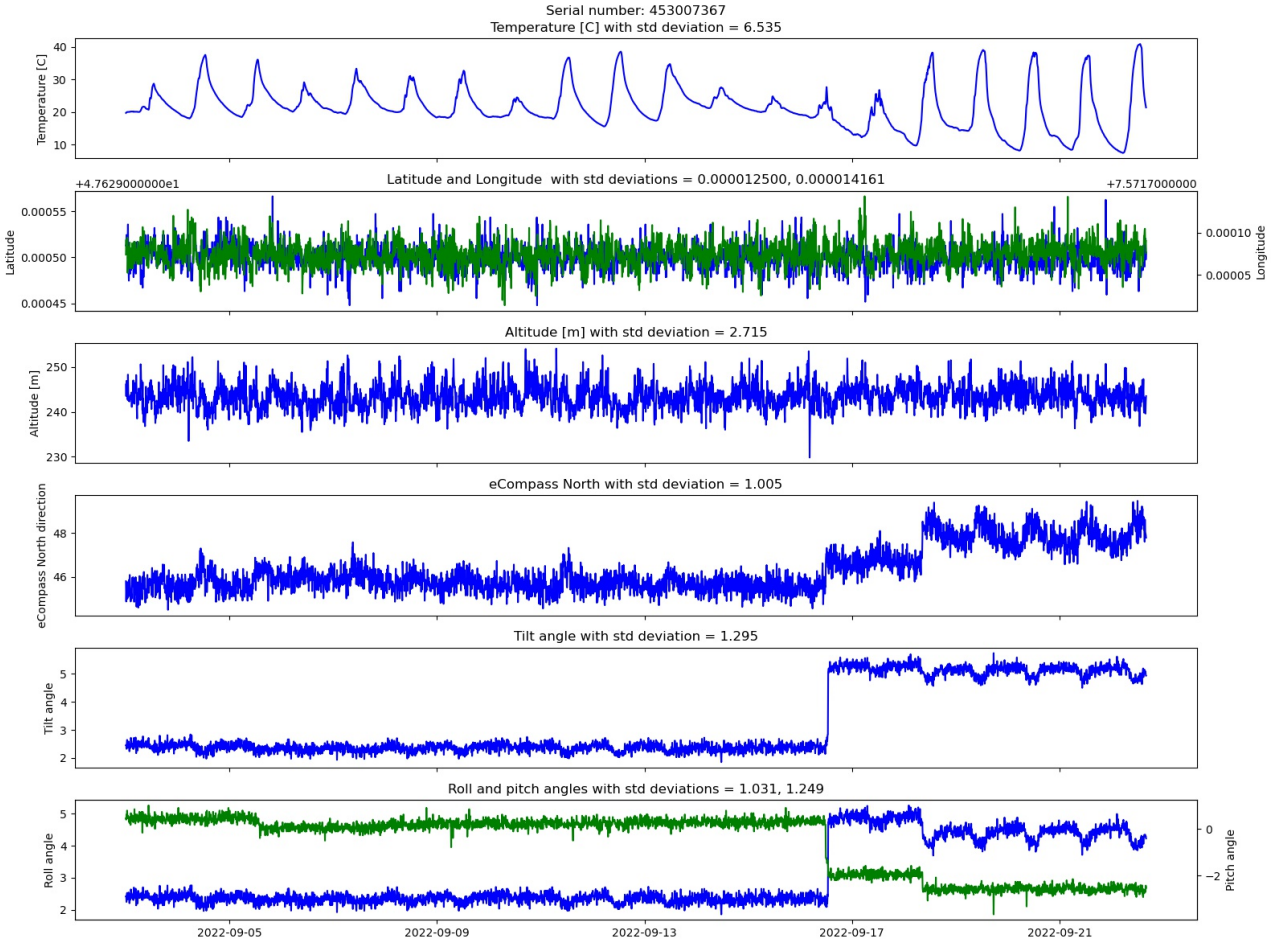
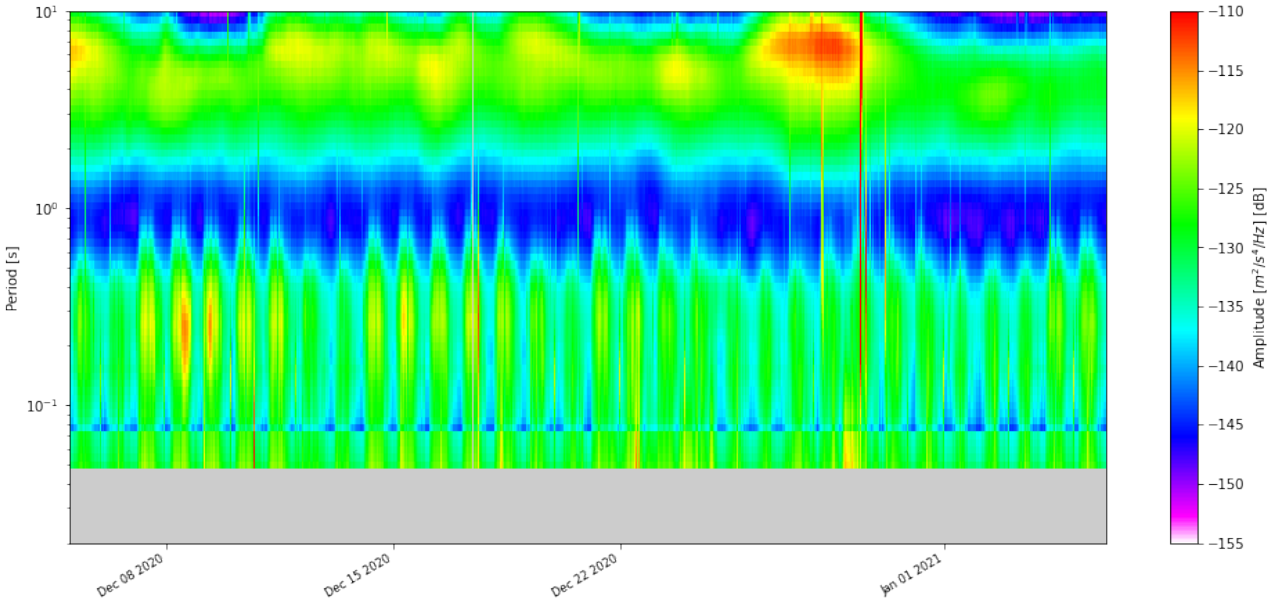


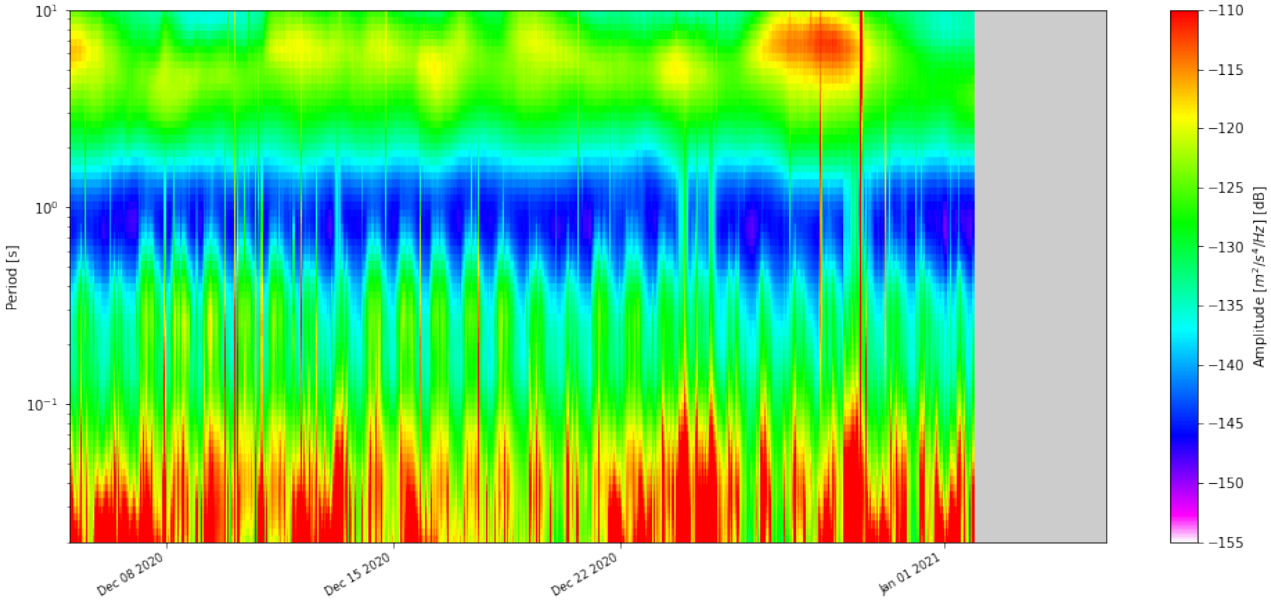
Figure A.1: Example of quality control data for one geophone from the Riehen network. Around September 16, the data indicate the node was disturbed and possibly taken out of the ground, due to the observed jumps shown by the position sensors (tilt, roll and pitch angles) and the increased day-night contrast recorded by the internal temperature sensor. Note the eCompass was not calibrated prior to the experiment so the absolute value shown is arbitrary. The nodes were oriented in the field using a compass

A.2 Comparison to broadband seismometer

Comparison of time variations of Probabilitic Power Spectral Density (PPSD) for a SmartSolo nodal geophone and a Nanometrics Trillium 240s broadband station from the permanent Swiss network. See section 3.1 in the main text for details.



(a) Broadband station ACB (Nanometrics Trillium 240 s)

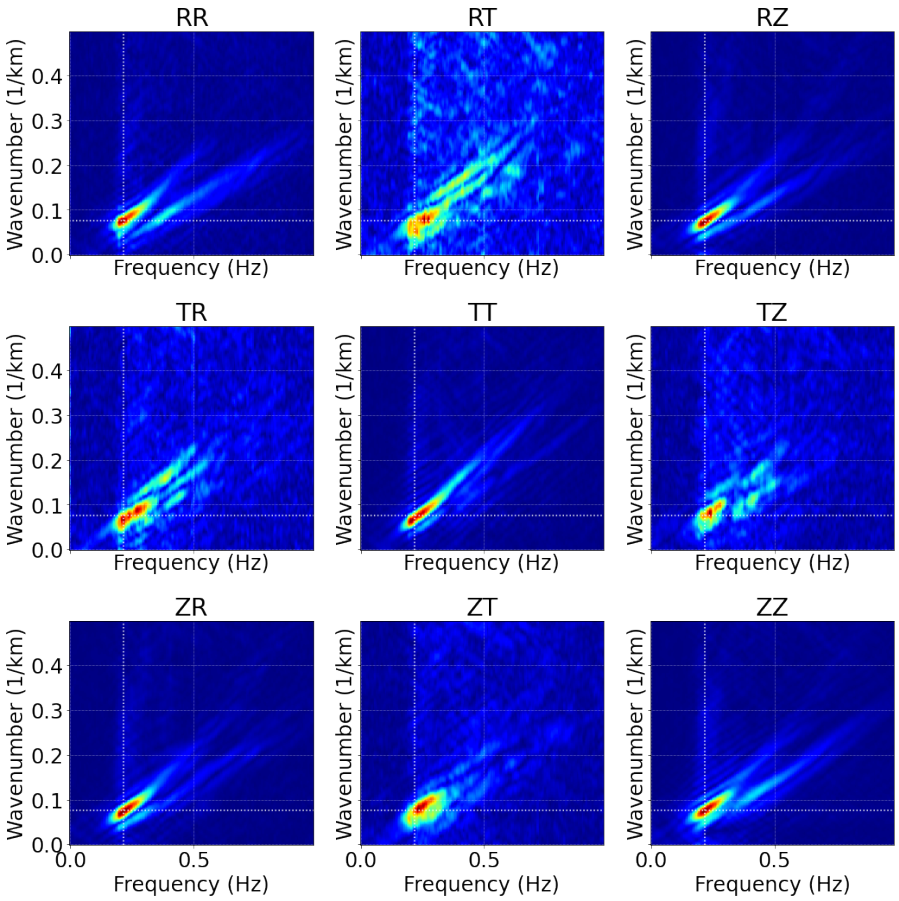


(b) SmartSolo 5 Hz geophone (3007367)

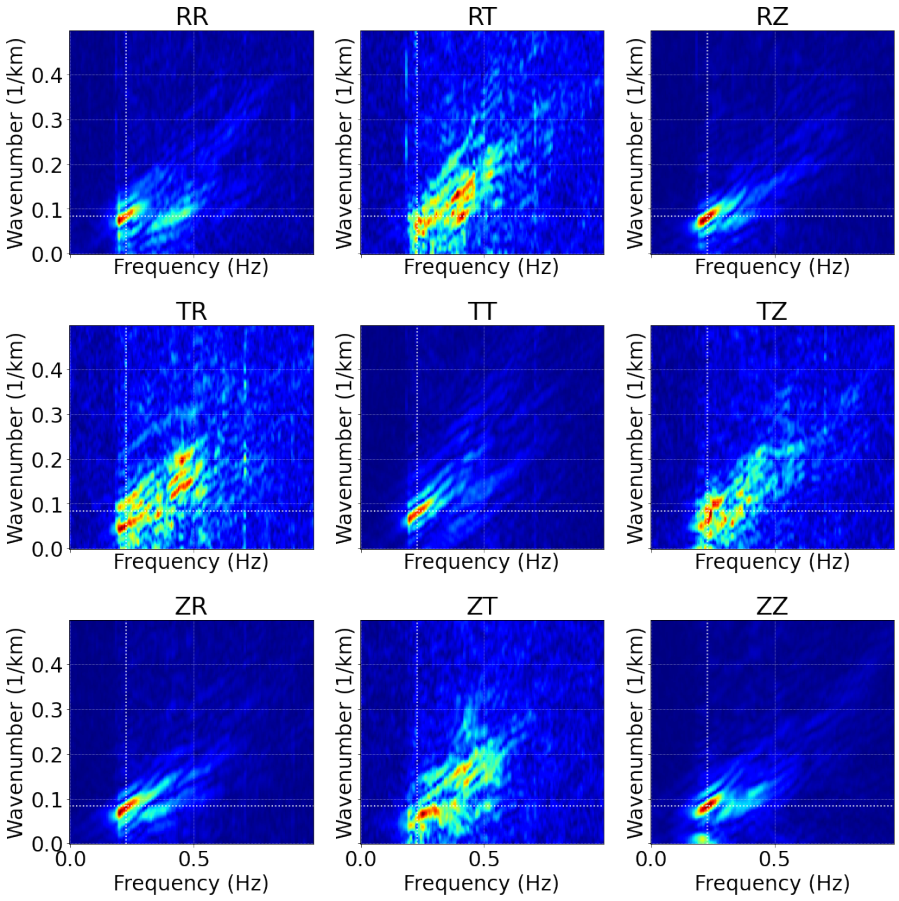
Figure A.2: Comparison of the time-varying spectral characteristics of noise for SED broadband station ACB and a geophone located closeby between December 4 2020 and January 5 2021.

B. FK decomposition of the recovered wavefield

Figure B.1 shows the frequency-wavenumber decomposition of the cross-correlation tensors. Linear trends in these graphs indicate surface waves (velocity depends on frequency). The FK plots were constructed with an inter-station bin size of 150 m.



(a) Aargau dataset



(b) Riehen dataset

Figure B.1: Representation in the frequency-wavenumber (FK) domain of the cross-correlation tensors in Figures 3.5 and 3.6.

C. Predicted dispersion and sensitivity kernels

In Figure 3.8 of the main text, the sensitivity kernels predicted for the Swiss 1D model of Husen et al. [2011] were shown. For completeness, the senstivity kernels and the predicted dispersion curves with local 1D models for Aargau and Riehen extracted from other sources are shown. The cyan and magenta curves in Figure 3.10 and 3.11 were made with these local models.

C.1 Riehen

For Riehen, the Vs model of Michel et al. [2017] is used. This model includes low-velocity layers, and was derived from a combination of well logs from Basel-1 and Otterbach-2, which reach 5 km deep and are both located to the east of the Rhine Valley Flexure, above the Rhine Graben. Figures C.1 and C.2 show the sensitivity kernels and predicted dispersion for this model.

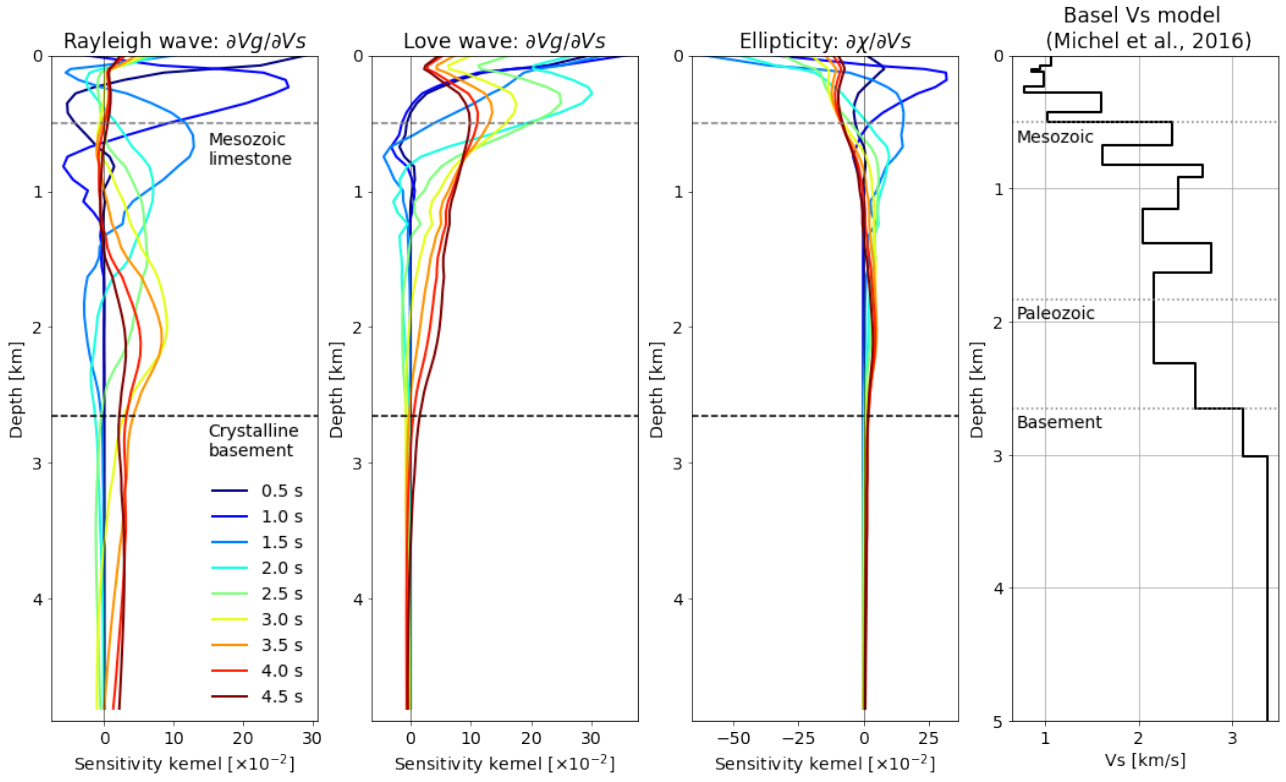


Figure C.1: Calculated sensitivity kernels for the Vs model of Michel et al. [2017].

C.2 Aargau

For Aargau, the well logs of Riniken, Boettstein and Leuggern only include Vp velocities. We derive Vs models by dividing the Vp profiles (”geological interval Vp” in the Nagra reports) with a Vp/Vs ratio of 1.73, a standard value for the Earth’s crust. Riniken is located above the Permo-Carboniferous trough, and did not reach the crystalline basement below. Is it 1800 m deep. Boettstein and Leuggern are situated in the northern part of the

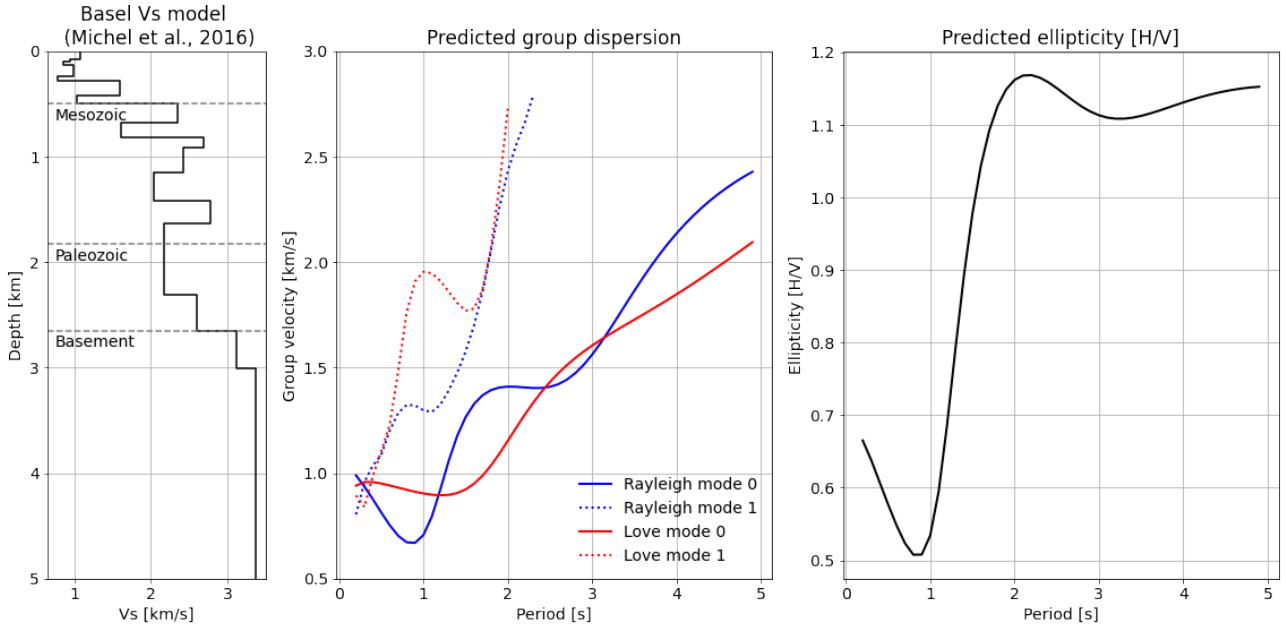


Figure C.2: Calculated Rayleigh and Love dispersion curves and ellipticity for the Vs model of Michel et al. [2017].

NANT network and the trough, where the crystalline basement (granite and gneiss) is reached at shallow depths (approximately 317 and 229 m, respectively). Theses wells are 1500 m and 1631 m deep, respectively. Since they have similar Vp profile, only Boettstein is shown here. For modelling sensitivity kernels and dispersion curves for the upper 5 km of the crust, the velocity of the last layer, in the crystalline basement, is extended to an half-space.

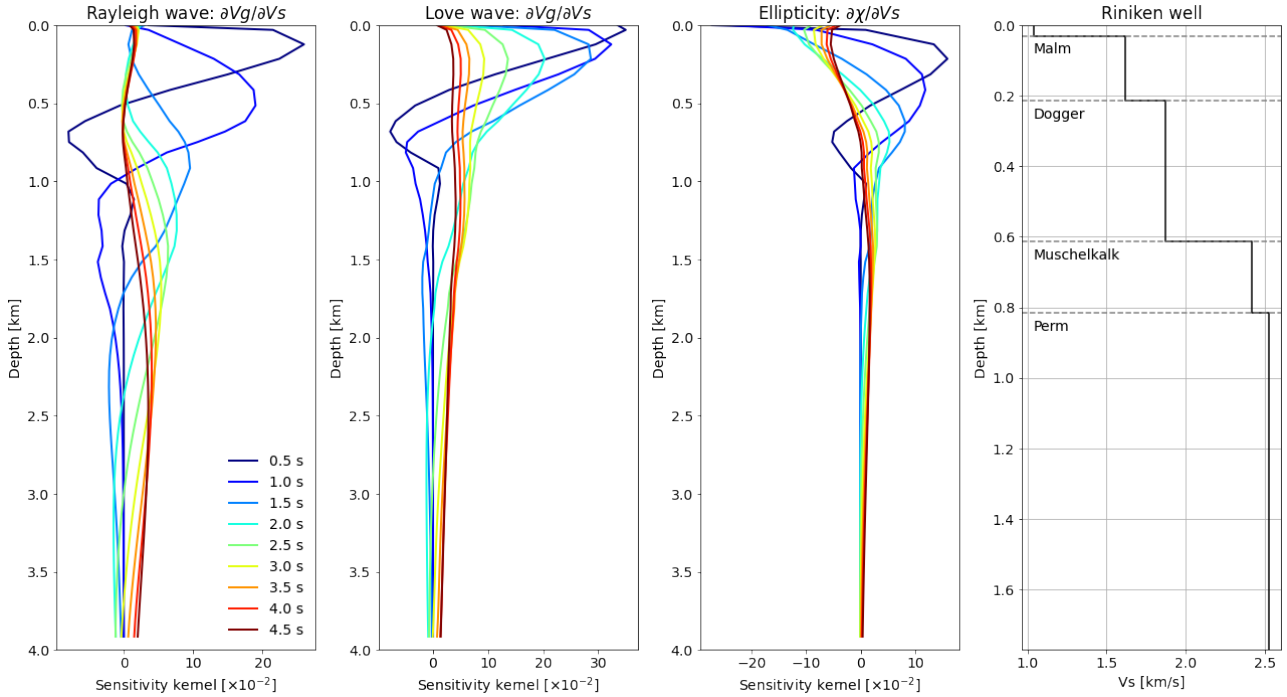


Figure C.3: Calculated sensitivity kernels for the Riniken well geological interval Vp log, assuming a constant Vp/Vs ratio of 1.73.

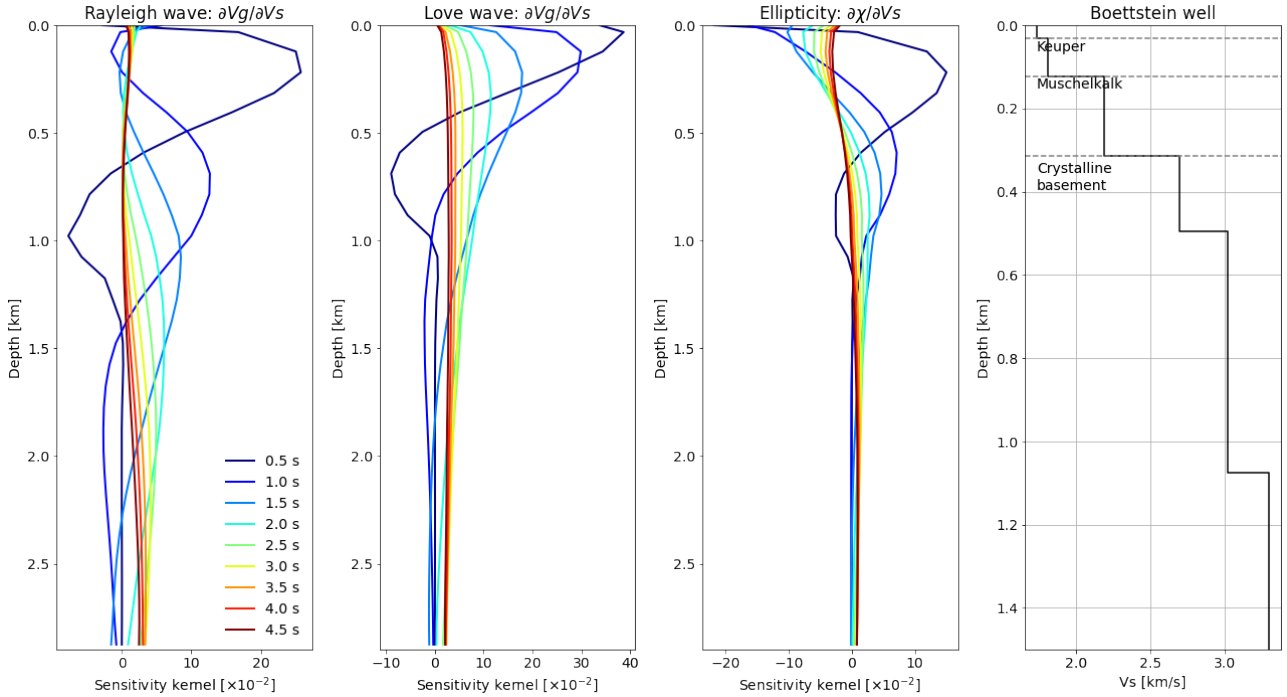


Figure C.4: Calculated sensitivity kernels for the Boettstein well geological interval Vp log, assuming a constant Vp/Vs ratio of 1.73.

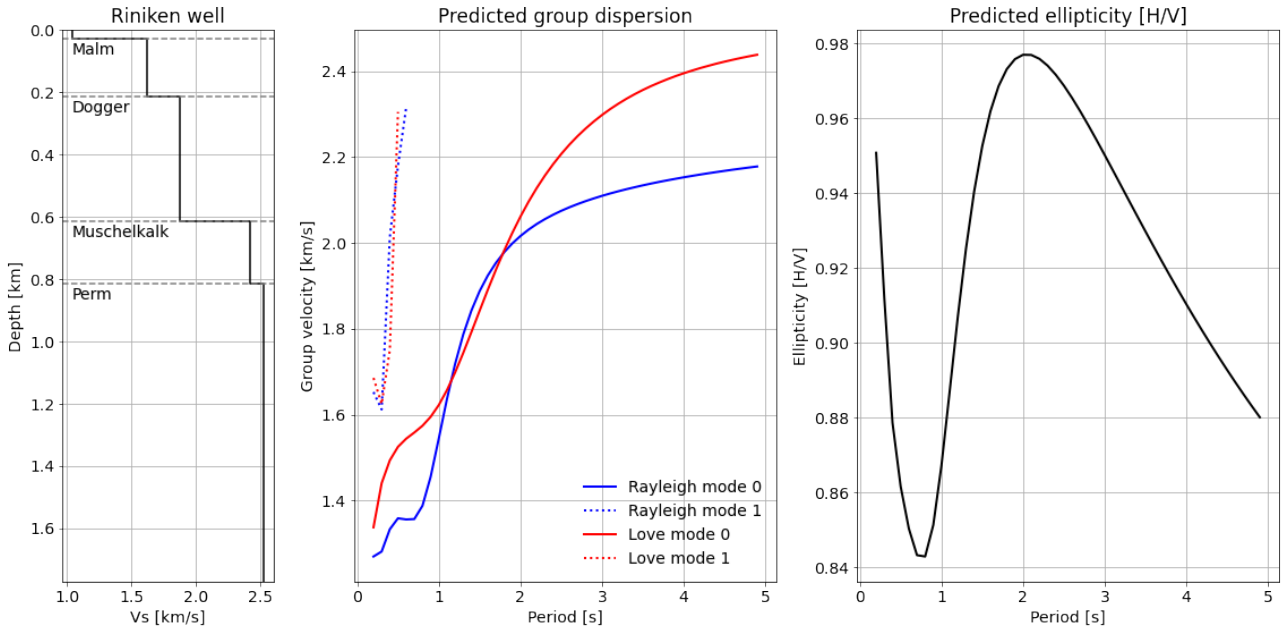


Figure C.5: Calculated Rayleigh and Love dispersion curves and ellipticity for the Riniken well geological interval Vp log, assuming a constant Vp/Vs ratio of 1.73.

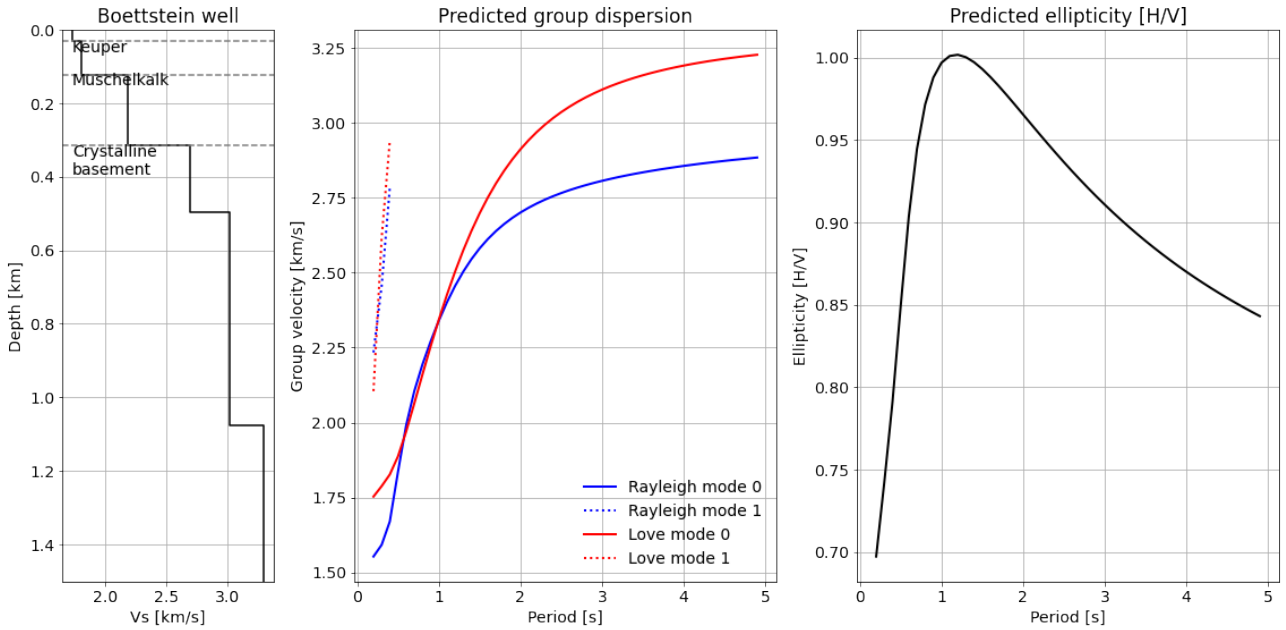


Figure C.6: Calculated Rayleigh and Love dispersion curves and ellipticity for the Boettstein well geological interval Vp log, assuming a constant Vp/Vs ratio of 1.73.

D. Uncertainty and resolution estimation

Below are detailed different methods explored to evaluate resolution and uncertainty in the group velocity maps.

D.1 Checkerboard tests

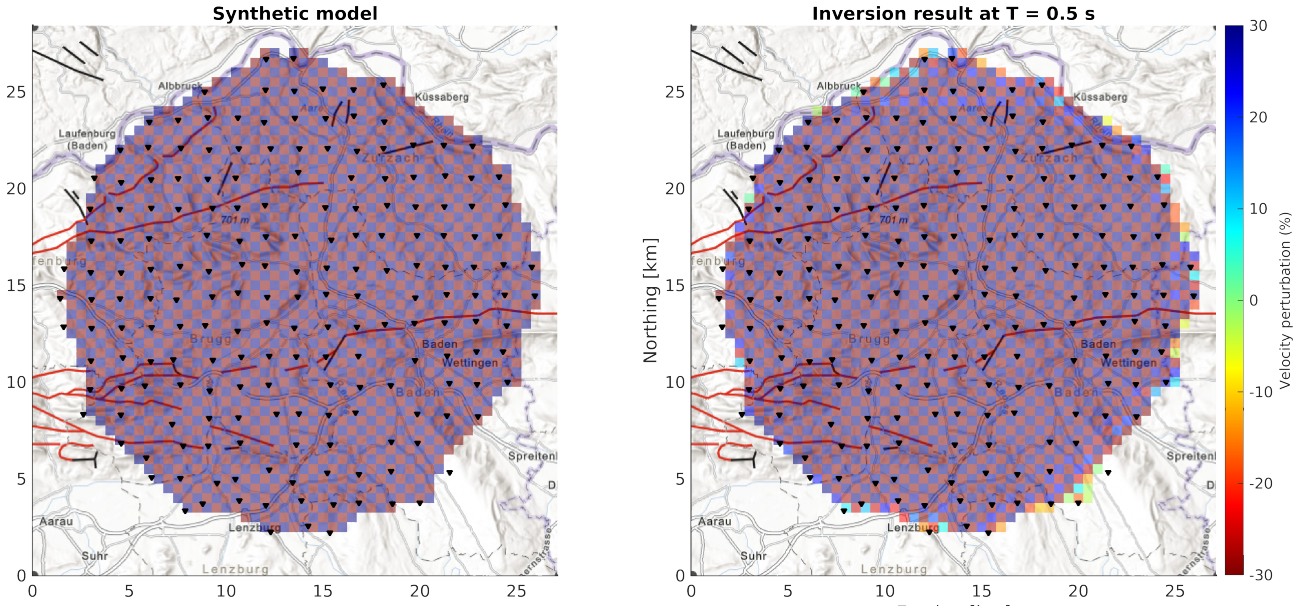
Checkerboard tests are a classic resolution test in passive seismic tomography. While they have some limitations [Rawlinson and Spakman, 2016], they are easy to interpret qualitatively. This test consists of first constructing a synthetic model, here presenting a ”checkerboard” pattern of positive and negative velocity anomaly blocks (e.g. +/- 30%), and then inverting the synthetic group travel time data to compare how close the recovered model resembles the checkerboard pattern. Distorted checkerboard shapes or underestimated anomaly amplitudes in the recovered model indicate poor resolution or smearing effects over the affected areas. In the context of group velocity maps, we have made the important assumption in our inversion approach of straight ray paths to represent surface wave propagation. In the far-field approximation (distance travelled much larger than the wavelength) and in a medium of moderate velocity contrasts, this assumption is considered acceptable. However, we must keep in mind that surface waves have a finite width of sensitivity along the ray paths and are not sensitive to anomalies smaller than approximately a third of their wavelength. The checkerboard tests should then only be regarded as a guide for station network design and to investigate the isolated effect of asymmetric ray path coverage and density on model resolution. Figures D.1 and D.2 show the checkerboard tests for the periods as presented in this report in Figures 4.1 and 5.1. For decreasing ray path density at higher periods, a larger checkerboard pattern can be recovered accurately, which gives an idea of the size of the anomalies that can be well resolved on the basis of ray path distribution alone.

D.2 Bootstrap resampling

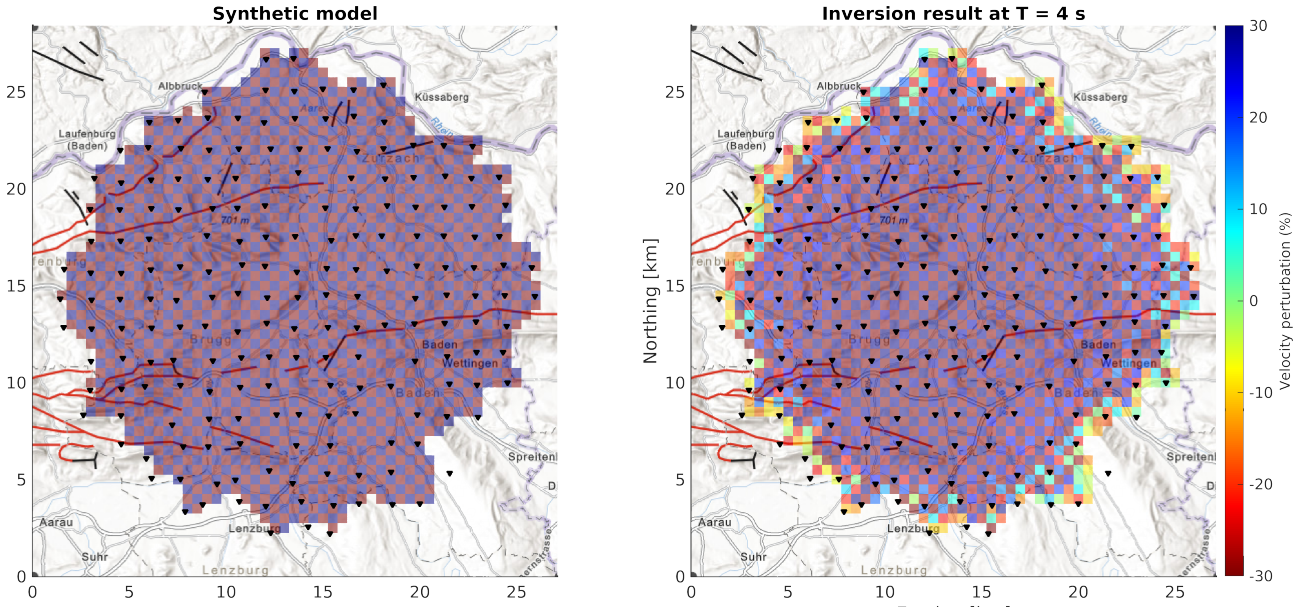
The bootstrap resampling [Schnaidt and Heinson, 2015] can be used to estimate the stability of the group velocity map inversion. We inverted for 500 models, with 5% of samples from the picking dataset removed randomly. The ensemble of models is then statistically analyzed to determine the variability of solutions. Figure D.3 shows two examples of the bootstrap test applied to data from Aargau and Riehen. We find that the standard deviation of the ensemble of models is usually higher at the boundary of more complex structures, for example near the Mandach Thrust in Aargau or on the Dinkelberg block in Riehen. The values of standard deviations are below 10 m/s, less than 1% of group velocity, which reflect very stable inversion results. This method however does not give the uncertainties on group velocity maps that are caused by data errors.

D.3 Comparison of different picking datasets

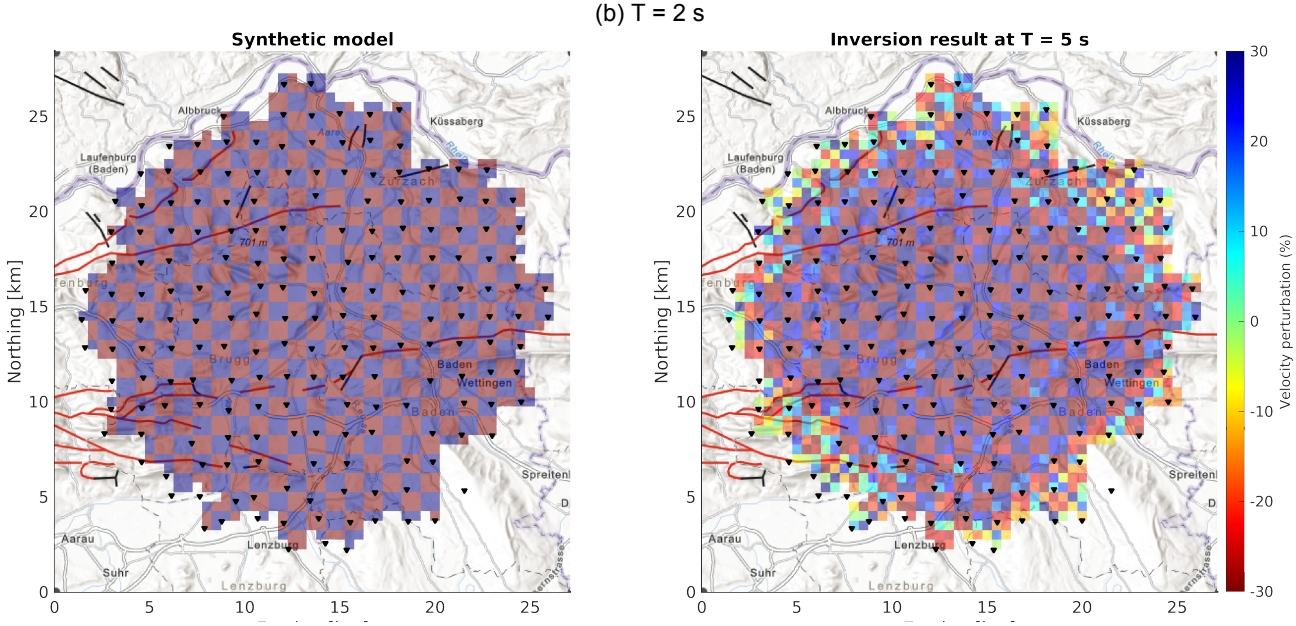
As detailed in the Methodologies chapter, we applied our picking approach to multiple cross-components. Since Rayleigh waves should be observed on the FTAN images of ZZ, ZR, RZ and RR cross-correlations (including stacking of their images), we can try to compare the group velocity maps recovered for different picking datasets. The features common to all these velocity maps could then be considered as robust features. This approach has however the limitation that the ray path density and coverage for these different picking datasets must be relatively similar so the comparison is not biased by ray path sampling. The noise level in the raw seismic records on the horizontal components is higher than on the vertical one, since the sensors are buried at a shallow depth directly in soil. Because the vertical component is less likely to be affected by undesirable noise effects, the ZZ cross-correlations always have more dispersion picks. Figure D.4 illustrate this approach with an example from both the Aargau and Riehen approach. We suggest such comparisons be used when interpreting group velocity maps. Quantitative uncertainties may also be derived from this approach, such as they can be used as input to the probabilistic depth inversion method.



(a) T = 0.5 s

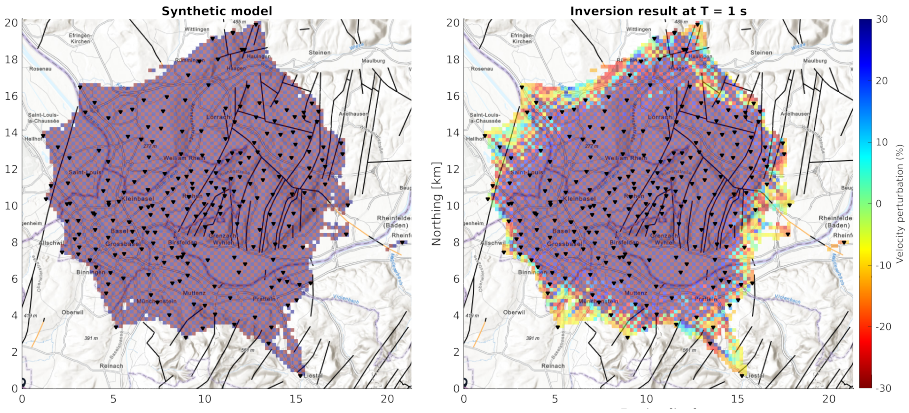


(b) T = 2 s

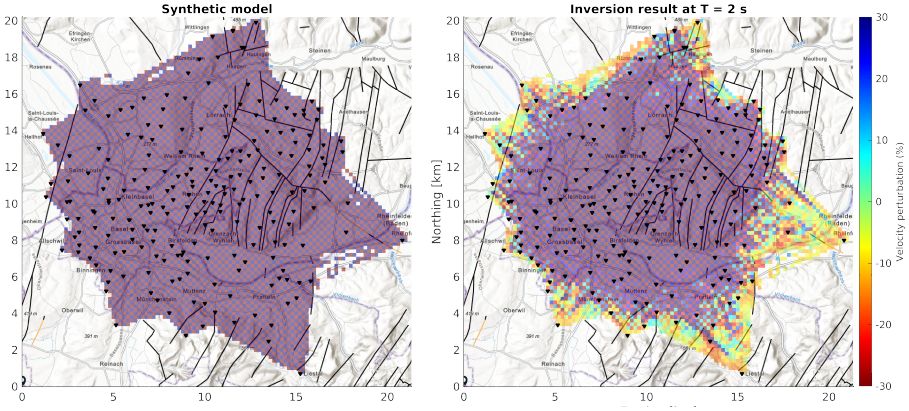


(c) T = 5 s

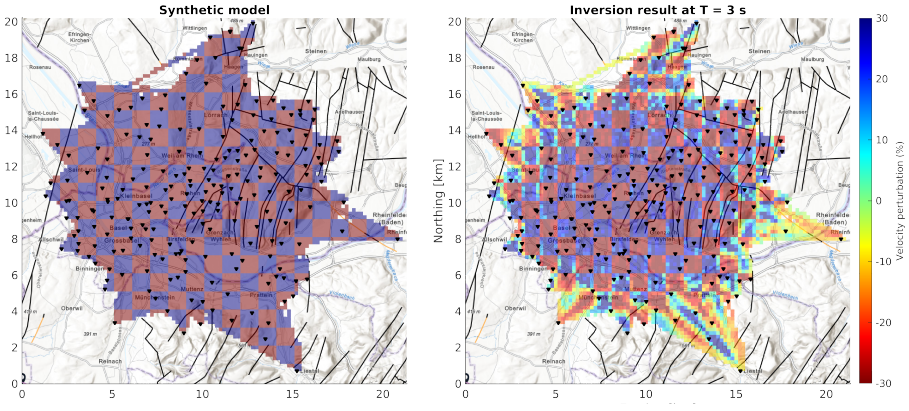
Figure D.1: Checkerboard tests for Aargau



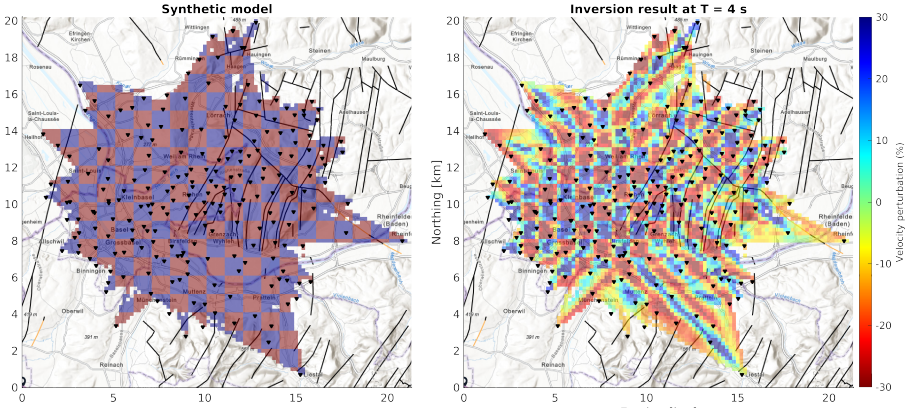
(a) T = 1 s



(b) T = 2 s

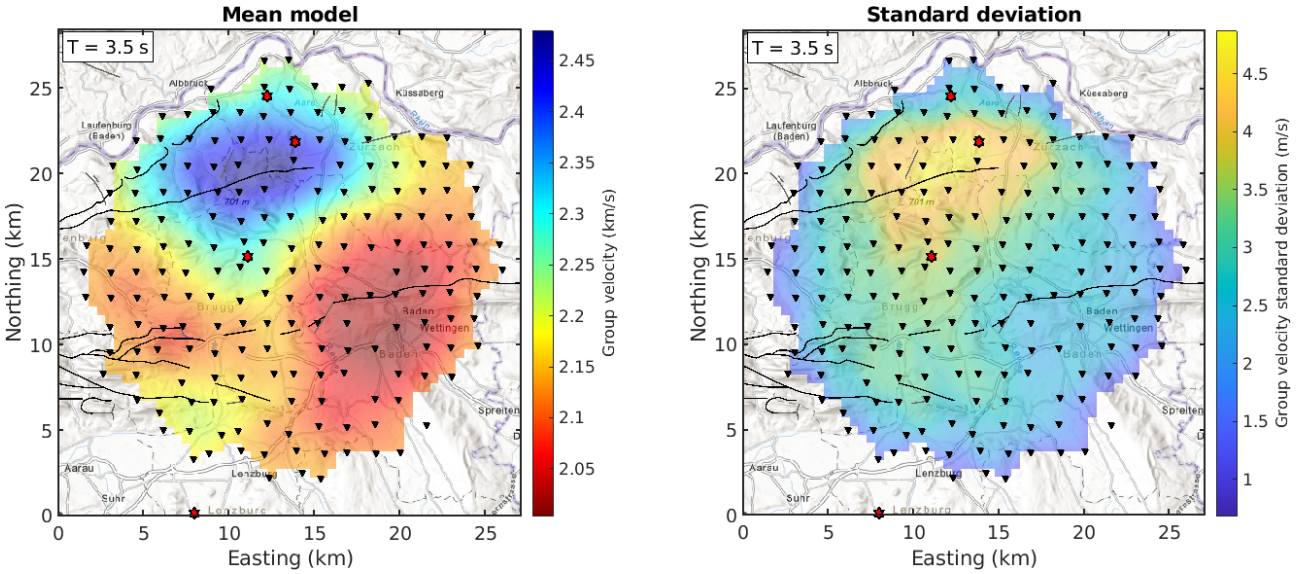


(c) T = 3 s

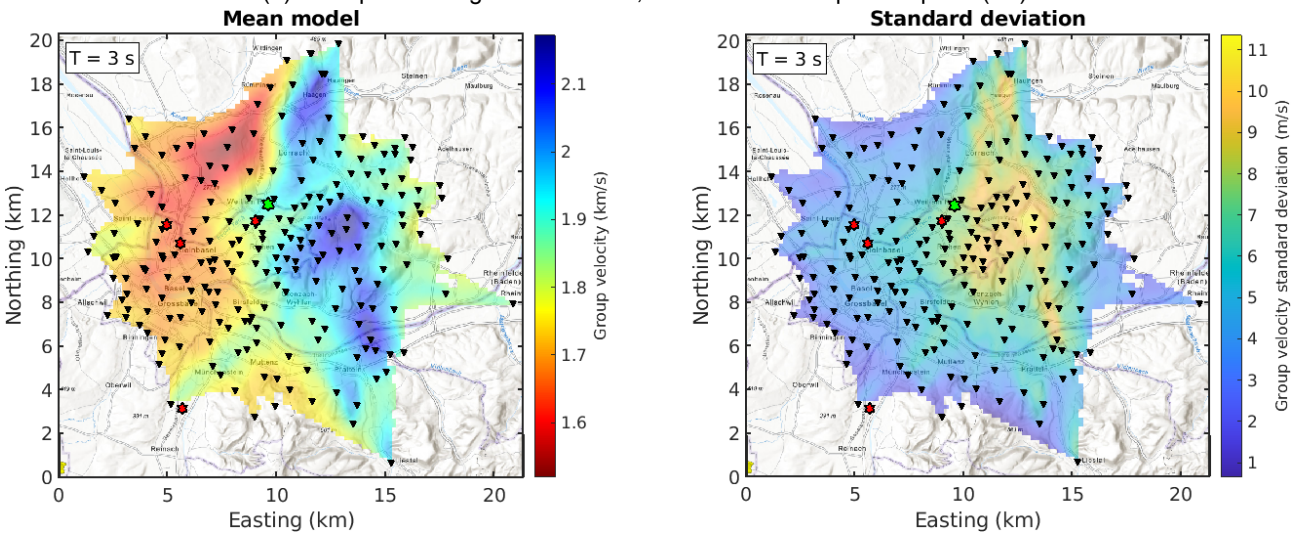


(d) T = 4 s

Figure D.2: Checkerboard tests for Riehen

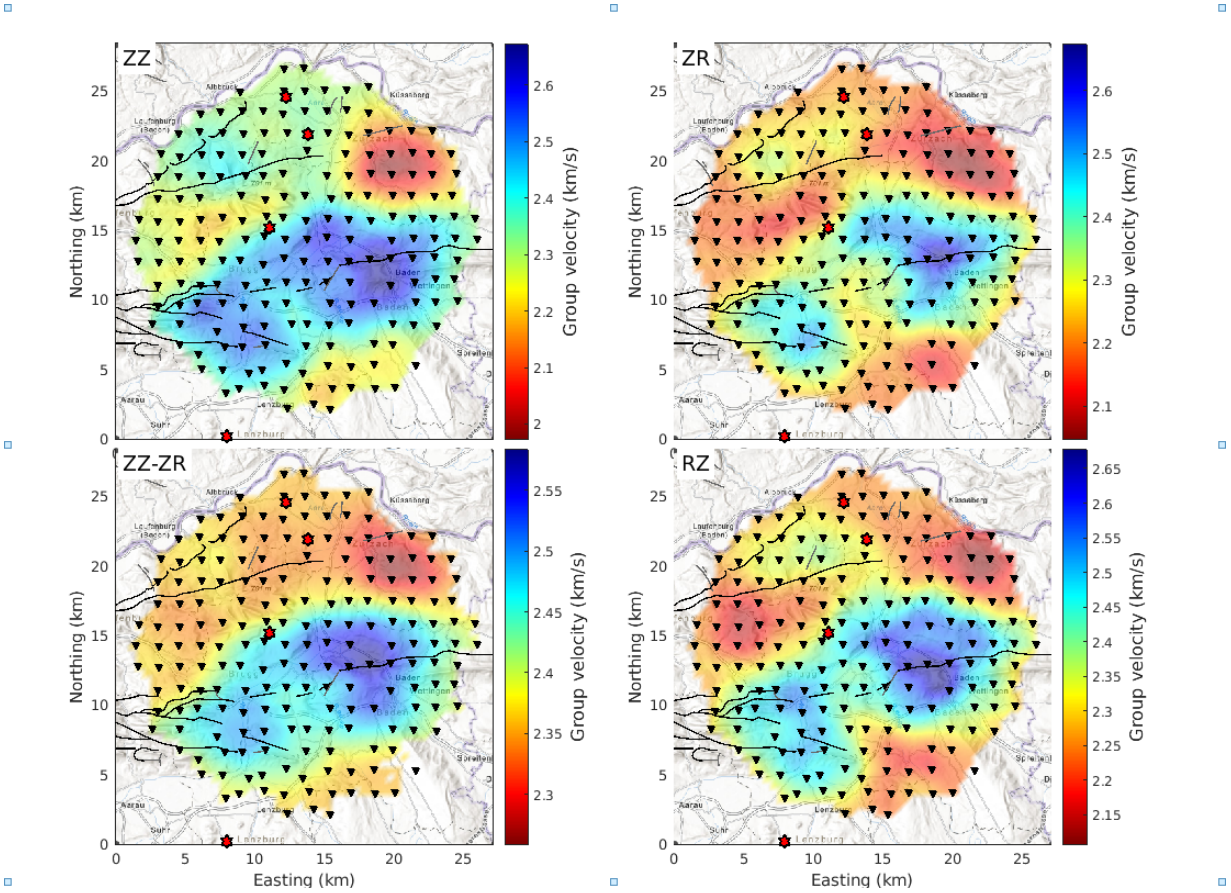


(a) Example for Aargau at T = 3.5 s, for Love wave dispersion picks (TT).

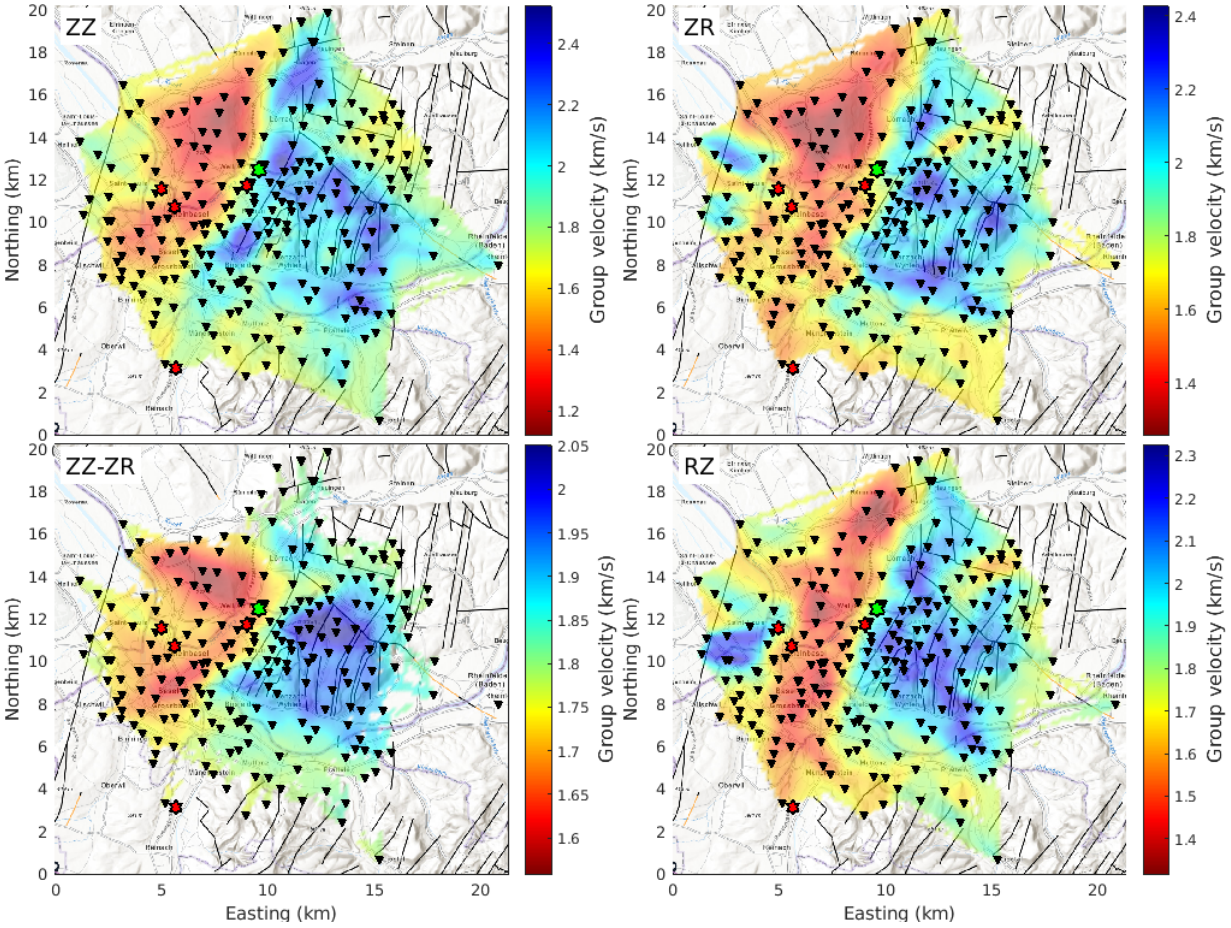


(b) Example for Riehen at T = 3 s, for Rayleigh wave dispersion picks (ZZ).

Figure D.3: Uncertainty estimation using bootstrap resampling. The maps on the left and right indicate respectively the mean and the standard deviation of the 500 realizations with 5% of data removed.



(a) Example for Aargau at T = 2.0 s.

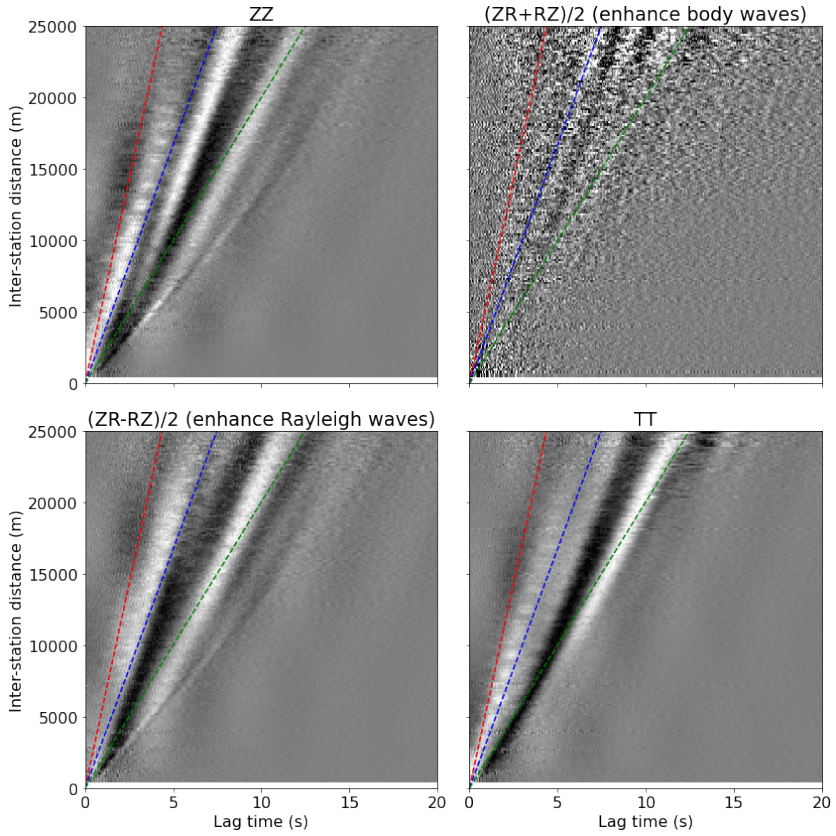


(b) Example for Riehen at T = 1.5 s.

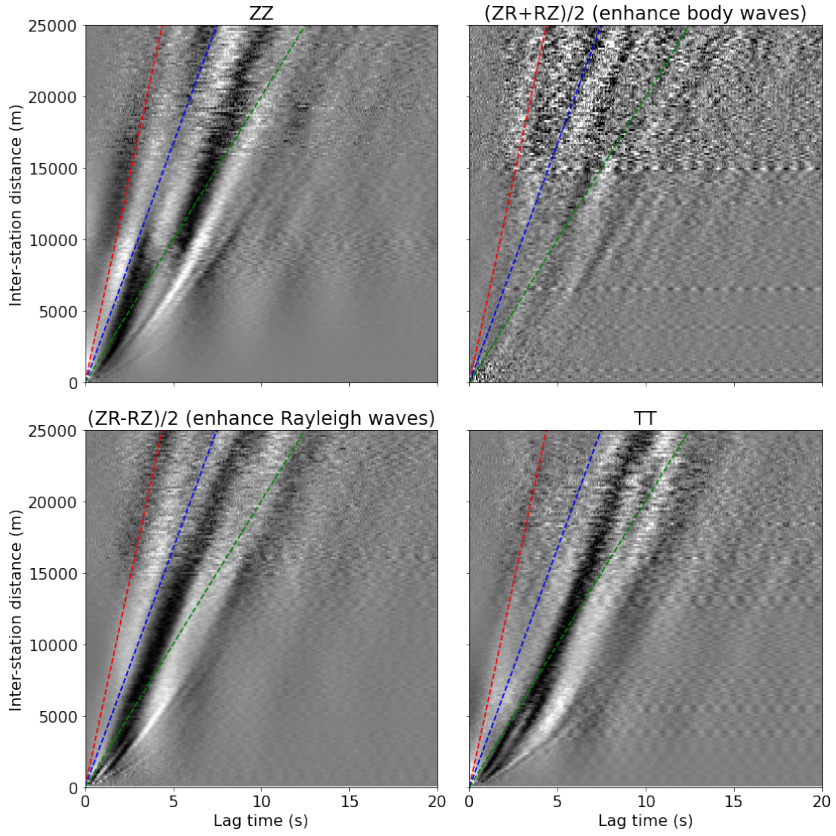
Figure D.4: Comparison of Rayleigh group velocity maps when using different picking datasets from Figures 3.10 and 3.11.

E. Polarization analysis to enhance body wave energy

It was suggested in several previous studies that the difference between the ZR and RZ cross-components could be used to enhance the smaller amplitude body wave energy from ambient noise cross-correlations (Takagi et al., 2014; Riahi et al., 2021). In an isotropic medium, the average ((ZR+RZ) /2) should enhance body waves, while the difference ((ZR-RZ)/2) should suppress body wave energy and retain surface wave energy only. In Riahi et al. (2023), they employed this approach and showed that the intensity of body wave energy varies throughout the recording period. For this reason, they had to carefully select the time windows used for the stacks to enhance sufficiently the weak signal from P waves. I applied a similar approach to both the Aargau and Riehen datasets. As in Riahi (2021,2023), the ZR+RZ cross-correlations when the entire recording period is stacked did not show any clear P-wave energy (Figure E.1). However, specific time windows showed fast apparent velocities on the ZR+RZ component, but these findings had some suspect characteristics that must be more carefully examined to ensure they are not artifacts from cross-correlations.



(a) Aargau dataset



(b) Riehen dataset

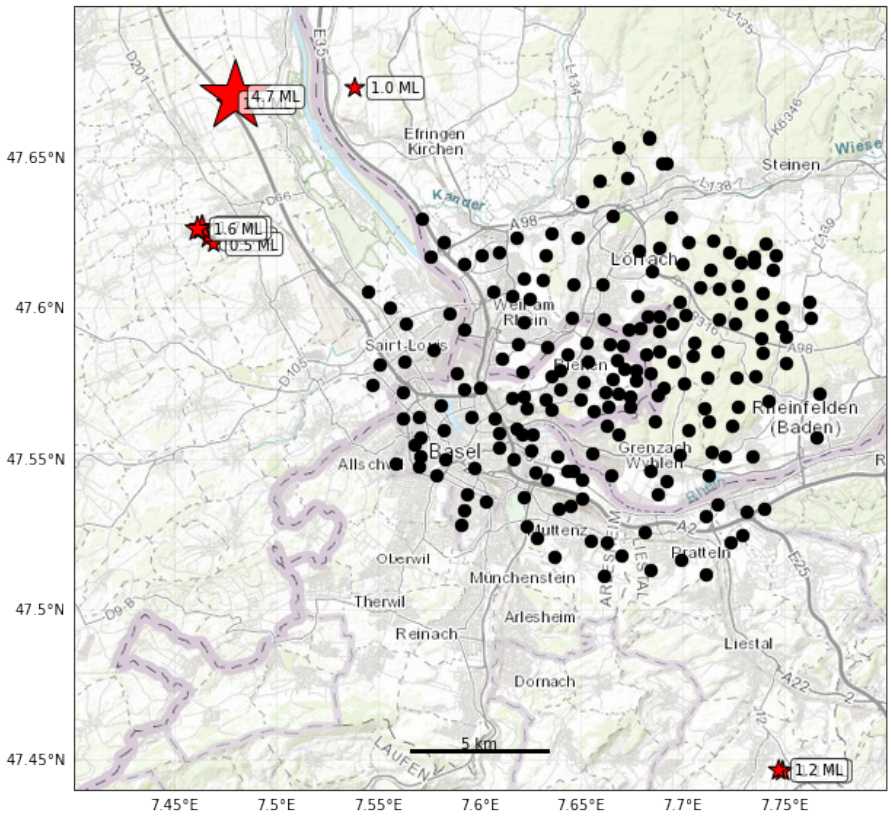
Figure E.1: Polarization analysis of ZR and RZ cross-components for the Aargau and Riehen dataset. The average of ZR and RZ enhances body wave energy, while the difference retains surface wave energy. The red and green lines indicate apparent velocities equal to the average Vp and Vs for these local areas based on regional earthquake tomography [Diehl et al., 2021], while the blue lines correspond to an apparent velocity of 2 km/s.

F. Local seismicity recorded by the Riehen nodal network

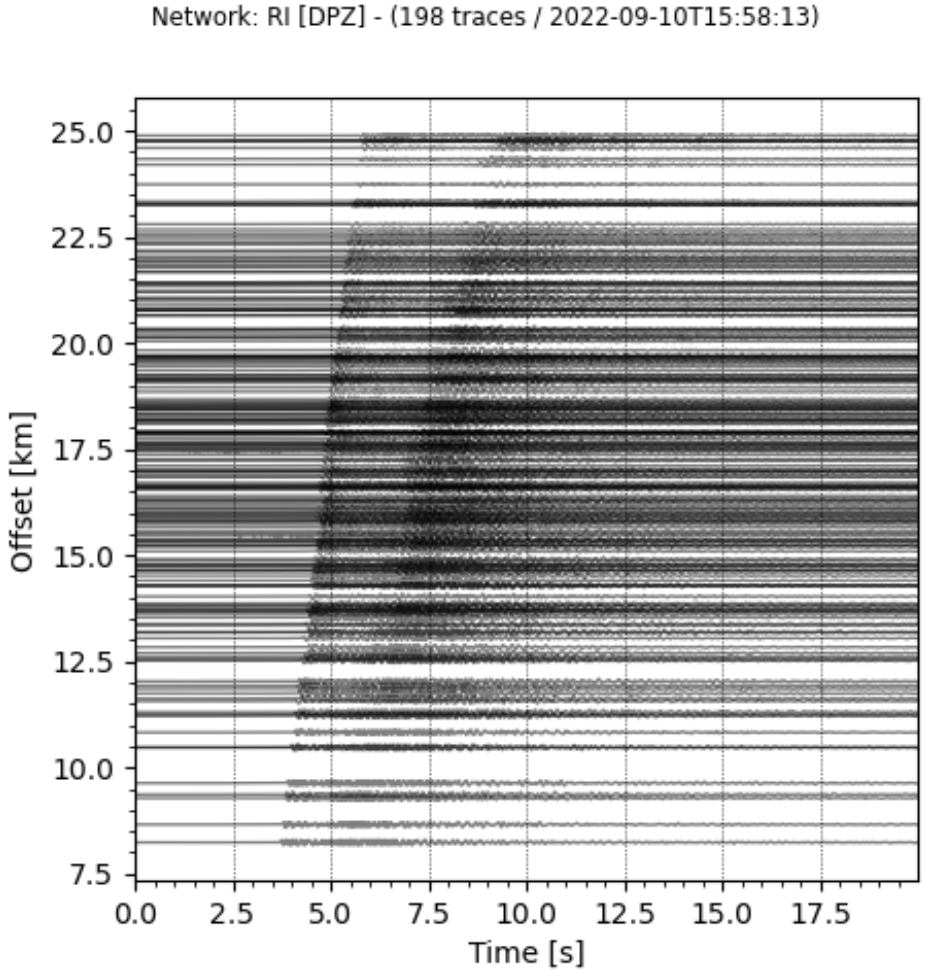
The earthquakes reported by both the EMSC and SED earthquake services during the Riehen deployment are listed in Table F.1 and mapped in Figure F.1. It included a powerful 4.7 ML event on the afternoon of September 10 at 13 km depth.

Origin Time (UTC)	Latitude	Longitude	Depth	Magnitude	Source
2022-09-05T08:21:48.854721Z	47.673	7.539	14.3 km	1.0 ML	SED
2022-09-06T17:24:55.701932Z	47.446	7.747	19.0 km	1.2 ML	SED
2022-09-06T17:49:54.476364Z	47.446	7.749	19.1 km	1.1 ML	SED
2022-09-10T15:58:13.000000Z	47.670	7.480	13.0 km	4.7 ML	EMSC
2022-09-10T16:24:22.922327Z	47.668	7.476	12.8 km	1.0 ML	SED
2022-09-10T20:48:50.567885Z	47.626	7.461	14.6 km	1.6 ML	SED
2022-09-10T20:49:28.334311Z	47.627	7.464	14.3 km	1.7 ML	SED
2022-09-10T20:55:21.579899Z	47.621	7.469	13.7 km	0.5 ML	SED
2022-09-10T22:59:27.233606Z	47.623	7.466	14.1 km	0.8 ML	SED

Table F.1: Earthquakes reported during the Riehen deployment



(a) Distribution of local earthquakes reported during the deployment. Black circles are nodal geophones and stars are earthquakes with size proportional to magnitude.

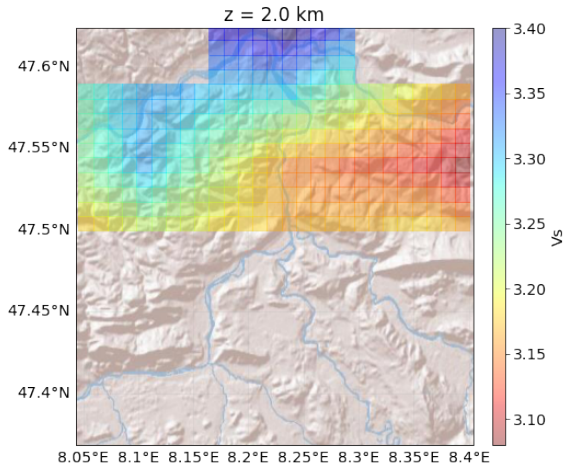


(b) The 4.7 ML event recorded on the nodal network.

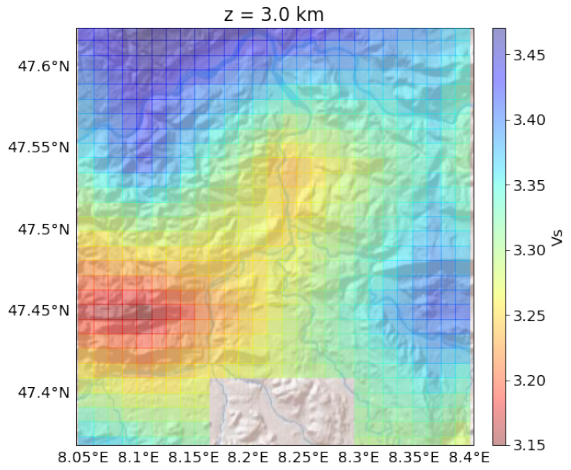
Figure F.1: Earthquakes reported during the Riehen deployment

G. Comparison to regional earthquake tomography

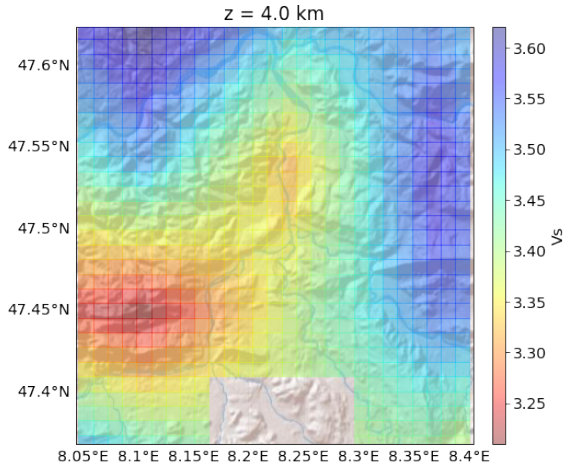
In Figures G.1 and G.2, we compare the NANT group velocity maps to the new Swiss 3D Vs model derived from regional earthquake tomography (RET) by Diehl et al. [2021]. This RET model is on a 3D grid with 1 km spacing, but the resolution of each cell depends on the distribution of earthquakes and SED permanent stations, which affects ray path density. We mask values of poor resolution (RDE < 0.075). We can see some consistency between the regional anomalies at 2-5 km depth and the larger wavelength features in the group velocity maps.



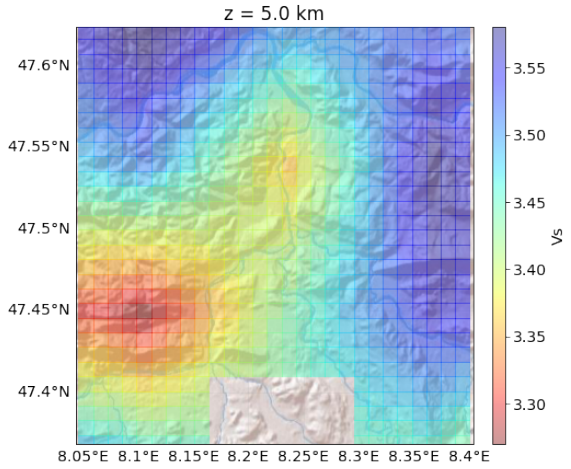
(a) Swiss 3D Vs z = 2 km



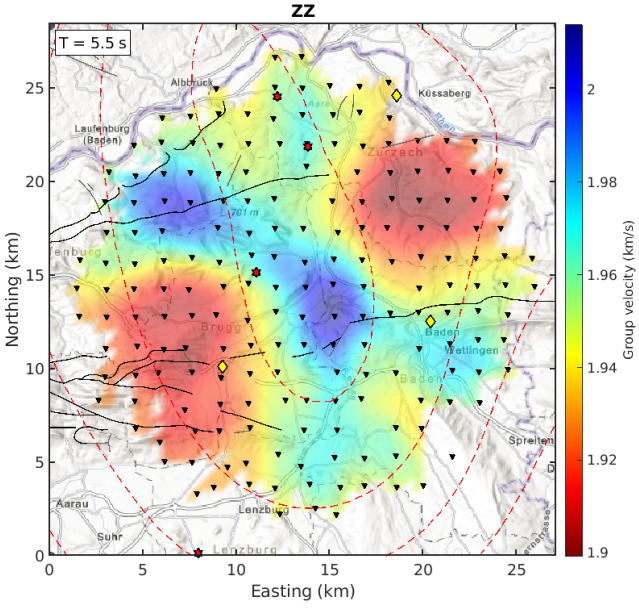
(b) Swiss 3D Vs z = 3 km



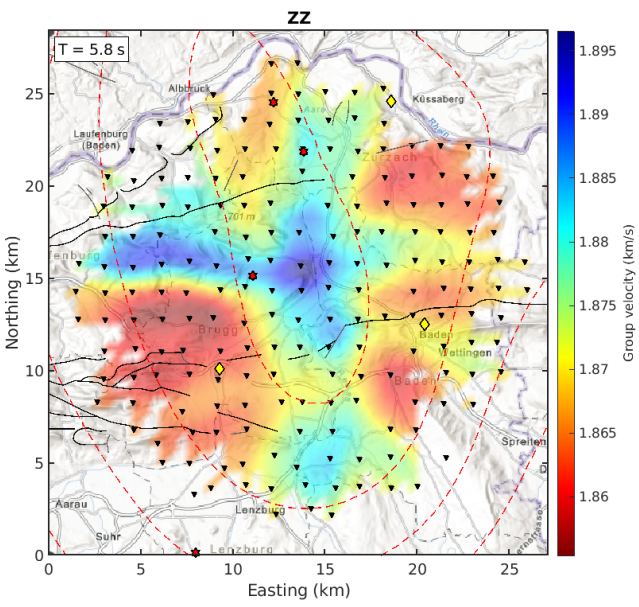
(c) Swiss 3D Vs z = 4 km



(d) Swiss 3D Vs z = 5 km

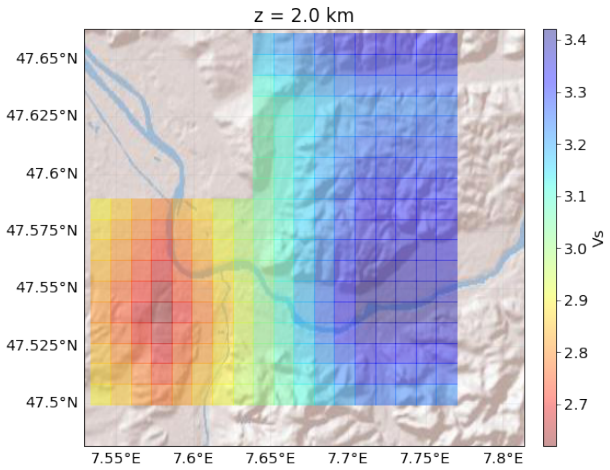


(e) NANT Rayleigh Vg T = 5.5 s

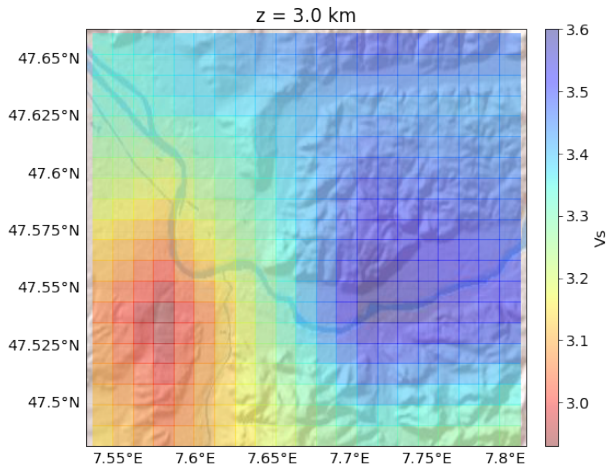


(f) NANT Rayleigh Vg T = 5.8 s

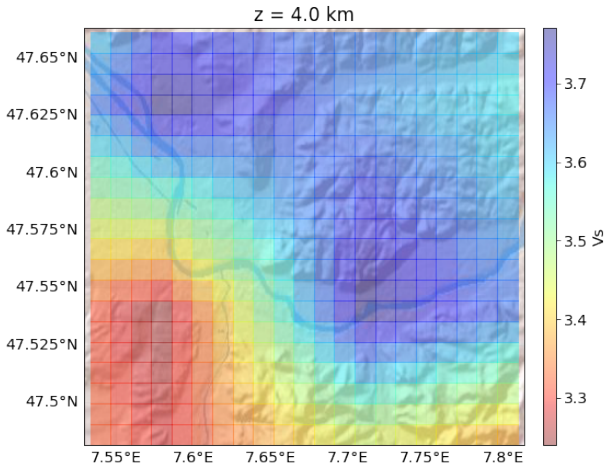
Figure G.1: Swiss 3D Sg velocity model from Diehl et al. [2021] in Aargau compared with two Rayleigh group velocity maps at 5.5 and 5.8 s. Grid nodes in the Swiss 3D Sg model with insufficient resolution are masked (RDE < 0.075, T. Diehl, pers. communication).



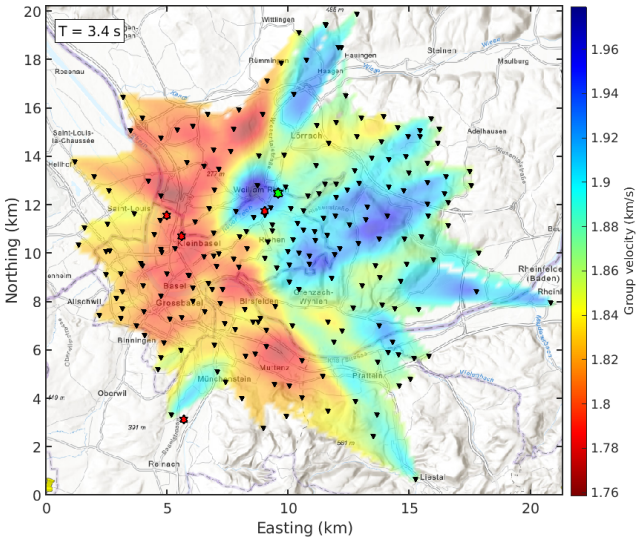
(a) Swiss 3D Vs z = 2 km



(b) Swiss 3D Vs z = 3 km



(c) Swiss 3D Vs z = 4 km



(d) NANT Rayleigh Vg T = 3.4 s

Figure G.2: Swiss 3D Sg velocity model from Diehl et al. [2021] in Riehen compared with Rayleigh group velocity map at 3.4 s. Grid nodes in the Swiss 3D Sg model with insufficient resolution are masked (RDE < 0.075, T. Diehl, pers. communication).

H. Possible methodological improvements

There are several aspects of the nodal NANT method that require further attention from a technical point of view or that could benefit from improvements. This includes:

- Combining Love wave dispersion with Rayleigh wave dispersion and ellipticity for the 3D depth inversion procedure to better constrain the shallower structure and fully consider uncertainties in measurements in the calculation of misfits inside the non-linear inversion algorithm. With a joint inversion, we can derive a V_{SV} and V_{SH} model and investigate radial anisotropy, which is an indicator of fracture density and hence, permeability.
- Shallow scale imaging in mountainous areas: for Aargau and Riehen, the topography could be safely neglected in the model inversion due to the relatively small path deviations caused by modest topographic features. However, in cantons such as Valais/Wallis, topography would likely present difficulties for NANT due to higher scattering and restrictions in terms of network design. Future projects could investigate incorporating topography into our existing inversion workflow and assess the reliability of the method in environments with higher scattering conditions.
- Increased horizontal resolution of NANT could be achieved with a higher number of nodes, on the scale of 500 and more. However, scaling up would require several adjustments to the group velocity map inversion step and a more efficient automated picking approach than we have developed for the results presented in this report. Better approaches could leverage machine learning developments in recent years to facilitate this very time-consuming, but critical step of NANT.